Improvement of Natural Fiber Mechanical Properties for Structural Polymer Composites

by

Amy Langhorst

A dissertation submitted in partial fulfillment
of the requirements for the degree of
Doctor of Philosophy
(Materials Science and Engineering)
in the University of Michigan
2023

Doctoral Committee:

Professor Alan Taub, Chair
Professor Mihaela Banu
Professor Nicholas Kotov
Professor Brian Love

Amy Langhorst

ammlang@umich.edu

ORCID iD: 0000-0001-9307-8410

DEDICATION

This dissertation is dedicated to my family, given and chosen. Without your love and support, this would never have been possible.

To my parents, your unwavering belief in the truth and power of science is what inspired me to pursue this Ph.D. I would never have made it here without your faith in me and your boundless support.

To Julia, you are my foundation and my home. Words can't describe how thankful I am for your support and patience throughout this journey - I couldn't have done this without you. Above it all, thank you for always believing in me. I am endlessly thankful that you have chosen to be by my side for all of life's adventures. Here's to writing the next chapter together.

ACKNOWLEDGEMENTS

I would like to first and foremost thank Professor Taub for giving me the opportunity to join his group. I started this PhD part-time while working full-time. I am very thankful that Professor Taub was willing to be flexible with my schedule and progress when I was juggling my career and PhD responsibilities.

I have learned and grown immensely by working with Professor Taub; he has helped shape the way I think through research and engineering problems, design experiments, and see the world. His enthusiasm for understanding and dedication to science has pushed me to strive for excellence and made me a better researcher and engineer. I am endlessly appreciative of all of the support, advice, and time he extended to me throughout my time at Michigan. Thank you for your dedication to being an outstanding advisor.

I would also like to extend a big thank you to Professor Miki Banu for her constant support and invaluable guidance, especially as we started navigating the natural fiber space as a team. She has always been a source of positivity and encouraged me every step of the way. I am very thankful for her guidance and mentorship throughout my time at Michigan.

Additionally, I would like to thank my other committee members, Professor Nicholas Kotov and Professor Brian Love. Thank you very much for your support, guidance, and suggestions in the completion of my dissertation work.

This work has been truly collaborative; I am very thankful to everyone who has contributed advice, methodology, and/ or data collection to this work:

A big thank you to Julie Rieland who helped measure the crystallinity and structure of fibers via XRD in this work. Thank you for many hours of analysis time and always being willing to think through possible theories for the mechanisms at play.

I would also like to thank the Sodano group. Thank you to Steven Mamolo, who helped to generate the Interfacial Shear Strength measurements presented in this work, Ruowen Tu, who helped troubleshoot composite fabrication with me, Dr. Kelsey Steinke, who provided invaluable advice on composite fabrication and analysis, and Professor Henry Sodano for his support and guidance.

I am also very thankful for the contributions of Mengjie Yu and Professor Richard Laine. A big thank you to Mengjie, for helping measure the porosity and surface area of fibers analyzed in this work, and to Professor Laine for your support and guidance.

A huge thank you to Xhulja Biraku, who helped mount and microtome many of the fibers used for morphological analysis. Thank you for always being willing to help tackle new challenges. You will be writing your thesis before you know it!

A big thank you to the Ellis group: Ellen Thompson, Eva Albalghiti, and Professor Brian Ellis. We lost a critical piece of equipment in the last few months of this work and could not have completed this without your support. To Ellen Thompson - thank you so much for taking the time to help me troubleshoot, teaching me how to use new instrumentation, helping ensure that we were doing everything safely, and being such a positive person!

Thank you to Andy Poli and Professor Ellen Arruda for their guidance and advice in novel mechanical testing and imaging techniques.

To the Taub Group, past and present: Dr. Wes Chapkin, Dr. Aaron Gladstein, Dr. Randy Cheng, Dr. Anshul Singhal, Kanat Anurakparadorn, Jon Goettsch, Anita Li, Jonah Berman,

Jonah Chad, Seth Fox: thank you all for your advice and help throughout the years. To Jonah Berman, Jonah Chad, and Seth Fox, thank you so much for all your contributions to this work via single fiber preparation, composite fabrication, fixture design, and testing. To Anshul Singhal, thanks for always being willing to think through problems with me and for your guidance and support.

To the Van Vlack Lab Staff: Dr. Sahar Farjami, Dr. Tim Chambers, Justin Scanlon, and Keith McIntyre, thank you for all your advice, troubleshooting, and support! To Keith McIntyre – thank you so much for the advice, guidance, equipment training, and support. I may not use a mill often in the future, but I will always have a strong appreciation for the art of precision machining. Who knew how hard it was to cut a precise 15-degree bevel into Garolite sheet? Thank you for troubleshooting with me for weeks on end and teaching me about sine plates & gauge blocks.

A big thank you to the staff at $(MC)^2$ for their advice and contributions to this work. Thank you to Allen Hunter for his PFIB advice and preparation of specimens for TEM. A big thank you to Tao Ma for his contributions via TEM imaging and EDS – searching for 5nm TiO_2 was not easy! Thank you to Nancy Muyanja for guidance and advice as well as evaluation of fibers via XPS. And many thanks to Bobby Kerns for his advice, guidance, and support in all things from finding the appropriate technique, determining how to prepare samples appropriately, and helping with data analysis.

Thank you to all the MSE department staff including Ellen Kampf, Renee Hilgendorf, Kevin Worth, Shelley Fellers, Lourdes Jorgensen, and Todd Richardson for your support throughout the years!

A big thank you to Anton Paar, and Andy Labrousse, for their support in measuring the density of the fibers in this work via gas pycnometry.

Thank you to Ford Motor Company for the financial support of this research. Also, thank you to the many dedicated members of Research and Advanced Engineering at Ford Motor Company who supported this PhD journey, including Dr. Elisa Harrison, Dr. Sabrina Peczonczyk, Janice Tardiff, Dr. Mark Nichols, Dr. Cindy Barrera-Martinez, Megan Shewey, Dr. Alper Kiziltas, and Dr. Deborah Mielewski. A big thank you to Dr. Elisa Harrison for the TOF-SIMS imaging presented in this work. To Elisa & Sabrina – thank you for all your support, positivity, and inspiration – I wouldn't be here without you! To Janice, Mark, Cindy, and Megan, thank you so much for all your support and guidance throughout the years.

A huge thank you to my family and friends for all of your support throughout the years. A big thank you to Beth and Ben Langhorst for your fabulous coloring skills. To my closest friends, thank you for keeping me sane, accepting me even when I fell asleep at 9pm, for cheering me up on days when experiments didn't work as expected, and being my chosen family. To my family, thank you for always believing in me, accepting me for who I am, and supporting me in this journey.

TABLE OF CONTENTS

LIST OF TABLES

LIST OF FIGURES

ABSTRACT

Transportation of people and goods accounts for 25% of global energy consumption, with personal transportation accounting for more energy consumption than all forms of freight combined. As global CO_2 levels have increased in recent years, the transportation sector has increased its focus on the development of low carbon footprint products. Automakers have focused on the replacement of monolithic materials with composites, which can be stronger and lighter than the materials they are replacing. However, many structural polymer composites contain fiberglass reinforcement, which has high density and is energy intensive to produce. Prior work has found that replacement of glass fiber with natural fibers as reinforcing agents in polymer composites can reduce component weight by 25-30% and CO_2 emissions by >8 kg/ vehicle. However, the widespread use of natural fibers as a replacement for glass in structural polymer composites has been limited by the lower intrinsic mechanical properties of natural fibers in comparison to glass. Research efforts to improve natural fiber composite properties have been mainly focused on improving fiber-matrix adhesion via chemical and physical treatments, with some treatments known to compromise the mechanical performance of the fiber itself.

This work focused on the development of a treatment for natural fibers capable of improving natural fiber stiffness to enable the widespread use of natural fibers in structural composites. Treatment of flax fibers in supercritical fluids in the presence of nanomaterials was explored to attempt to improve flax fiber mechanical properties. Treatment of flax fiber in

supercritical CO_2 ($scCO_2$) in the presence of titanium dioxide (TiO_2) nanoparticles resulted in a 71% and 80% increase in fiber tensile modulus and ultimate tensile strength, respectively. No evidence of incorporation of TiO_2 nanoparticles within flax fibers was observed. Treatment resulted in changes to fiber morphology and structure. Prior work has shown that smaller cross-sectional area fibers exhibit higher strength and modulus. Treatment in $scCO_2$ with TiO_2 resulted a reduction in fiber cross-sectional area, suggesting that treatment resulted in fiber fibrillation. Additionally, after treatment, a 70% reduction in fiber porosity was observed, including collapse of the lumen (an internal closed pore within each cell in a fiber) and closure of micro/meso pores. The crystallinity of the fibers was increased by 11%, as determined via x-ray diffraction. In addition, treatment resulted in surface smoothing, as a 98% reduction in fiber surface area was observed. Two mechanisms for changes to the fibers were proposed: 1) fiber fibrillation: in which low-crystallinity, high porosity components of each fiber were removed via repeated impact with nanoparticles during treatment, resulting in a fiber with higher crystallinity, low porosity, and smaller cross-sectional area, and 2) shot peening: in which repeated impact of the fiber surface with nanomaterials under high pressure resulted in local plastic deformation of the fiber causing cellulose crystallization, surface smoothing, and pore closure.

Formation of 30 vol% epoxy composites containing flax fibers treated in $scCO_2$ with TiO_2 nanoparticles resulted in composites with 43% and 37% higher modulus and strength than composites containing untreated fiber. New models for the prediction of composite modulus were created, considering fiber size as a non-negligible factor contributing to fiber modulus. Overall, this dissertation laid the groundwork for development of a cost-effective, optimized method for improving the mechanical properties of flax fibers and their resulting polymer composites.

Chapter 1
Introduction

1.1 Motivation

The demand for carbon-negative materials and technologies has increased in recent years, as manufacturing companies seek to reduce their global carbon footprint. Transportation accounts for approximately 25% of global energy consumption, with light-duty vehicles consuming more energy than all modes of freight transportation combined. [1] Because of this, over the last 50 years, automakers have devoted significant resources towards improving the fuel economy, vehicle range, and sustainability of their products. In addition, since 2015, battery electric vehicle (BEV) sales have increased by over 500%, as automakers transition from the production of internal combustion engine (ICE) powered vehicles to alternative powertrains. [2,3] Because of the lower energy density provided by batteries in comparison to liquid fuels, reducing vehicle weight has a more significant effect on BEV range compared to fuel economy improvements in ICE powered vehicles. Specifically, a 10% reduction in BEV weight can improve electric range by 14%, making the value proposition for increasing the use of lightweight materials very appealing.[4,5] In order to meet consumer demand for vehicles with long vehicle range and low carbon-footprint, automakers need new lightweight, sustainable materials capable of replacing heavy vehicle components.

Composite materials have the potential to be stronger and lighter than monolithic materials they may be replacing. The US Department of Energy estimates that replacement of cast iron and traditional steel components with lightweight materials, including polymer

composites, could reduce vehicle weight by up to 50%. [6] Over the last several decades, many traditionally metallic automotive components have been replaced with fiberglass-reinforced polymer composites. However, fiberglass is relatively heavy, with a density of ~2.6 g/cm^3, and requires significant energy to produce. In recent years, automakers have also invested in the development of more sustainable polymeric composites, including composites containing bio-based resins, fillers, and reinforcements, including natural fiber composites. Natural fibers have the advantages of being renewable, lightweight, and low cost. In the last 20 years, Ford has produced vehicle components containing wheat straw and cellulose, BMW has used bamboo in interior composites, and flax fiber has been used to reinforce components on Porsche and Polestar vehicles. [7]

Replacement of glass fiber with natural fibers could significantly contribute to automaker goals of reducing vehicle weight and vehicle carbon footprint. Specifically, the replacement of glass fiber with flax fiber has been shown to reduce the carbon footprint of the resulting polymer composites by 3 tons of CO_2/ ton of polymer composite produced and can reduce vehicle component weight by up to 25-30%. [8,9] However, many applications of natural fiber composites on vehicles are in non-structural components, with glass fiber used as primary reinforcement in most structural automotive composites. While the best reported values of the density normalized (specific) properties of natural fibers are competitive with glass fiber, the main barrier to widespread use of natural fibers as reinforcement in structural polymer composites is the high variability and low average mechanical properties of natural fibers themselves. (Table 1.1) Prior work has shown that the species, cultivation conditions, and extraction techniques can significantly affect the final performance of the extracted fibers. [10,11] From a design perspective, this variability makes it challenging to model the

performance of desired structures and requires engineers to design to the lower bounds of fiber performance to prevent premature failures. Because of the potential for natural fiber composites to be used in the production of lightweight, carbon-negative vehicle components, there is strong motivation to find ways to reduce fiber variability and improve the intrinsic properties of the fibers via improved cultivation/ extraction techniques or novel fiber treatments. This work seeks to develop a novel technique to improve the performance of flax fibers, resulting in fibers more suitable for the replacement of glass fiber in structural polymer composites.

Table 1.1 Properties of natural fibers in comparison to glass fiber, as reported in the literature. [8,12,13]

Properties	**E-glass**	**Flax**	**Hemp**	**Cotton**	**Bamboo**
Density (ρ) (g/cm^3)	2.55	1.3-1.5	1.48	1.5	1
Tensile strength (MPa)	2400	800-1500	550–1110	287-800	391-860
Specific strength (MPa/ρ)	940	138-965	100-750	191-533	100-860
Elongation (%)	3	1.2-1.6	2-3	3-10	1.7-1.9
Modulus (GPa)	73	20-80	30-60	5.5- 13	18-46
Specific Modulus (GPa/ρ)	29	18-53	39-47	3.7-8.4	18-46

1.2 Natural Fibers

Flax fibers used in composites and textile applications are phloem fibers, or bast fibers, which develop in flax stems with the purpose of providing structural support for the plant (Figure 1.1). To extract flax fibers, stems are first retted, which is a process in which microbes or chemicals are used to soften and loosen the bast fibers from the stem. Dew retting is the most common form of retting used today, in which flax stems are cut and left in the field to be

exposed to naturally occurring microbes. [14] After retting, flax fibers undergo mechanical extraction from the stem via scutching and hackling. During scutching, stems are scraped by a series of co-rotating knives to form ribbon like fiber bundles. Hackling involves combing these bundles, resulting in refining of the bundles into smaller technical fibers. [15]

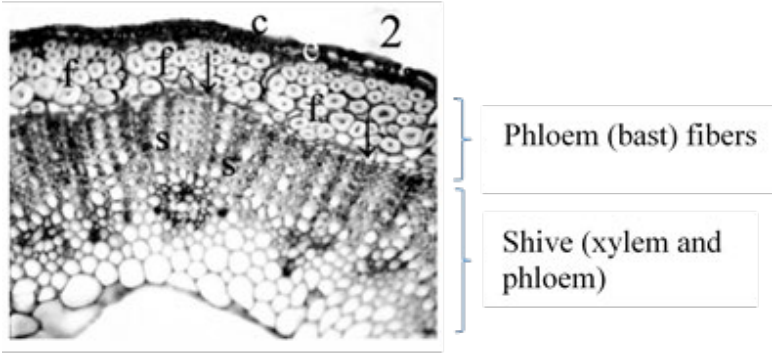

Figure 1.1: Light micrograph of flax stem, indicating location of phloem (bast) fibers and flax vascular structure (xylem & phloem cells). [14,16]

Flax fibers used for reinforcement in composites are commonly referred to as technical fibers. The technical fiber consists of individual plant cells (elementary fibers), bound together with a pectin-rich interface called the middle lamella. Each elementary fiber is approximately 5-35 μm in diameter and 2-5 cm long, with an internal pore called the lumen, which can be up to 40 μm long (Figure 1.2). [16–19] The cell wall of an elementary fiber is commonly divided into three layers which provide the structure for the plant. [18] The secondary cell wall makes up about 80% of the elementary fiber cross-section and contains highly crystalline (~65-70% crystallinity) cellulose microfibrils angled at ~10° to the cell axis in a matrix of amorphous hemicellulose and pectins (Figure 1.3). [11,18,20–22]

While the lumen inherently presents large internal porosity within a technical fiber, prior work has reported the presence of additional small internal cavities within flax fibers, resulting in

stress concentrations during loading and leading to fiber failure. [17] Reductions in flax fiber porosity, achieved via chemical or thermal treatments, have shown to improve mechanical interlocking and chemical bonding within a fiber, resulting in improved mechanical properties. [23–25]

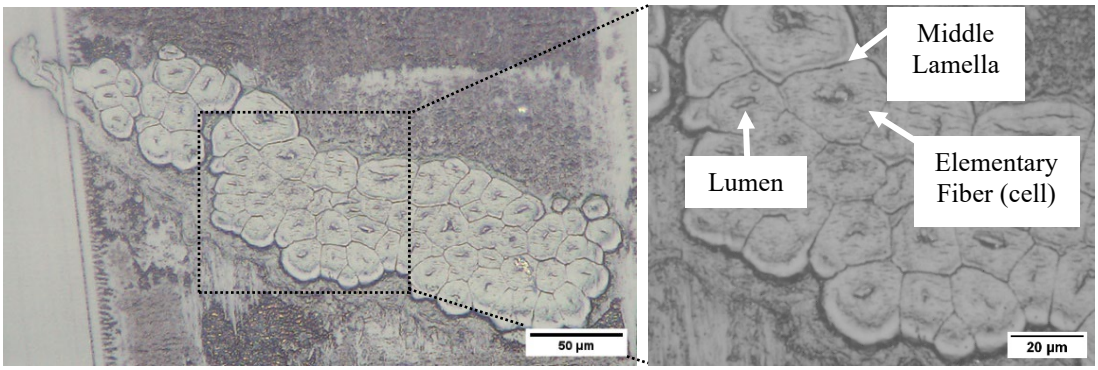

Figure 1.2 Optical micrographs of a flax technical fiber. Each elementary fiber (plant cell) contains a lumen. The cell walls consist of a network of crystalline cellulose microfibrils held in a matrix of hemicelluloses, lignin, and pectin. Elementary fibers are bound together via a pectin-rich middle lamella.[7]

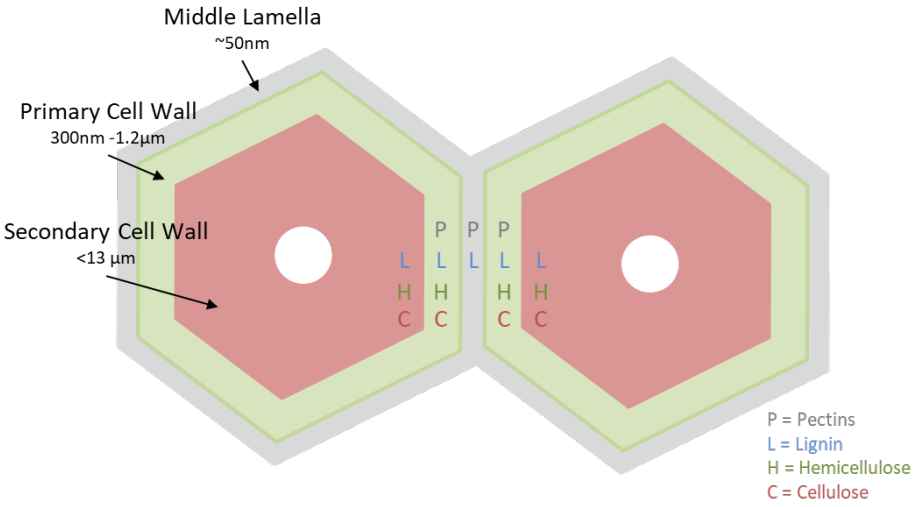

Figure 1.3: Schematic of the structure and chemical composition of flax fibers.

Prior work has studied the failure mechanism of technical flax fibers under tension. Work by Romhany, et al, was able to determine a failure mechanism of flax fibers via simultaneous tensile testing, SEM, and acoustic emission (AE). Their findings verify that the main location for crack initiation occurs at the elementary fiber interfaces within a flax technical fiber (Figure 1.4). [26] Additionally, Charlet, et al, were able to measure the mechanical properties of the interface between elementary flax fibers. Their work showed that the interfacial shear strength and shear modulus of this interface was 2.9 MPa (± 2.4 MPa) and 18.7 kPa (± 10 kPa), respectively. They reported that the shear modulus is stiffer than pure pectin, likely due to minor lignification present throughout the compound middle lamella. [27] However, the shear strength of this interface is very weak, exhibiting shear strength with nearly half of the interfacial strength of PLA and natural fiber, the weakest known synthetic polymer/ natural fiber interface. [27] Therefore, initiation of technical fiber failure through the elementary fiber interface may be due either to inherent weakness of the middle lamella, or due to degradation of the middle lamella during retting. Improvement in interfacial adhesion between elementary fibers or reparation of damage caused during fiber extraction could delay crack initiation/ propagation and improve fiber strength.

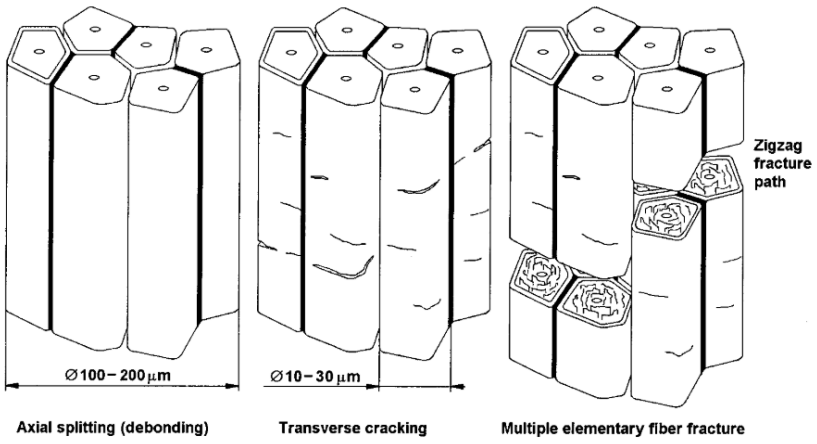

Figure 1.4: Schematic and microscopic visualization of technical fiber failure mode. Fiber failure initiation occurs at the elementary cell wall interface, via failure through the middle lamella.[24,26]

It has been shown that increased processing of natural fibers results in technical fibers with improved properties. [20,24,28] For example, flax fibers tested after scutching showed lower tensile properties than fibers tested after scutching and hackling. [15] Additionally, bulk fibers from wood (technical fibers) have a Young's modulus near 10 GPa, but after pulping, a single pulp fiber can have a modulus near 40 GPa. [20,24] With increased processing, the fineness (mass/fiber length) decreases, resulting in a reduction in length and diameter of each technical fiber. [29] It is suggested that finer fibers consist of fewer elementary fibers across their diameter, limiting the number of weak middle lamellae and improving the overall strength of a fiber. [20,24] Bevitori, et al, and Bourmaud, et al, reported an inverse dependence between tensile strength and fiber diameter as well as tensile modulus and fiber diameter (Figure 1.5). [28]

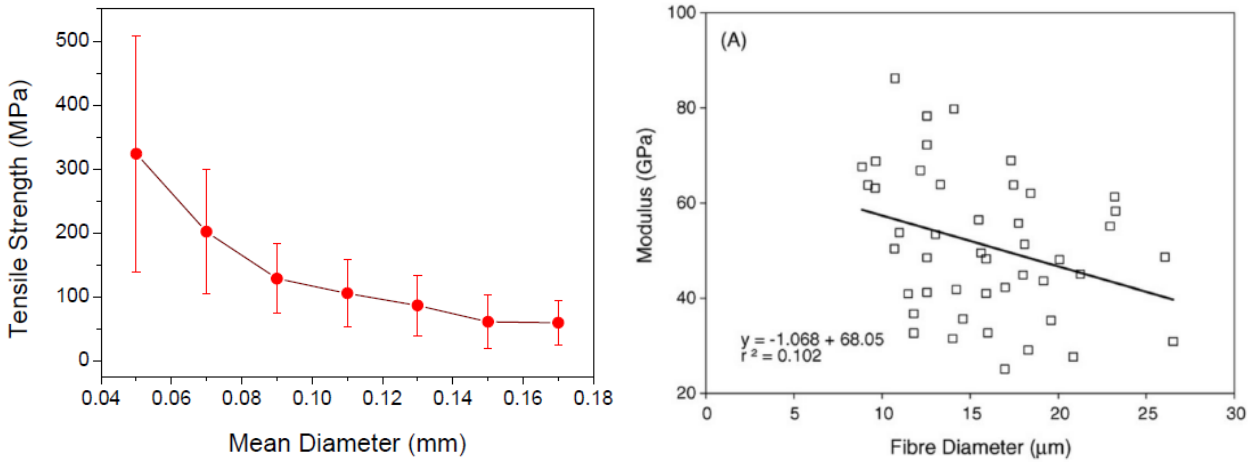

Figure 1.5: Relationship between jute fiber diameter vs. tensile strength and flax fiber diameter vs. modulus. Smaller diameter fibers exhibit improved tensile properties. [20,24,28]

1.3 Fiber Modifications

Chemical treatments have been explored as a means to improve natural fiber properties and their resulting composites, including alkali treatments, acetylation, and silane treatments. [30–33] Treatment of fibers with sodium hydroxide (NaOH) solution was shown to remove amorphous lignin, pectin, and hemicellulose from fibers while exposing hydroxyl groups on the fiber surface. The treated fiber exhibited high surface area, enabling strong mechanical entanglement and chemical bonding between the fibers and non-polar polymer matrices like polypropylene. [34,35] Use of low-concentration alkali solution for treatment of flax fiber enabled production of flax-epoxy composites with a 30% increase in tensile strength and modulus after treatment. [30] Silane treatment and acetylation have also been shown to be effective at improving the fiber-matrix interface. [31,35] Silane treatment enables siloxane bridging between hydroxyl groups present on natural fibers to non-polar matrices. [35] However, chemical treatments have also been shown to reduce fiber properties and compromise the associated composite properties. Treatment with sodium hydroxide has been shown to cause the

conversion of cellulose-I to cellulose-II, a more thermodynamically stable structure than cellulose-I, but with a modulus that is 35% lower due to reduced crystallinity. [31,36–38] In prior work, the modulus of flax fiber was reduced from 46.9 GPa to 13.5 GPa after extended treatment in NaOH solution. [32] In addition, the modulus of sisal fibers treated with silane was shown to be reduced by over 10%. [31] A 30% flax fiber-polypropylene composite containing flax treated with 20% NaOH resulted in a reduction in modulus from 1660 MPa to 1500 MPa. [32]

Supercritical fluid has also been explored as a treatment for natural fiber surface modification, extraction of lignocellulosic components, and improved dyeing. [39–43] Supercritical CO_2 ($scCO_2$) is a non-toxic, non-polluting, and non-flammable substance with a moderate critical point (31.1°C, 7.4 MPa). [43] The densities of supercritical fluids are similar to many liquid, organic solvents but their diffusivities and viscosities are near those of gases. Because of this, $scCO_2$ has been shown to be very effective at swelling and plasticizing amorphous polymers by intercalating between polymer chains and interfering with molecular interactions, resulting in reductions to glass transition temperature and reduce polymer processing temperatures. [44] Prior work has evaluated the use of supercritical CO_2 as a means for solvent-less dyeing of natural fibers, and several authors have attempted to use supercritical CO_2 for the extraction or removal of non-cellulosic components from natural fibers (Table 1.2). [39,41,53,54,45–52] However, many of these authors also report fiber damage and reduced mechanical properties which they hypothesize are caused by high temperatures, high flow rates during fluid infiltration and fluid removal, and/or the presence of moisture in the fibers during treatment. The presence of moisture in $scCO_2$ results in the formation of carbonic acid which results in acid hydrolysis and has been shown to induce extraction of material from natural

fibers. [55] In addition, high flow rates have been shown to be effective at foaming of polymers and exfoliation of nanomaterials during supercritical fluid processing of nanocomposites. [56–58] In these processes, the rapid depressurization of the system could be causing rapid fluid expansion, resulting in local plastic deformation and formation of bubbles in the fibers. Additionally, high temperatures (above 130°C) have been previously shown to result in slow decomposition of the lignocellulosic components of natural fibers. [59–61]

Table 1.2: Summary of prior work of use of supercritical CO_2 ($scCO_2$) to treat natural fibers

Fiber Type	Fluid type	Treatment Conditions Reported	Result	Reference
Cotton, Viscose	$scCO_2$	160°C 30 MPa 4 hr	Depolymerization of cellulose attributed to high temperatures and long duration of treatment	[39]
Rice Husk	$scCO_2$ + water	80°C 27 MPa 10 min	Delignification of biomass. No significant change to enzymatic digestibility or crystallinity	[40]
Hemp Fibers	$scCO_2$	129°C 15 MPa 17 hr	Reduction in hydrophilicity. Extraction of hemicellulose and pectin. Reduction in tensile modulus and elongation.	[41]
Flax Yarns	$scCO_2$	130°C 5 MPa 170 min Rapid infusion	Removal of hemicellulose, lignin, pectin. Reduction in interfacial adhesion with epoxy.	[42]
Flax Rove	$scCO_2$	70-120°C 28 MPa 90 min Rapid infusion	Damage to fiber surface, increasing with treatment temperature. Increase in fiber crystallinity. Improved thermal properties.	[43]

1.4 Thesis Overview

This work seeks to develop a novel technique to improve the mechanical properties of flax fibers, resulting in fibers more suitable for use in structural polymer composites. Several treatments are explored within this body of work. Treatments which were successful in improving flax fiber mechanical properties were studied in depth to understand the resulting changes to fiber structure, morphology, and/or chemistry. Additionally, unidirectional polymer

composites were created with improved flax fibers to understand how fiber treatments affect the final composite performance.

In Chapter 2, flax fibers and pectin films were treated with nanomaterials in the presence of $scCO_2$ to attempt to incorporate nanomaterials within the fiber structure. Fibers were characterized via single fiber tensile testing, visualized using plasma focused ion beam scanning electron microscopy (PFIB-SEM), and the location of nanomaterials determined via energy dispersive x-ray spectroscopy (EDS). Modifications to treatments and nanoparticle chemistry were made based on lessons learned. The incorporation of nanoparticles in pectin films was determined via Time-of-Flight Secondary Ion Mass Spectrometry (TOF-SIMS) and the effects of pressure and duration of treatment were evaluated. An optimized set of conditions capable of successfully introducing nanomaterials into pectin were determined.

In Chapter 3, flax fibers were treated using the optimized set of conditions determined in Chapter 2. Fiber mechanical performance was improved upon treatment. Evaluation of nanoparticle location within the fiber structure were explored via PFIB-SEM, EDS, and transmission electron microscopy (TEM). Changes to fiber morphology, structure, and chemistry were explored: changes to porosity were measured via optical microscopy and nitrogen physisorption; changes to crystallinity were determined via x-ray diffraction (XRD); fiber density was measured using gas pycnometry; and bulk chemistry was analyzed using attenuated total reflectance Fourier transform infrared spectroscopy (FTIR). Two potential mechanisms for the improvements observed were proposed.

In Chapter 4, treated flax fibers were used to create 30 vol% unidirectional epoxy composites to explore how fiber treatment affects final composite tensile properties. Interfacial shear strength between fibers and epoxy was evaluated from fiber pull-out testing. Composites

created with treated fibers exhibited higher modulus and strength than untreated fibers. Fiber size distribution within each composite was characterized and used to create a model to predict composite modulus; the rule-of-mixtures (ROM) was modified to consider fiber size as a non-negligible component of natural fiber composite property prediction.

Chapter 5 summarizes the contributions of this thesis to the literature and discusses potential future directions for this work, including potential treatments with different fluid chemistries and different sized nanoparticles.

Chapter 2 Optimization of Nanoparticle Infiltration via $scCO_2$ Treatment

2.1 Introduction

Prior work has shown that the failure of flax technical fibers initiates in the middle lamella. [26,27] The middle lamella is the pectin-rich 50 nm thick interface between elementary fibers (cells) in a technical fiber. [16–19] Prior work to improve technical fiber mechanical properties has been focused mainly on chemical treatments or processing techniques, and have not been successful at creating technical fibers competitive with glass fiber for structural polymeric composites. [30–33] However, nanomaterials have been shown to improve the performance of polymeric materials, even at very low loading levels. [62] Because fiber failure is known to initiate within the middle lamella, we hypothesized that reinforcement of the interfaces between elementary fibers to either a) stiffen the middle lamella or b) bridge the middle lamella to enhance load transfer between adjacent elementary fibers could delay crack initiation and enhance fiber mechanical properties.

Supercritical CO_2 ($scCO_2$) has been shown to be highly effective at intercalating between amorphous polymer chains, resulting in swelling of the polymer, reducing polymer viscosity, reducing glass transition temperature, and increasing mass transport within the swollen polymer network. [43,47,49,55,56,63–66] Because the middle lamella consists mainly of amorphous polymers (pectin, lignin), the author hypothesized that $scCO_2$ could be used to strategically swell the middle lamella, increasing mass transport between elementary fibers and allowing for reinforcing agents to be introduced. A schematic of the hypothesized mechanism is shown

Figure 2.1, in which the middle lamella is swollen and infiltrated with nanomaterials, via treatment in $scCO_2$.

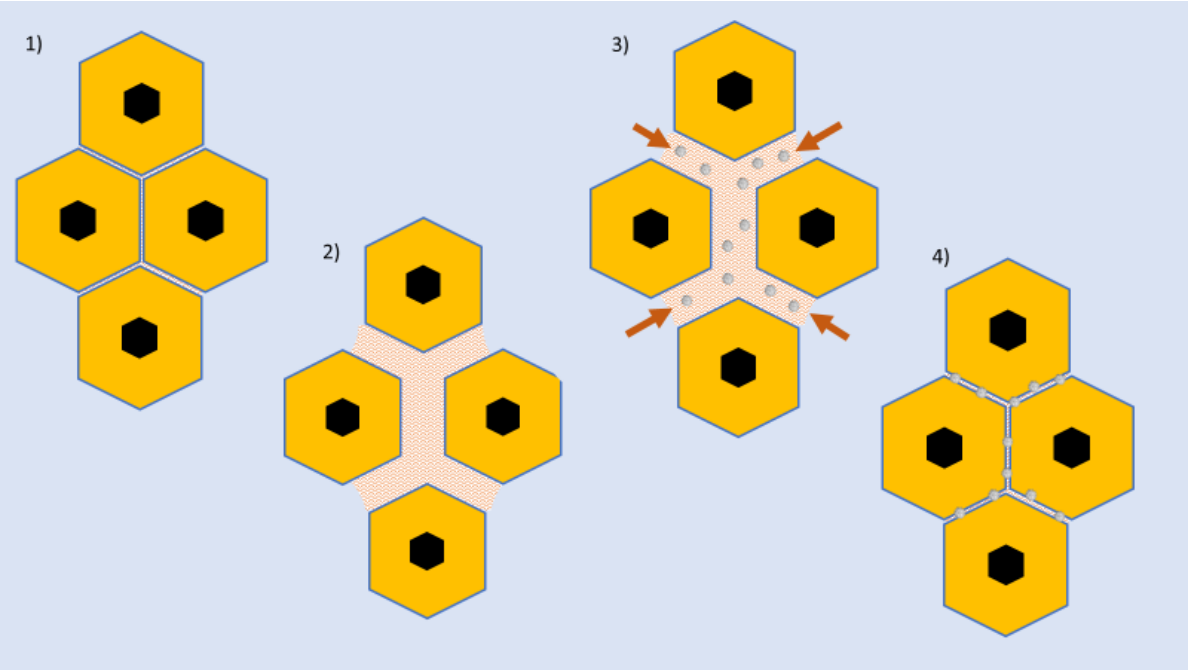

Figure 2.1: Schematic for infiltration of the middle lamella with reinforcement, such as nanoparticles. 1) Initial technical fiber. 2) Swelling of amorphous middle lamella with $scCO_2$. 3) Infiltration of middle lamella with reinforcement, such as nanoparticles. 4) Collapse of the middle lamella upon controlled depressurization and release of $scCO_2$, trapping nanoparticles within fiber structure.

Prior work has evaluated the use of $scCO_2$ as a means for solvent-less dyeing of natural fibers, and several authors have attempted to use $scCO_2$ for the extraction or removal of non-cellulosic components from natural fibers (Table 1.2). [39,41,53,54,45–52] However, many of these authors also report fiber damage and reduced mechanical properties which they hypothesize are caused by high temperatures, high flow rates during fluid infiltration and fluid removal, and/or the presence of moisture in the fibers during treatment. The presence of moisture in $scCO_2$ results in the formation of carbonic acid which results in acid hydrolysis and subsequent extraction of material from natural fibers. [55] In addition, high flow rates have been

shown to be effective at foaming of polymers and exfoliation of nanomaterials during supercritical fluid processing of nanocomposites. In these processes, the rapid depressurization of the system results in rapid fluid expansion within the polymer or nanomaterial, causing plastic deformation. [56–58] Additionally, high temperatures have been shown to result in slow decomposition of the lignocellulosic components of natural fibers. [59–61]

In this chapter, treatment of technical fibers in $scCO_2$ at low temperatures, via low flow rates, and without moisture in the system is explored, to attempt to prevent the damage mechanisms previously reported. Treatment of pectin films as a model material for the middle lamella was explored to understand the effect of different treatment conditions on the infiltration of pectin with nanoparticles. Additionally, because natural fibers are highly hydrophilic, aqueous pre-treatment of flax fibers via dip-coating and sonication were explored as a means of introducing nanomaterials into large cracks in the technical fibers prior to further infiltration via $scCO_2$ treatment. Iterative experimental designs enabled selection of treatment conditions via lessons learned from analysis of fibers after each treatment performed.

2.2 Experimental

2.2.1 Materials

Long-line technical Agatha flax fibers were cultivated and extracted by Fibrevolution, LLC, (Portland, OR, USA). The flax stems were dew-retted, hand-scutched, and hand-hackled to yield technical fibers used throughout this study.

Low-methoxyl citrus pectin and monocalcium phosphate were used to form pectin films via pectin hydrogels (Pomona's Universal Pectin, Oakhurst, CA, USA). To create pectin hydrogels, a 0.103 g/mL solution of low-methoxyl pectin was created. Pectin was added to

water held at 100°C and stirred until dissolved. A 0.001 g/mL (0.0042 M) solution of monocalcium phosphate was also created. Monocalcium phosphate was dissolved in water at 23°C and stirred with a magnetic stir bar. The solution of monocalcium phosphate was brought to a boil, the pectin solution added, and the newly formed pectin + monocalcium phosphate solution was brought to a boil. The pectin + monocalcium phosphate solution was removed from heat and poured to fill 10 ml polystyrene molds (8 mm x 41 mm x 41 mm Fisherbrand Polystyrene Weighing Dishes, Waltham, MA, USA). The molds were placed in a refrigerator kept at 1°C to form a hydrogel which remained in the refrigerator for 1 week to allow the hydrogel to dry into a film. After drying, the pectin films (~0.05 mm thick) were cut into ~1-cm^2 pieces for treatment and evaluation.

Titanium dioxide anatase nanoparticles (TiO_2, 5nm, US Research Nanomaterials, Inc, Houston, TX, USA) and iron oxide nanoparticles (Fe_3O_4, 3nm, US Research Nanomaterials) were used for fiber treatments in this study.

2.2.2 Supercritical Fluid Treatment

A pressure vessel was used to treat flax fiber and pectin film samples as shown in Figure 2.2. A magnetic stir rod was placed on the bottom of the vessel beneath a cage of fiberglass mesh (~1 cm openings) to allow for continuous stirring of the fluid throughout the treatment. When nanomaterials were added to the pressure vessel directly, they were placed directly in the bottom of the vessel at the start of the experiment to avoid contact with the sample before beginning treatment. Prior to treatment, fibers were cut to 6 cm lengths and dried for 2-4 hours in a convection oven at 60°C. Fibers (or pectin samples) were placed on top of the fiberglass mesh to prevent damage from the stir-rod during infusion, and the pressure vessel was sealed. Prior to beginning pressurization, the chamber was purged for at least 5 min with the gas being used for

treatment. Pressurization occurred slowly via a gas booster pump, at a pressurization rate of 350 kPa/min. Temperature of the vessel was maintained via a band heater held at 60°C. Depressurization was controlled to a rate of 2 MPa/min.

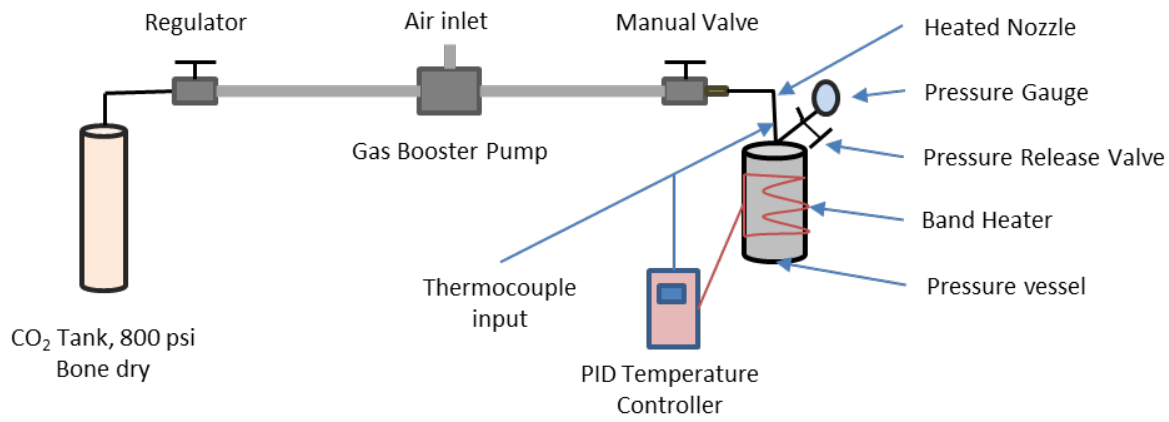

Figure 2.2: Design of equipment and pressure vessel used to incorporate nanomaterials within fiber samples using supercritical CO_2

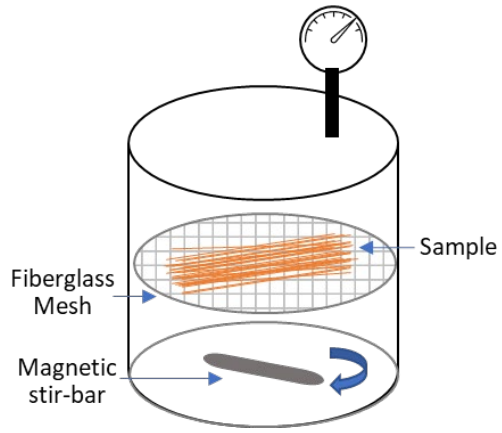

Figure 2.3: Inside of pressure vessel during supercritical fluid treatment. Sample was placed on top of fiberglass mesh and a magnetic stir-bar was used to agitate the fluid for the duration of treatment.

2.2.3 Treatment of Pectin films in scCO₂

Direct treatment of pectin films with 5 nm TiO_2 nanoparticles in supercritical fluid (without any aqueous pre-treatment) was performed according to the experimental conditions

outlined in Table 2.1. TiO_2 nanoparticles were first poured into the pressure vessel. The sample being treated was then placed on top of the fiberglass mesh, and the vessel was sealed and pressurized. The weight ratio of nanoparticles to sample was held at approximately 1:1. A schematic summarizing the process flow for the treatment of pectin films is shown in Figure 2.4.

Table 2.1: Experimental design for incorporation TiO_2 nanoparticles within pectin films via infusion in supercritical CO_2.

Sample Name	Fluid Type	Pressure [MPa]	Time Duration [hours]	Temperature [°C]	Depressurization rate [MPa / min]	Nanoparticle Type
Untreated Pectin	-	Untreated	-	-	-	-
Pectin 8MPa 4hr	$scCO_2$	8	4	60	2	5nm TiO_2
Pectin 28MPa 4hr	$scCO_2$	28	4	60	2	5nm TiO_2
Pectin 10MPa 24hr	$scCO_2$	10	24	60	2	5nm TiO_2
Pectin 28MPa 24hr	$scCO_2$	28	24	60	2	5nm TiO_2

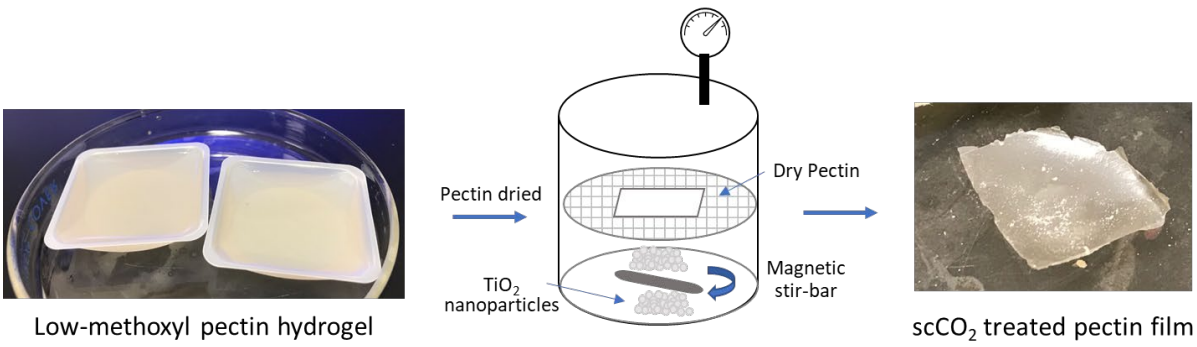

Figure 2.4: Process flow for creation and treatment of pectin films directly in $scCO_2$ in the presence of TiO_2 nanoparticles.

2.2.4 Aqueous Nanoparticle Solution Pre-Treatments

Flax fibers underwent aqueous pre-treatments with both Fe_3O_4 and TiO_2 nanoparticles as shown in Table 2.2. Nanoparticles were dispersed in deionized water at 3 vol% and then ultrasonicated for 5 minutes to ensure particle dispersion. Fibers were dip coated in the solution for 5 minutes. Those fibers which underwent sonication remained in solution after dip coating and were ultrasonicated for 10 minutes. After the specified aqueous solution treatments, the fiber sample was placed in an oven at 80°C for 1-2 hr until dry. Fibers which underwent further treatment in supercritical carbon dioxide ($scCO_2$) were placed into a pressure vessel in their dry state. A schematic summarizing the process flow for aqueous pre-treatment followed by $scCO_2$ treatment is shown in Figure 2.5.

Table 2.2: Experimental design for aqueous nanoparticle treatment using Fe_3O_4 and TiO_2 nanoparticles followed by supercritical fluid treatment of flax fibers.

	Nanoparticle Solution	**Dip Coat Duration [min]**	**Sonication Duration [min]**	**$scCO_2$ Treatment?**	**Pressure [MPa]**	**Duration [hours]**	**Temperature [°C]**
Untreated	-	-	-	-	-	-	-
Fe_3O_4 Dip Coated	3 vol% 3nm $Fe_3O_4 + H_2O$	5	-	-	-	-	-
Fe_3O_4 Dip + 28MPa $scCO_2$		5	-	Yes	28	24	60
Fe_3O_4 Dip + Son		5	10	-	-	-	-
Fe_3O_4 Dip + Son + 28MPa $scCO_2$		5	10	Yes	28	24	60
TiO_2 Dip Coated	3 vol% 5nm $TiO_2 + H_2O$	5	-	-	-	-	-
TiO_2 Dip + 28MPa $scCO_2$		5	-	Yes	28	24	60

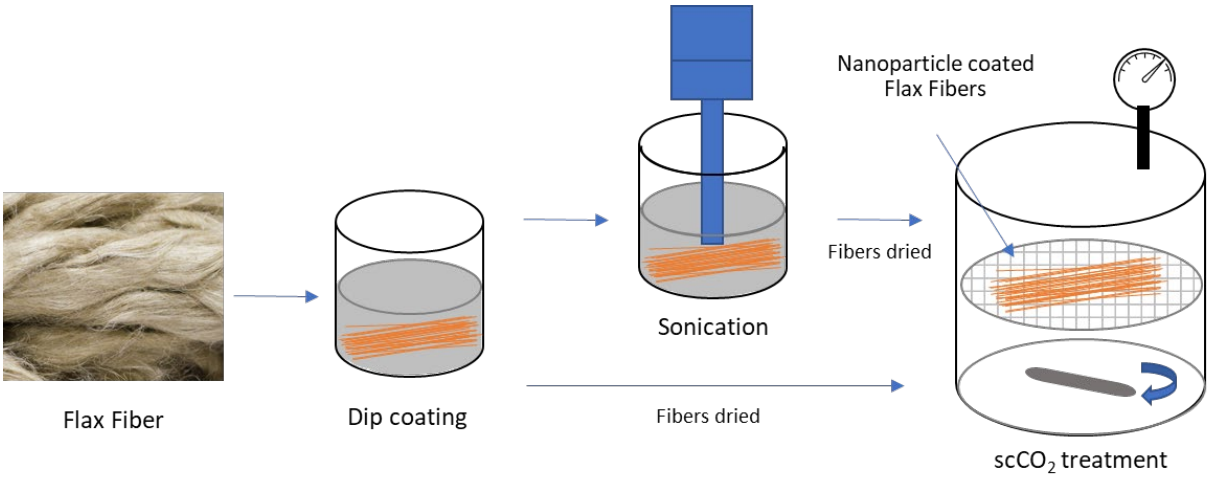

Figure 2.5: Process flow for treatment of flax fibers via aqueous pre-treatments and $scCO_2$, as specified in Table 2.2.

2.2.5 Time-of-Flight Secondary Ion Mass Spectrometry (TOF-SIMS)

To detect TiO_2 nanoparticles in the pectin layers, specimens were prepared and analyzed by TOF-SIMS using a Physical Electronics TRIFT-IV mass spectrometer. Pectin films were adhered between two polypropylene (PP) sheets and microtomed edge-on to smooth the surface (technique previously described by Gerlock, et. al.) [67] A 30 keV Au+ primary ion beam under static conditions was used to generate positive secondary ion spectra and images. The total ion dose was kept below 2×10^{10} ions/ cm^2. A region of 200 µm x 200 µm was used to collect images for each sample using the unbunched mode to maximize spatial resolution. An electron flood gun was employed to stabilize the charge on the system during data acquisition. Secondary ions were collected at a mass resolution (m/Δm) between 4000–8000 over a range of 0–1850 m/z. Positive spectra m/z values were mass calibrated using CH+, C2H3+, C3H5+, C5H7+ peaks. Mass calibration errors were typically below 20 ppm.

For each sample, ImageJ Fiji software was used to quantify the intensity of the Ti ion signal in positive secondary ion images, with separate analysis of the pectin and PP regions of

each image. The signal in the pectin and PP regions were color-averaged prior to conversion to 8-bit grayscale. The color scale on positive ion image was also converted to 8-bit grayscale, enabling conversion of a gray value to an intensity value. This scale was compared to the average grayscale value within each pectin and PP region of the images, allowing quantitation of the signal intensity. The pectin intensity value was normalized to the PP intensity value for each image to allow for sample-to-sample comparisons.

2.2.6 Single Fiber Tensile Testing

Fibers were mounted in paper frames as shown in Figure 2.6 per ASTM C1557-20.[68] To glue the fibers to the frame and prevent slipping during testing, 1-2 drops of 3M General Use No Run Super Glue were applied to the top and bottom edges of the window. A second frame was applied on top of the first to secure the fiber. At least 20 fibers were mounted and tested per sample. After mounting, all fibers were conditioned in a desiccator box held at 25% RH for at least 24 hours prior to testing. All fibers were tested at a gauge length of 10 mm.

The cross-sectional area of each fiber mounted for single fiber tensile testing was obtained via imaging of fiber diameters using an Olympus inverted GX51 microscope at 5x magnification followed by image analysis using the software ImageJ Fiji. The diameter of each fiber was measured along two axes as shown in Figure 2.6. At least 8 measurements were taken along the length of the fiber on each axis and averaged. The fiber cross-sectional area was approximated as the area of an ellipse via Equation 1, as shown in prior studies.[69]

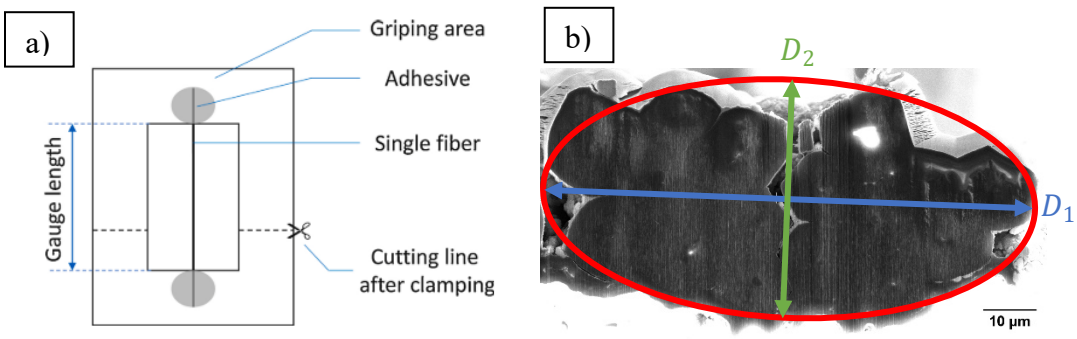

Figure 2.6: a) Schematic of paper mount used for single fiber tensile testing of flax fibers. The gauge length was 10mm for all samples tested.[70] b) Schematic of diameter measurement locations on technical fiber and area measurement via approximation of fiber cross-section as ellipse.

$$A = \pi \cdot \frac{D_1}{2} \cdot \frac{D_2}{2} \quad (1)$$

Single fiber tensile tests of technical flax fibers were performed according to ASTM C1557-20 on a TA XT Plus Texture Analyzer using a 5kg load cell and an extension rate of 0.01 mm/s.[68] The maximum crosshead extension (ΔL) and maximum force (F) were determined for all fibers. The machine compliance (C_s) was determined experimentally and found to be 0.009 mm/N. The corrected fiber elongation (Δl) and fiber strain ($\frac{\Delta l}{l_0}$) were determined via the Equations 2-3 below.

$$\Delta L = \Delta l + C_s \cdot F \quad (2)$$

$$\frac{\Delta l}{l_0} = \frac{F}{AE} \quad (3)$$

2.2.7 Peel Testing

To prepare fibers for peel testing, technical fiber ends were gently compressed to induce a split of the technical fiber. The split portion of the technical fiber was gently pulled to allow for

gripping and the remaining fiber was taped under tension to a glass slide, leaving ~30 mm of fiber between taped ends for testing. A small drop of 3M General Use Super Glue was applied near the tape to ensure that the fiber remained on the glass surface during testing.

A TA XT Plus Texture Analyzer was used to perform 90 degree peel tests (N = 4) on the prepared fibers using a 5-kg load cell and a peel rate of 0.5 mm/s (Figure 2.7). Fibers were peeled for the full length of the prepared specimen. After testing, the diameter of the peel was measured via optical microscopy using an Olympus inverted GX51 microscope at 5x magnification followed by image analysis using the ImageJ Fiji. The maximum force required to separate the peel from the fiber was determined, and values were normalized to the peel width removed for each fiber.

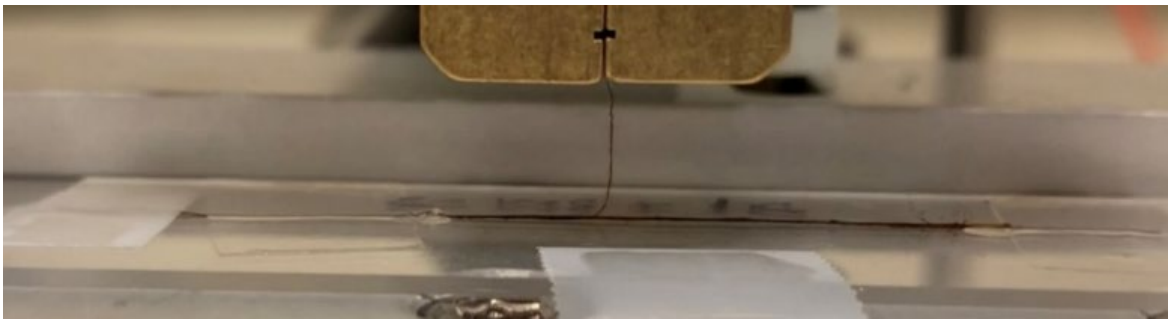

Figure 2.7: Peel test performed on technical flax fibers. A small portion of fiber was peeled away from the remaining technical fiber and the maximum force was recorded. Values were subsequently normalized to the peel diameter.

2.2.8 Plasma Focused Ion Beam Scanning Electron Microscopy (PFIB-SEM)

A Thermo Fisher Helios G4 Plasma Focused Ion Beam (PFIB) Scanning Electron Microscope (SEM) with a ThermoFisher Pathfinder Energy Dispersive Spectroscopy (EDS) UltraDry 30M system was used to evaluate fiber samples after treatment. Samples were mounted on conductive tape and gold coated to enable evaluation. Before cutting, fibers were

coated with a carbon and platinum protective cap to prevent surface deformation. Cuts were made via an inductively coupled xenon gas plasma ion beam at a maximum beam current of 60 nA. SEM images of fiber surfaces and cross-sections were taken using 5kV accelerating voltage and 0.2 nA current.

2.2.9 Energy Dispersive X-Ray Spectroscopy (EDS)

EDS analysis and EDS mapping were conducted to visualize the location of nanoparticles within fiber cross-sections (N = 3). For SEM with EDS analysis, conditions were 15kV acceleration voltage, 1.6nA current, and a working distance of 4mm. EDS conditions were optimized to maximize global counts per second (~5000-10000 counts/s).

2.3 Results and Discussion

2.3.1 Treatment of Pectin Films with TiO_2 in $scCO_2$

Experiments were initially conducted with pectin films as a model material for the middle lamella. Pectin films were created and then treated with 5 nm TiO_2 nanoparticles in supercritical CO_2 per the experimental design in Table 2.1. TOF-SIMS was used to evaluate the infiltration of pectin films with nanoparticles following treatment, by analyzing the Ti ionization signal in cross-sections of the pectin films.

After treatment at the lowest pressure condition and the shortest duration evaluated in this study (Pectin 8MPa 4hr), the Ti ionization signal from the pectin films was not significantly different than the control pectin film (Figure 2.8 - Figure 2.9). A few small agglomerates were detected on the surface of the film, after this treatment (Figure 2.9). With increasing pressure (Pectin 28MPa 4 hr), the Ti signal increased, suggesting that the higher pressure may improve

infiltration of nanoparticles (Figure 2.10). Treatment for a longer duration (24 hrs) resulted in even higher Ti ionization signals (Figure 2.11-Figure 2.12). Figure 2.13 summarizes quantitative results for Ti ionization signal from image analysis of TOF-SIMS images. Overall, image analysis confirms the presence of TiO_2 within pectin films treated at 28MPa for 4 hours, 10MPa for 24 hours, or 28MPa for 24 hours. Higher pressure and longer treatment duration were shown to result in stronger Ti signal from within the pectin films, suggesting that higher pressures and longer durations are more effective at infiltration TiO_2 nanoparticles into pectin films.

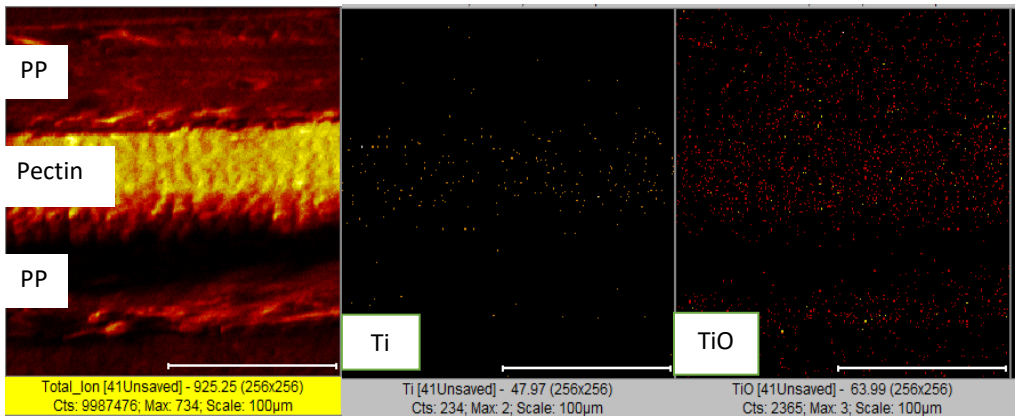

Figure 2.8: TOF-SIMS images of Untreated pectin film. Cross-sections showed very low background ionization intensities of Ti and TiO signals.

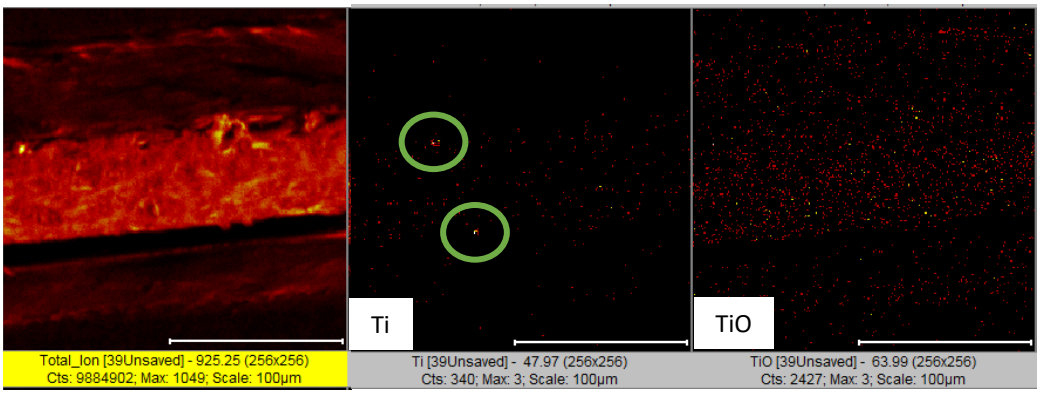

Figure 2.9: TOF-SIMS images of a pectin film treated with TiO_2 nanoparticles in $scCO_2$ for 4 hours at 8MPa (Pectin 8MPa 4hr). Bright spots in the Ti image show the presence of TiO_2 agglomerates at the film surface.

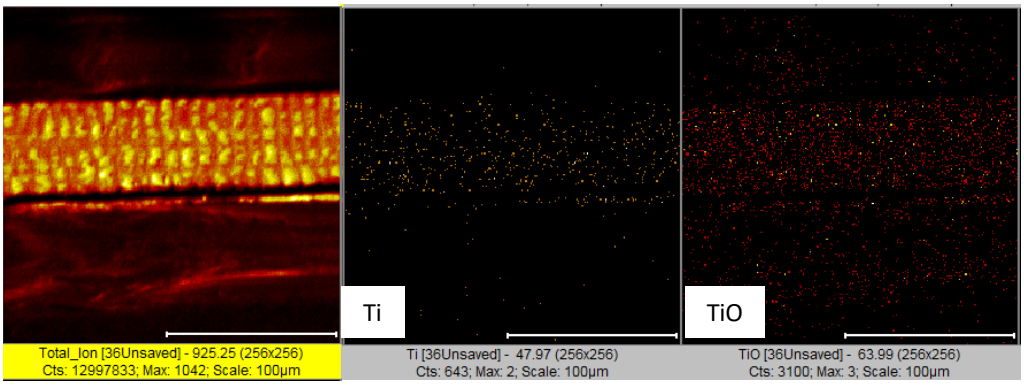

Figure 2.10: TOF-SIMS of a pectin film treated with TiO_2 nanoparticles in supercritical CO_2 for 4 hours at 28MPa (Pectin 28MPa 4hr). The Ti and TiO images show that nanoparticles are dispersed within the pectin film.

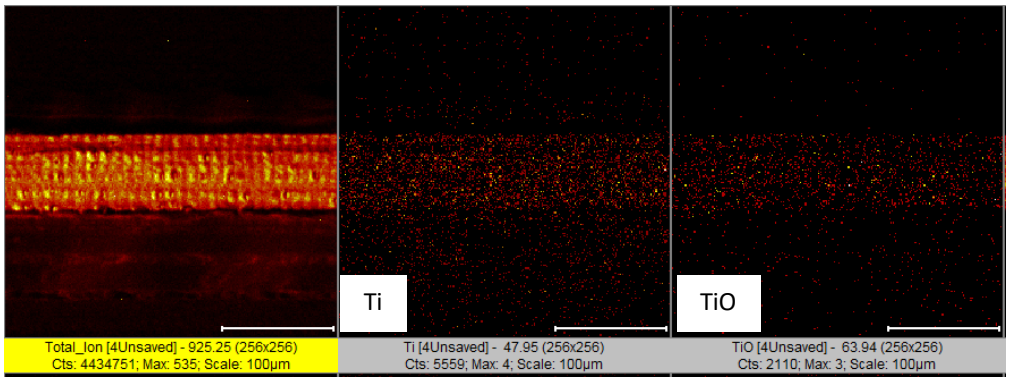

Figure 2.11: TOF-SIMS of a pectin film treated with TiO_2 nanoparticles in supercritical CO_2 for 24 hours at 10MPa (Pectin 10MPa 24hr). These images show more TiO_2 nanoparticles within the pectin film as the duration of treatment increases.

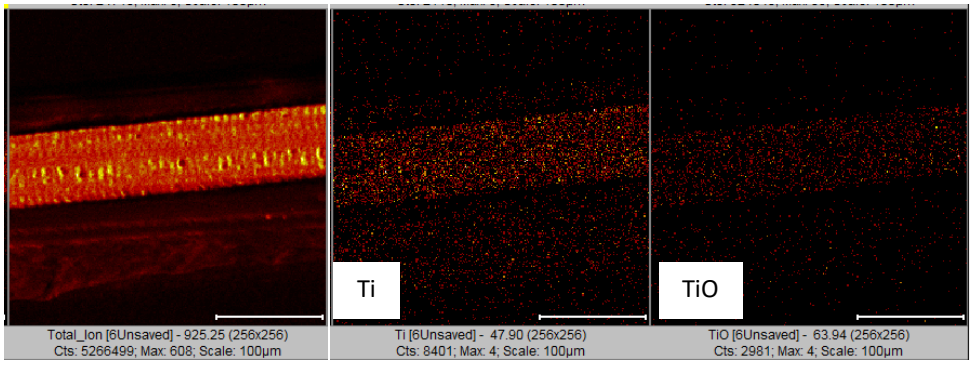

Figure 2.12: TOF-SIMS of pectin film treated with TiO_2 nanoparticles in supercritical CO_2 for 24 hours at 28MPa (Pectin 28MPa 24hr). Compared to the control and other treatment conditions, these images show more TiO_2 nanoparticles within the pectin film as the pressure and duration of treatment is increased.

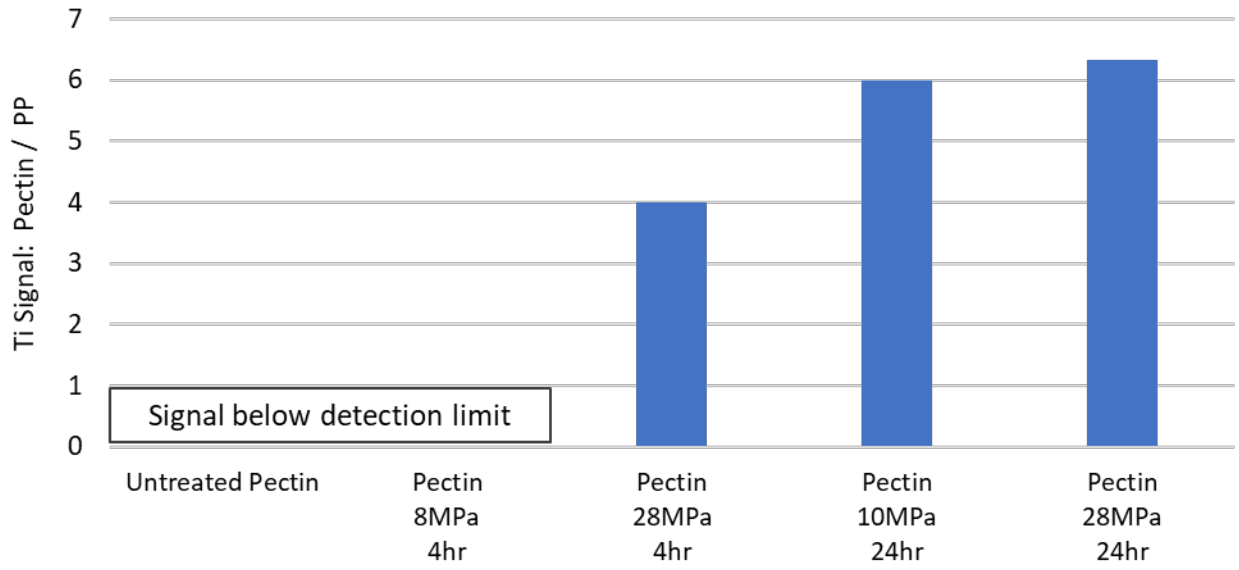

Figure 2.13: Results from quantitation of Ti ionization signal in pectin films via TOF-SIMS, reported as Ti signal in pectin normalized to Ti signal in PP (Pectin signal / PP signal).

2.3.2 Aqueous Pre-Treatments with Nanoparticles

Because of the hydrophilicity of natural fibers, aqueous pre-treatment of flax fibers via dip-coating and sonication were explored as a means of introducing nanomaterials into large cracks in the technical fibers prior to further infiltration via $scCO_2$ treatment. The tensile modulus and ultimate strength of flax fibers treated with Fe_3O_4 nanoparticles per Table 2.2 are shown in Figure 2.14. Results from experiments involving aqueous pretreatment of flax fibers with Fe_3O_4 nanoparticles via dip-coating (Fe_3O_4 Dip Coated) and/or sonication (Fe_3O_4 Dip + Son) showed comparable or slightly reduced tensile modulus in comparison to untreated flax fiber. Dip-coating alone resulted in improvements to fiber stiffness, but further treatment (via sonication and/or $scCO_2$) resulted in reductions in stiffness. All treatments resulted in strength reductions relative to untreated fibers.

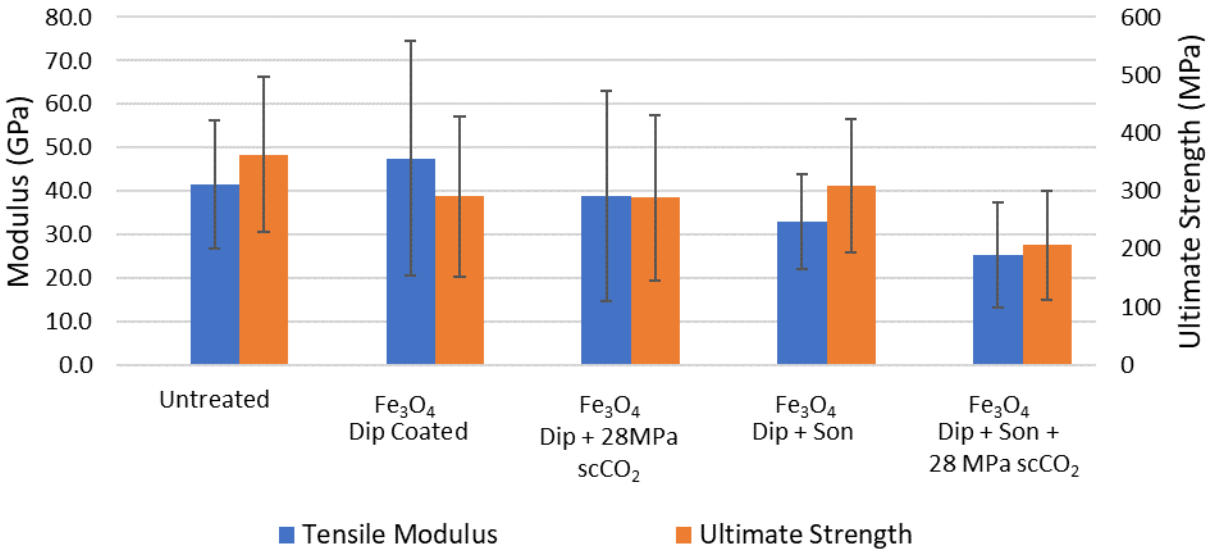

Figure 2.14: Single fiber tensile properties of untreated flax fibers compared to fibers treated by dip-coating in a 3 vol% aqueous solution of Fe_3O_4 nanoparticles for 5 minutes. Additional treatments of dip-coated fibers were evaluated, including sonication in the nanoparticle solution for 10 minutes and/ or treatment with supercritical CO_2 for 24 hours at 60°C.

Micrographs of fiber surfaces before and after for both Fe_3O_4 Dip + Son and Fe_3O_4 Dip + Son + 28 MPa $scCO_2$ treatment showed significant agglomeration of Fe_3O_4 nanoparticles on the fiber surface after treatments (Figure 2.15, Figure 2.16). In addition, the formation/presence of numerous microcracks was observed after treatment with sonication. It is possible that the superparamagnetic behavior of 3 nm Fe_3O_4 nanoparticles caused the formation of large particle agglomerates that caused cracking of the fiber upon high pressure treatment with $scCO_2$. This observation is consistent with prior work by Anurakparadorn, et. al. showing that the magnetic behavior of cobalt ferrite nanoparticles resulted in significant agglomeration in solution. [71]

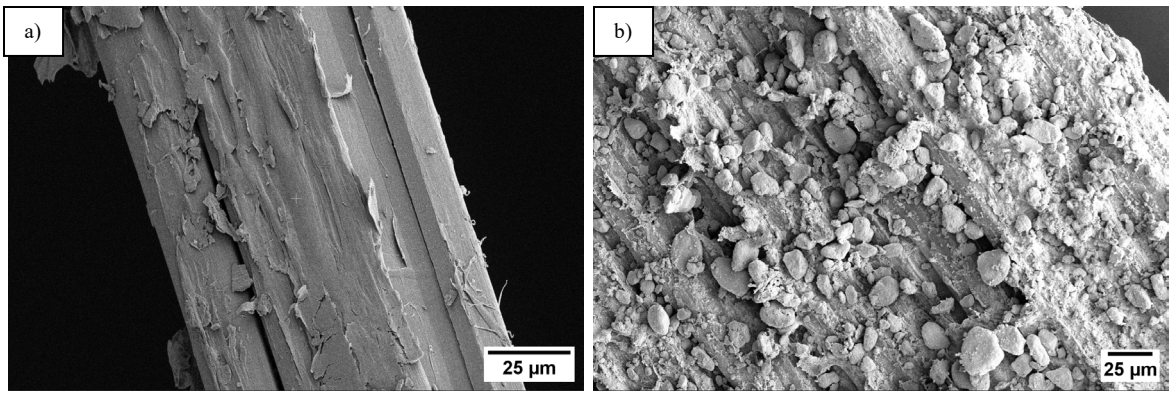

Figure 2.15: SEM micrographs of (a) the surface of an untreated flax fiber and (b) the surface of Fe_3O_4 Dip + Son fiber showing significant nanoparticle agglomeration.

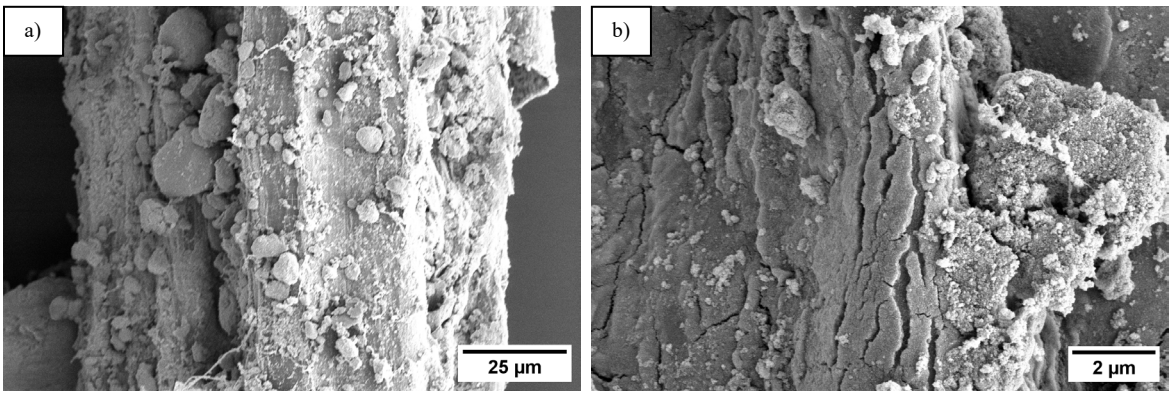

Figure 2.16: Surfaces of Fe_3O_4 Dip + Son treated fibers, showing (a) significant nanoparticle agglomeration on the fiber surface and (b) microcracks on the fiber surface.

Cross-sections of the fibers evaluated with EDS (Figure 2.17 - Figure 2.20) showed significant Fe_3O_4 agglomeration on the surface of fibers and within fiber cracks after Fe_3O_4 Dip Coating, Fe_3O_4Dip + Son, and Fe_3O_4Dip + Son + 28MPa $scCO_2$ treatments. EDS quantification of iron content on the inside of the fiber cross-section after each treatment step are summarized in Table 2.3. Dip + Son treatment was shown to be capable of introducing small quantities of Fe_3O_4 inside the fiber cross-section (0.23 at%). The presence of Fe with the fiber structure after Fe_3O_4 Dip + Son treatment did not coincide with increases to fiber modulus or strength (Figure 2.14), suggesting that particles were able to enter large cracks but not improve load transfer

between elementary fibers via crack bridging or reinforcement of the middle lamellae. However, additional treatment with $scCO_2$ (Fe_3O_4 Dip + Son + 28MPa $scCO_2$) resulted in a reduction in the quantity of Fe_3O_4 in the cross-section of the fiber (0.17 at%). It appears that sonication drove particles into the fiber cracks and/or within the fiber structure, but further $scCO_2$ treatment and/or the subsequent depressurization, may have removed some nanomaterials from the fiber structure.

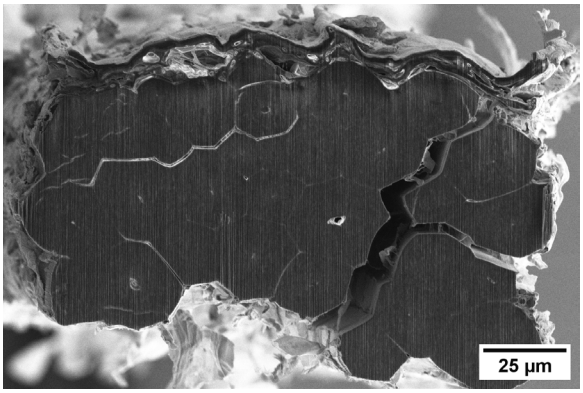

Figure 2.17: PFIB-SEM image of Untreated fiber cross-section, showing cellular structure.

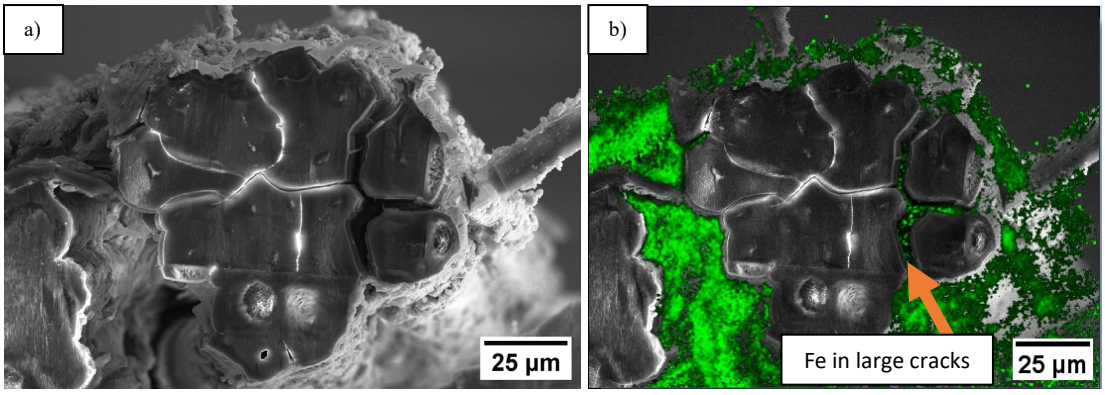

Figure 2.18: PFIB-SEM image of Fe_3O_4 Dip Coated fiber (a) cross-section and (b) EDS map showing the presence of iron (in green) on the fiber surface and within large fiber cracks (as indicated with arrow).

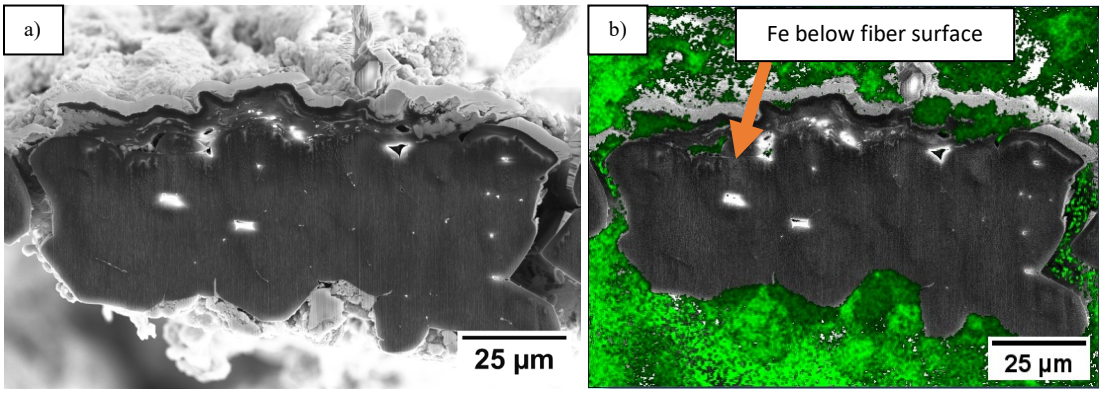

Figure 2.19: PFIB-SEM image of Fe_3O_4 Dip + Son fiber (a) cross-section and (b) EDS map showing the presence of iron (in green) on the fiber surface and within the fiber cross-section, near the fiber surface (as indicated with arrow)

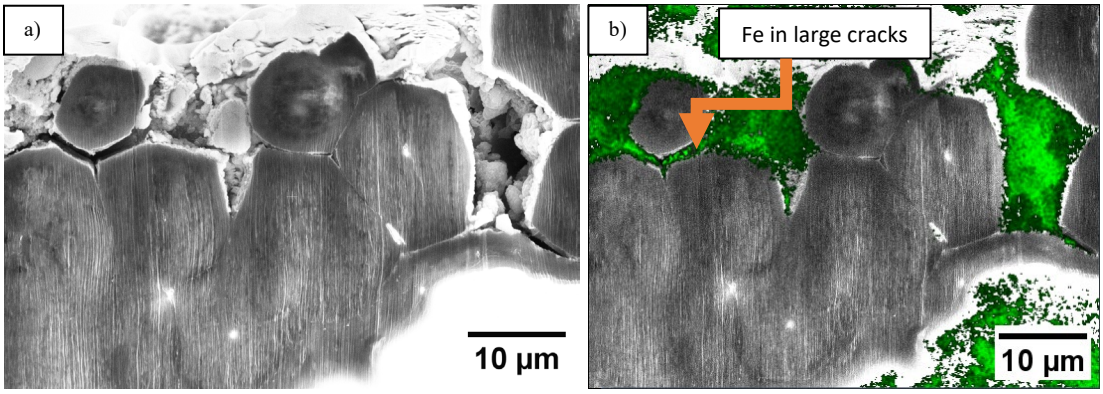

Figure 2.20: PFIB-SEM image of Fe_3O_4 Dip + Son + 28MPa $scCO_2$ fiber (a) cross section and (b) EDS map showing presence of iron (in green) from nanoparticle infiltration of larger fiber cracks (as indicated with arrow).

Table 2.3: Results from EDS quantitation of Fe content within cross-sections of flax fibers treated with Fe_3O_4 nanoparticles.

	Fe (Kα) (at%)	**Error (at%)**
Untreated	0	0
Fe_3O_4 Dip Coated	0	0
Fe_3O_4 Dip + Son	0.228	0.040
Fe_3O_4 Dip + Son + 28MPa $scCO_2$	0.168	0.033

Peel tests were conducted on fibers in which nanoparticles were detected via EDS to quantify the adhesion between elementary fibers into the technical fiber. The average peel force required to separate each technical fiber was measured and normalized to peel width (Table 2.4). The force to peel Fe_3O_4 Dip + Son fibers was 22% higher than untreated fibers. However, fibers

which underwent Fe_3O_4 Dip + Son + 28MPa $scCO_2$ treatment required >3x the amount of force to remove the fiber peel, compared to the untreated fiber. (Table 2.4) Interestingly, the maximum peel force for Fe_3O_4 Dip + Son + 28MPa $scCO_2$ treated fibers was higher than fibers which underwent Fe_3O_4 Dip + Son despite there being a lower concentration of nanoparticles detected within its cross-section. These data provide evidence that supercritical fluid treatment of flax fiber may have improved interfacial adhesion between elementary fibers via a different mechanism than reinforcement of the middle lamellae with nanomaterials. The possible mechanism to explain this result is discussed further in Chapter 3.

Table 2.4: Results of peel tests determining the maximum force to separate technical fiber bundles

	Max Force/width [N/mm]	Standard Deviation [N/mm]
Untreated	0.23	0.09
Fe_3O_4 Dip + Son	0.28	0.13
Fe_3O_4 Dip + Son + 28MPa $scCO_2$	0.91	0.72

The internal surface of fibers which had undergone peel testing was also imaged and analyzed using SEM and EDS. Figure 2.21 shows the internal surface of a Fe_3O_4 Dip + Son + 28MPa $scCO_2$ treated fiber. Agglomerates of Fe were observed along the crack lines running lengthwise on the fiber, consistent with PFIB-SEM micrographs showing that this treatment mainly enabled infiltration of nanoparticles into larger cracks.

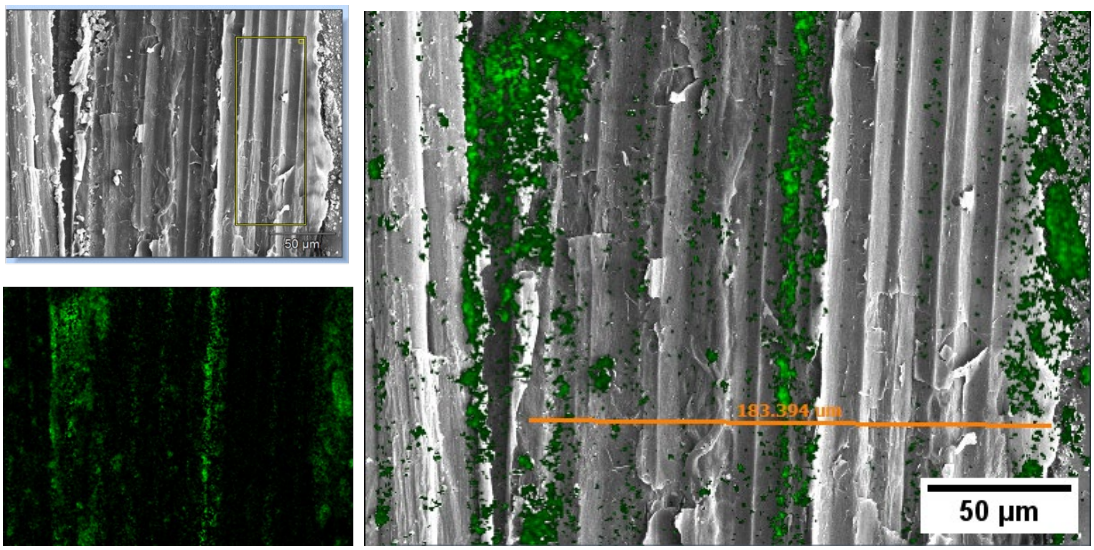

Figure 2.21: SEM-EDS analysis of the Internal surface of Fe_3O_4 Dip + Son + 28MPa $scCO_2$ treated fiber following peel removal of outer surface.

In initial experiments involving treatment of flax fibers with Fe_3O_4 nanoparticles via dip coating, sonication, and $scCO_2$, significant agglomeration of the particles was observed on the fiber surface and microcracks were observed after treatment via sonication. To see if the agglomeration was due to magnetic attraction, a non-paramagnetic nanoparticle (5nm TiO_2) was selected for subsequent experiments to attempt to prevent nanoparticle agglomeration, and sonication as a pre-treatment was removed from the experimental design, per Table 2.2.

Fibers were treated with aqueous solutions of 5 nm TiO_2 nanoparticles via dip-coating and subsequent treatment in $scCO_2$. Aqueous pre-treatment via dip-coating with TiO_2 nanoparticles (TiO_2 Dip Coated) resulted in reductions in tensile modulus and strength compared to untreated flax fiber (Figure 2.22). Further treatment of the TiO_2 dip-coated fibers in $scCO_2$ at 28MPa (TiO_2 Dip + 28MPa $scCO_2$) did not significantly change fiber modulus. The low tensile strength of dip-coated fibers was improved by subsequent $scCO_2$ treatment, but the result was only comparable to untreated fibers. Imaging of the surface of fibers after TiO_2 Dip + 28MPa $scCO_2$ treatment showed that nanoparticle agglomeration was still present (Figure 2.23). It is

possible that the differences in polarity between TiO_2 and water is encouraging nanoparticle agglomeration. The infiltration observed in pectin films via TOF-SIMS may have been enabled by improved dispersion of TiO_2 in non-polar $scCO_2$.

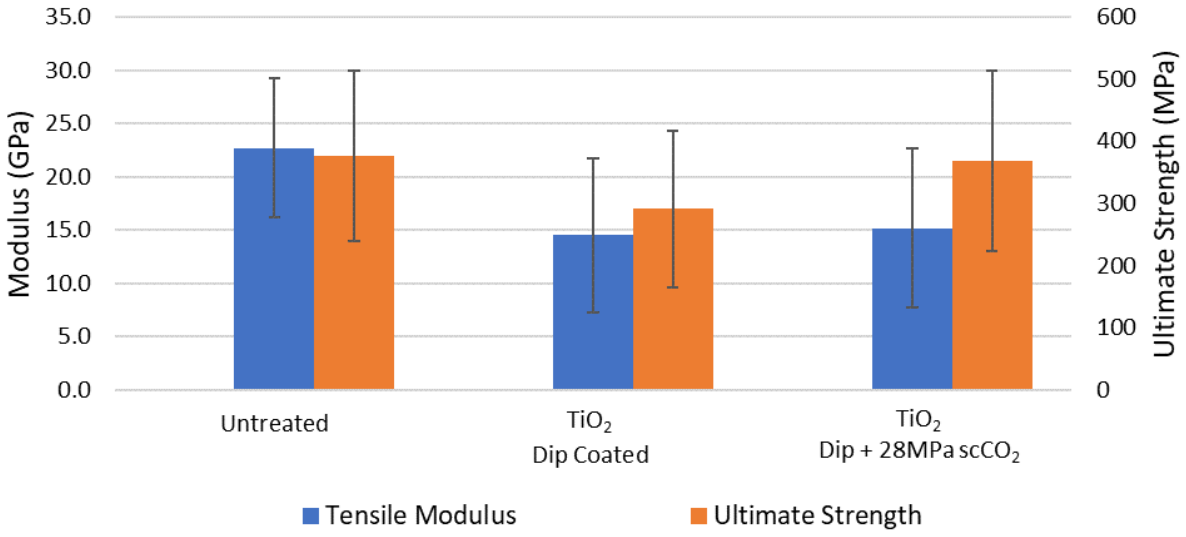

Figure 2.22: Single fiber tensile properties of flax fibers upon dip-coating in a 3 vol% aqueous solution of TiO_2 nanoparticles for 5 minutes followed by treatment in $scCO_2$ for 24 hours at 28MPa $scCO_2$ and 60°C.

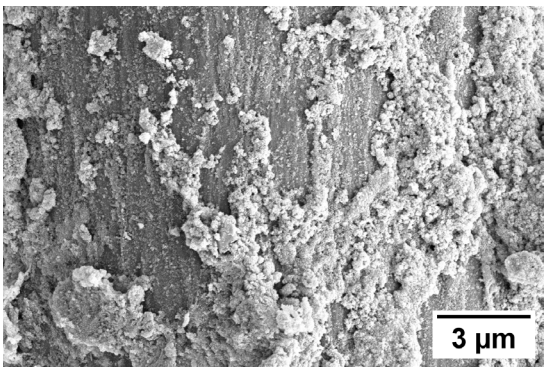

Figure 2.23: Surface of TiO_2 Dip + 28MPa $scCO_2$ treated flax fiber showing nanoparticle agglomeration.

2.4 Conclusions

Initial experiments were performed with the goal of exploring the factors which could affect nanoparticle infiltration of flax and pectin films. Through iterative experiments, it was determined that direct treatment in $scCO_2$ with TiO_2 nanoparticles can result in the incorporation of TiO_2 into pectin. Increasing the duration and pressure of treatment resulted in the incorporation of more TiO_2 within pectin films, with treatment at 28MPa for 24 hours resulting in the strongest Ti signal as detected via TOF-SIMS in pectin films. Exploration of the use of aqueous pre-treatment of flax fibers via dip coating and sonication of fibers in nanoparticle solutions prior to treatment in $scCO_2$ resulted in reductions to fiber mechanical properties. Aqueous pre-treatments resulted in significant nanoparticle agglomeration and fiber surface damage (via sonication). Treatment of flax fibers directly in $scCO_2$ with TiO_2 nanoparticles will be explored in the following chapters to evaluate if the treatment optimized in Chapter 2 (28MPa 24hr) can result in incorporation of nanoparticles within flax fibers and/or improvements to flax mechanical properties.

Chapter 3 Flax Fiber Mechanical Property Enhancement via $scCO_2$ Treatment

3.1 Introduction

In Chapter 2, a variety of treatments for flax fibers and pectin films were explored with the goal of optimizing conditions for infiltration of nanoparticles. Pectin films were used as a model material for the middle lamella within flax fibers. The analysis of treated pectin films with TOF-SIMS showed that $scCO_2$ treatment with TiO_2 nanoparticles could distribute and disperse TiO_2 throughout the pectin film. Higher pressures and longer durations resulted in more TiO_2 infiltration of pectin films, with treatment at 28MPa for 24 hours resulting in the largest amount of nanoparticle incorporation.

In this chapter, $scCO_2$ treatment of flax fibers with TiO_2 nanoparticles is explored, to study the effects of the optimized treatments on flax mechanical properties, structure, morphology and chemistry.

3.2 Experimental

The materials (flax fibers, TiO_2 nanoparticles) used for this work were as described in Chapter 2, Section 2.2.1.

Direct treatment of 6 cm long fibers with 5 nm TiO_2 nanoparticles in supercritical fluid was performed according to the experimental conditions outlined in Table 3.1. TiO_2 nanoparticles were weighed and placed in the pressure vessel. The fibers being treated were placed on top of the fiberglass mesh, and the vessel was sealed and pressurized. The weight ratio

of nanoparticles to fibers was held at approximately 1:1. Equipment design and treatment conditions for $scCO_2$ treatment was as described previously in Chapter 2, Section 2.2.2. A schematic summarizing the process flow for the treatment of flax fibers is shown in Figure 3.1.

Evaluation of fiber mechanical properties was determined via single fiber tensile testing, as previously described in Chapter 2, section 2.2.6. Samples were analyzed by PFIB-SEM + EDS to evaluate the incorporation and distribution of TiO_2 within the fiber, as previously described in Chapter 2 section 2.2.8-2.2.9.

Table 3.1: Experimental design outlining $scCO_2$ treatments performed on flax fibers with and without TiO_2 nanoparticles.

Sample Name	Sample Type	Fluid Type	Pressure [MPa]	Time Duration [hours]	Temperature [°C]	Depressurization rate [MPa / min]	Nanoparticle Type
Untreated	Flax	-	Untreated	-	-	-	-
28MPa	Flax	$scCO_2$	28	24	60	2	-
TiO_2 10MPa	Flax	$scCO_2$	10	24	60	2	5nm TiO_2
TiO_2 28MPa	Flax	$scCO_2$	28	24	60	2	5nm TiO_2

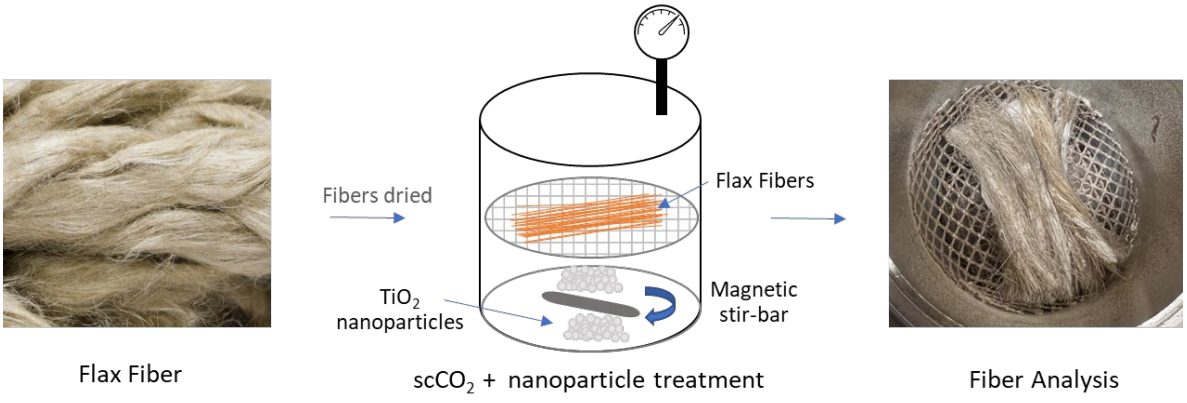

Figure 3.1: Process flow for treatment of flax fibers directly in $scCO_2$, as specified in Table 3.1.

3.2.1 Fiber Fixation, Microtomy, & Image Analysis

Fibers underwent fixation and mounting in polymerase chain reaction tubes (PCR) to enable ultramicrotoming and optical microscopy. Fixation was performed as previously described by Lara-Mondragón, et. al. [72] Fixation began with vacuum infiltration of a solution containing 0.001% (v/v) Tween 20, 2.5% (w/v) Glutaraldehyde, 2% (w/v) Formaldehyde, and 0.025 M piperazine-N,N′-bis(2-ethanesulfonic acid) (PIPES) buffer (pH 7.2) for 2 hours followed by solution replacement and overnight incubation at 4°C. The following day, samples were washed for 10 min in 0.025 M phosphate buffer followed by a 20 min wash in 0.025 M PIPES solution (pH 7.2) and then dehydrated via ethanol series (25%, 35%, 50%, 70%, 80%, 90%, 3x100%). Infiltration with liquid resin white (LRw, EMS #14381) occurred via incubation in solutions of resin and ethanol for 24 hours. The ratio of resin to ethanol was increased each day until fibers were fully infiltrated with resin over the course of 7 days and then oven cured for 24 hours at 58°C. After fixation and mounting, fibers were ultramicrotomed with a freshly broken glass knife to a thickness of 50 µm. A 1% toluidine blue solution was used to stain the sections for imaging. Transmission light microscopy was performed at 20x magnification on a Leica DM5500 upright microscope system. At least three cross-sections were taken per sample for image analysis.

Image analysis of transmission light micrographs was performed with ImageJ Fiji software. Measurements were taken to record the area and diameters of each technical fiber (D1 = large diameter & D2 = small diameter), the area of elementary fiber, as well as the area and diameters of each lumen visible within the cross-section (d1 = large diameter of lumen, d2 = small diameter of lumen). At least 10 measurements of each fiber attribute were taken per cross-

section. Specimens where the lumen was obscured or folded (due to sample preparation) were excluded. The percentage of cellular area containing lumen was recorded on at least three technical fiber cross-sections per sample.

3.2.2 Transmission Electron Microscopy (TEM) & EDS

A Thermo-Fisher Talos F200X G2 S/TEM (200 kV) and EDS (Super-X window-less system) were used to image and analyze the chemical composition of fiber cross-sections. Fiber cross-sections were prepared via PFIB (Pt cap applied for sectioning, 100 nm sections) or via mounting and microtoming (80 nm sections) and placed on a copper grid with 200 mesh spacing. To mount and microtome, samples were prepared as described in section 3.2.1 and manually placed on copper grids.

3.2.3 X-ray Diffraction (XRD)

A Rigaku SmartLab X-ray Diffractometer (XRD) with Cu-KR radiation (k = 0.154 nm) generated at 40 kV and 44 mA was used to characterize the crystallinity of the fibers. Fibers were held in a unidirectional single layer on a glass slide and conditioned in a desiccator held at 20% RH overnight prior to testing. The diffraction data were collected from 8 to 40° 2θ with a scan rate of 2° / min at 0.02° increments. Diffraction data from seven spots per sample were collected (unless otherwise stated). The fibers were identified as cellulose-I based on characteristic peaks for (1 -1 0) (1 1 0) and (2 0 0) located at approximately 14.5, 17, and 22° 2θ, respectively. [73–75] D-spacings were calculated using Matlab R2022a. The cellulose-I peaks were identified from XRD data using a built-in peak finding function and d-spacings were calculated using Bragg's law assuming a monoclinic structure. [76] Cellulose crystallinity was calculated using the method proposed by Segal, et al., per Equation 4, with I_{002} referencing the

intensity of the (2 0 0) cellulose peak found at approximately 22° 2θ and I_a references the intensity of the amorphous material, taken at the minima at 18.6° 2θ.[74]

$$\chi = \frac{I_{002} - I_a}{I_{002}} \quad (4)$$

3.2.4 Porosity and Specific Surface Area

Fiber microporosity and specific surface area were determined via nitrogen physisorption on a Micromeritics ASAP 2020. Fibers were manually cut into a fine powder (< 1 mm fiber length) using sharp scissors; at least 0.1 g of fiber were analyzed. Fibers were degassed at 60°C for 2 hours prior to analyses by N_2 physisorption at -196 °C (77 K). BET method using 10 data multipoint with relative pressures of 0.05-1 was applied. The pore volume was calculated based on the Barret–Joyner–Halenda (BJH) model.

3.2.5 Density

Fiber skeletal density was measured via nitrogen pycnometry on an Anton Paar Ultrapyc 5000. Flax fibers were cut to 65 mm in length and 0.5-1 g of fiber was used for volume measurements via the pycnometer. Fibers were infiltrated with nitrogen at 34.5 kPa and held at 20°C throughout testing. A total of 15 infiltration cycles were performed and average skeletal density was reported.

The bulk density of fibers was determined via measurement of the weight of 35 fibers cut to 65 mm in length using a microbalance. The volume of the fibers was determined by measurement of fiber diameters along two axes via imaging on an Olympus inverted GX51 microscope at 5x magnification followed by image analysis using the software ImageJ Fiji.

3.2.6 Attenuated Total Reflectance Fourier Transform Infrared Spectroscopy (ATR-FTIR)

ATR-FTIR analysis was conducted using a Jasco Fourier Transform Infrared Spectrometer (FT/IR 4100). Spectra were captured using 128 scans at a resolution of 0.24 cm^{-1} from 4000 to 800 cm^{-1}. Fibers were chopped into a fine powder and pressed onto the ATR crystal. A constant pressure was applied to each sample and key peaks related to lignocellulosic components were identified using OMNIC Spectra software.

3.3 Results and Discussion

3.3.1 Single Fiber Tensile Properties

The tensile properties of flax fibers before and after direct treatment in $scCO_2$ are shown in Figure 3.2. Treatments resulted in increases to tensile modulus and ultimate strength of flax fibers. Treatment at 28MPa without nanoparticles resulted in a 33% and 40% increase in tensile modulus and strength, respectively. The addition of nanoparticles resulted in further increases to tensile modulus and strength. Specifically, treatment in $scCO_2$ at 10MPa in the presence of TiO_2 resulted in 43% and 67% improvements to fiber tensile modulus and strength, respectively. Treatment in $scCO_2$ at 28MPa in the presence of TiO_2 resulted in a 71% and 80% improvement in modulus and strength, respectively.

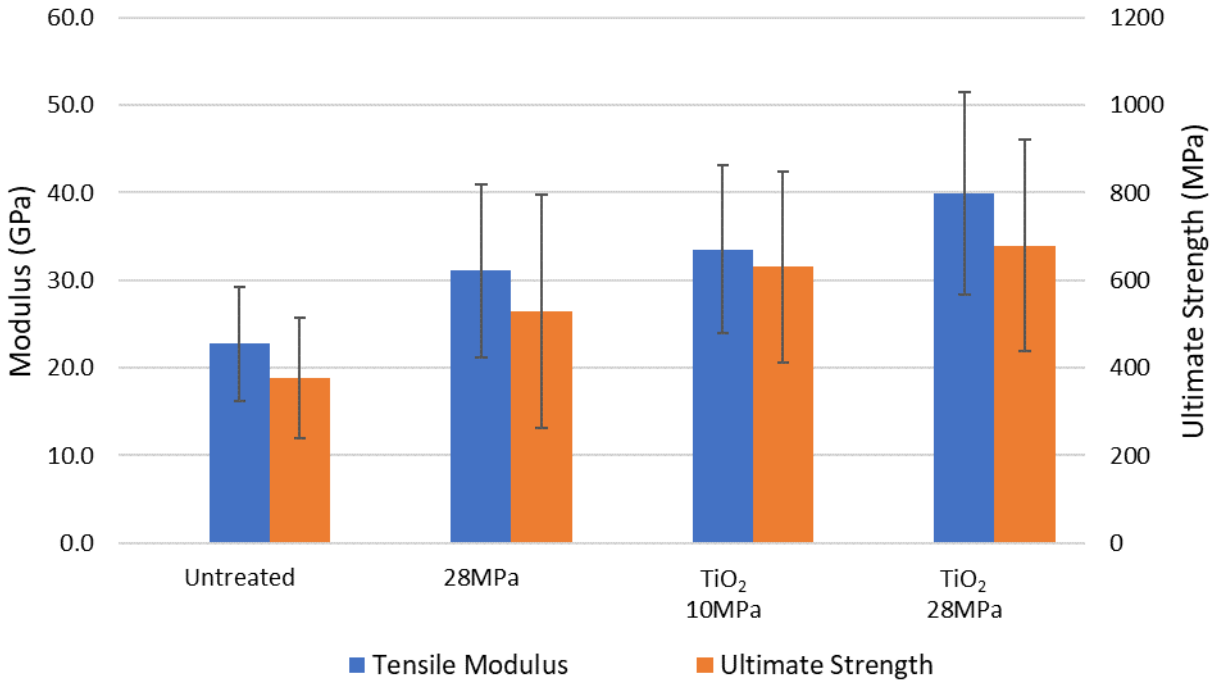

Figure 3.2: Single fiber tensile properties of flax fibers after undergoing treatment in supercritical fluid with or without the presence of TiO_2 nanoparticles.

3.3.2 SEM, TEM, and EDS

To determine whether nanoparticles were able to infiltrate and reinforce the fiber structure, fibers were analyzed by PFIB-SEM and EDS. SEM of the fiber surface revealed the presence of very few TiO_2 agglomerates located in crevices, but no overall surface coating with nanoparticles was observed (Figure 3.3). Further, no damage to the fiber surface was observed, as previously seen following aqueous pre-treatment of the fibers (Figure 2.16).

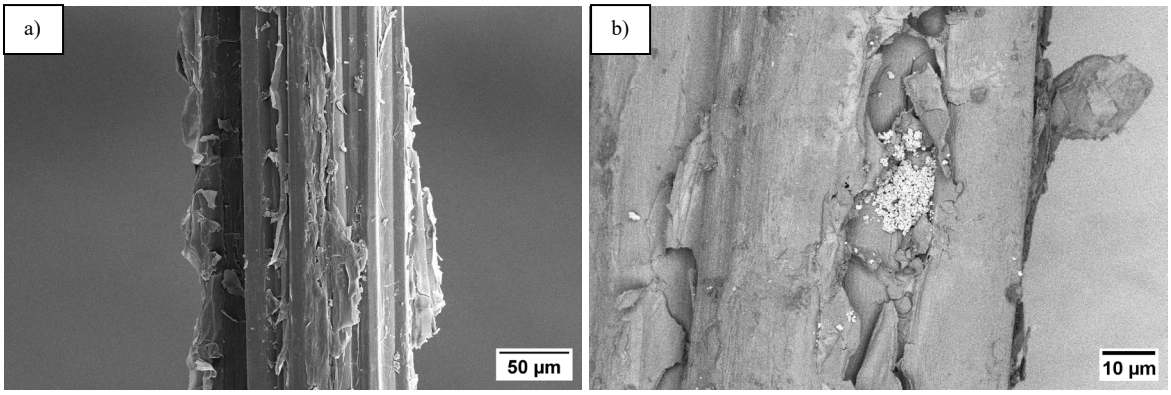

Figure 3.3: (a) Surface of TiO_2 28MPa treated fiber. (b) A few nanoparticle agglomerates were visible on the fiber surface and within surface defects.

Cross-sections of flax fibers treated in $scCO_2$ with TiO_2 at 28MPa (TiO_2 28MPa) were prepared using PFIB, and the elemental composition of the cross-section was examined using EDS. No significant Ti was detected with EDS and no Ti particles were observed visually, suggesting that if particles were present in the fiber structure, they would have to be present at relatively low concentrations and very disperse (below the detection limit of the EDS in the PFIB-SEM used for this analysis) (Figure 3.4).

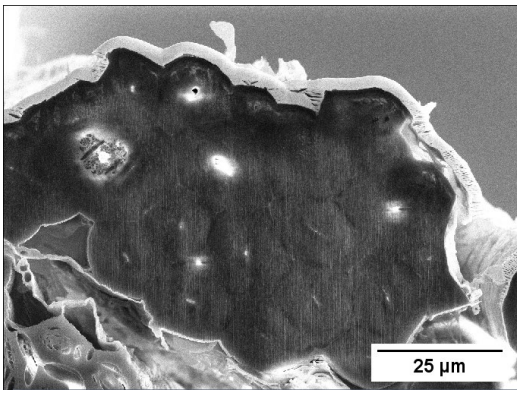

Figure 3.4: Cross-section of TiO_2 28MPa treated fiber cut and imaged with PFIB-SEM. No TiO_2 nanoparticles were detected within the cross-section of the fiber.

TEM was employed to enable higher-resolution imaging and EDS detection of Ti in fiber cross-sections. Figure 3.5 shows a cross-section of an elementary fiber coated with a platinum cap (applied for PFIB during TEM preparation) and evaluated using EDS. No significant TiO_2 was detected within the fiber cell walls or in the middle lamella. Some TiO_2 was detected beneath the surface of the fiber beneath the Pt cap. Figure 3.6 shows highly magnified areas of the surface of the fiber in which small TiO_2 agglomerates were detected. It is likely that some TiO_2 may be accumulating in small cracks or crevices on the fiber surface, which could be contributing to minor delay in crack propagation and minor improvements in performance. However, the magnitude of the improvement in performance suggests that additional mechanisms for property improvement are present.

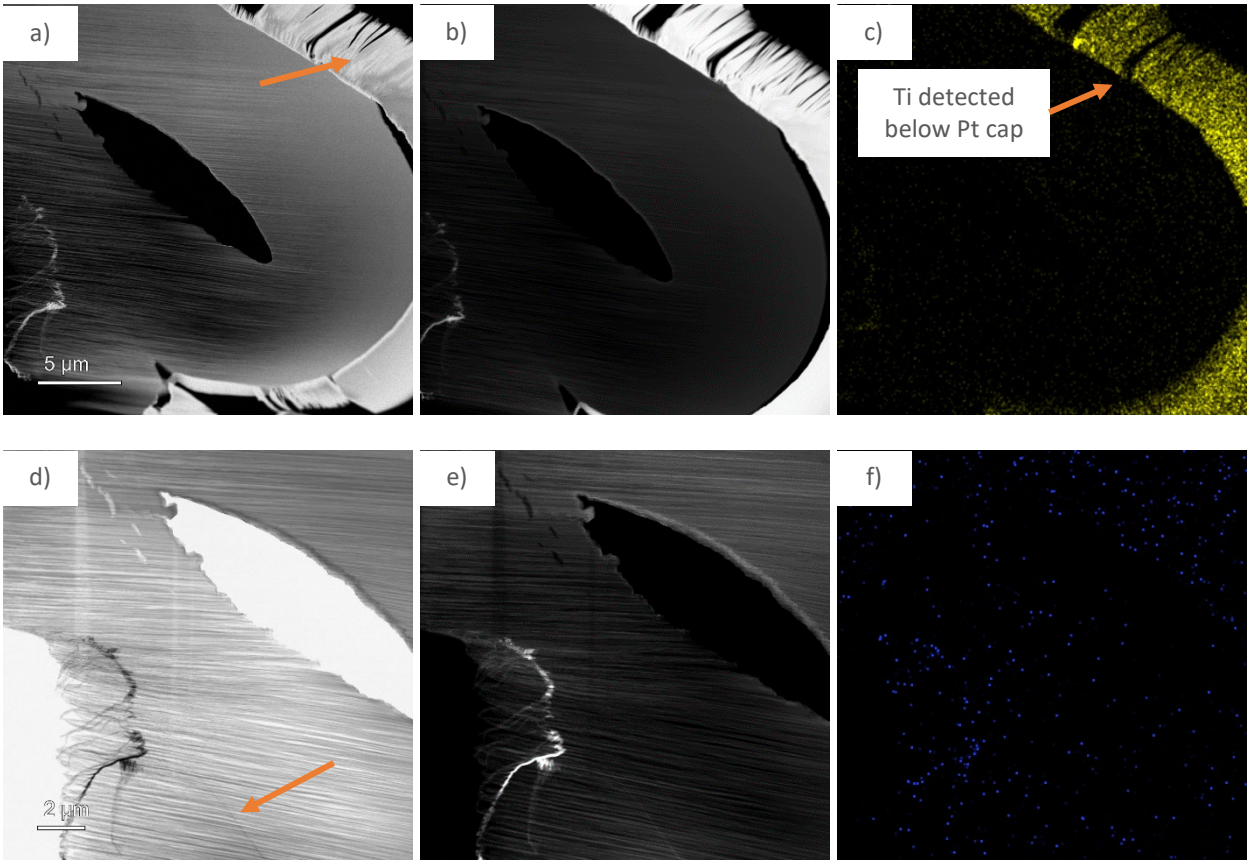

Figure 3.5: Cross-sections of TiO_2 28MPa treated fiber cut and imaged with TEM. No TiO_2 nanoparticles were detected within the elementary fiber or in the middle lamella. a) TEM micrograph with arrow indicating location of Pt cap placed on fiber surface during sample preparation for TEM. b) High-angle annular dark-field (HAADF) scanning TEM image of fiber. In HAADF, elements with higher Z appear brighter. High contrast observed on sample surface (Pt cap). c) EDS map of Ti signal indicating presence of Ti on surface of fiber beneath Pt cap. d) TEM micrograph of internal structure of sample, with arrow indicating location of middle lamella. e) HAADF TEM image of internal structure of sample; no Ti detected. f) EDS map of Ti signal; no Ti detected inside cell wall or in middle lamella.

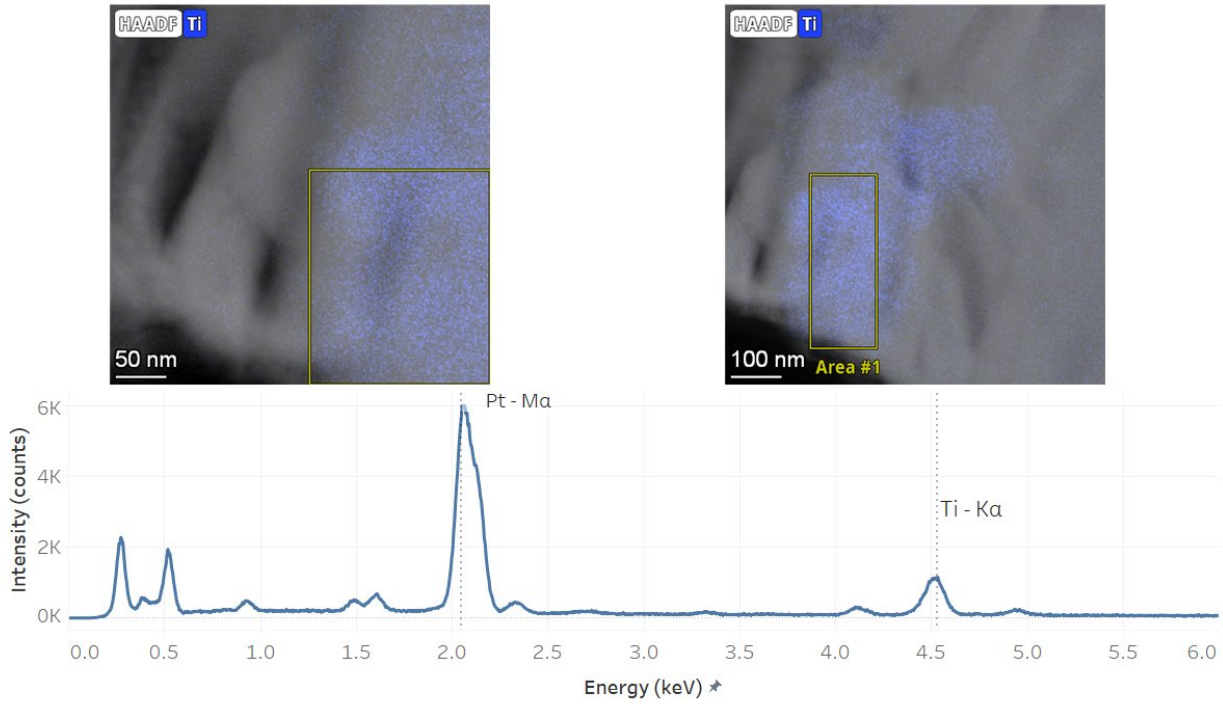

Figure 3.6: Surfaces of TiO_2 28MPa treated fibers cut with PFIB and imaged with TEM. EDS was used to map and validate the presence of Ti beneath the Pt cap. TiO_2 nanoparticles were detected sporadically on the fiber surface.

3.3.3 Changes to Fiber Morphology

To understand the mechanisms behind fiber property improvements, the dimensions and morphology of flax fibers were evaluated before and after treatment in $scCO_2$. Fibers underwent fixation, microtomy, transmission light microscopy, and image analysis as shown in Figure 3.7 - Figure 3.8. Image analysis was performed on fiber cross-sections to quantify changes to technical fiber dimensions (D1 = large diameter, D2 = small diameter), technical fiber area, elementary fiber (cellular) area, lumen area, and lumen dimensions (d1 = large diameter, d2 = small diameter) (Table 3.2).

Treatment at 28MPa without nanoparticles resulted in collapse of the lumen. It is likely that the pressure differential between the outside of the technical fiber and the internal closed

pore of the lumen encourages the observed collapse; lumen are less than 40 μm long pores and the technical fibers were treated at 6cm in length.[17,25,77] The lumen consisted of approximately 3.1% of cellular cross-sectional area before 28 MPa treatment, but only 1.2% of cellular cross-sectional area after treatment, a 63% reduction in lumen area (Table 3.2). The lumen size before treatment is consistent with previously reported values; Charlet, et al. reported that lumen consisted of approximately 2.7-4.0% of cellular area.[22] Additionally, the smaller diameter of the lumen (d2) was reduced by approximately 43% while the larger lumen diameter (d1) was reduced by ~24% (Table 3.2). The natural elliptical shape of the lumen likely predisposes the small diameter to close under compression. Additionally, the average lumen area after treatment at 28MPa without nanoparticles was reduced by ~7 μm^2 while the average elementary fiber area was reduced by 23 μm^2. It is possible that the additional reduction in elementary fiber areas is due to reductions in cellular micro/meso porosity or due to molecular consolidation.

Fibers treated with TiO_2 at 28MPa exhibited similar reductions to lumen area and diameters as treatment at 28MPa (without nanoparticles) (Table 3.2). However, the technical fiber area after treatment with TiO_2 was reduced by 66%, compared to an 8.6% change in elementary fiber area after 28 MPa treatment (without nanoparticles) (Table 3.2, Figure 3.9). This suggests that technical fibers are being fibrillated, or split into smaller technical fibers, upon TiO_2 28MPa treatment. The significant reduction in technical fiber cross-sectional area could be contributing to the improvement in fiber mechanical properties, as prior work has shown that smaller cross-sectional area fibers exhibit higher strength and moduli than larger technical fibers, due to the presence of fewer weak middle lamellae throughout the fiber cross-section. [20,24,28]

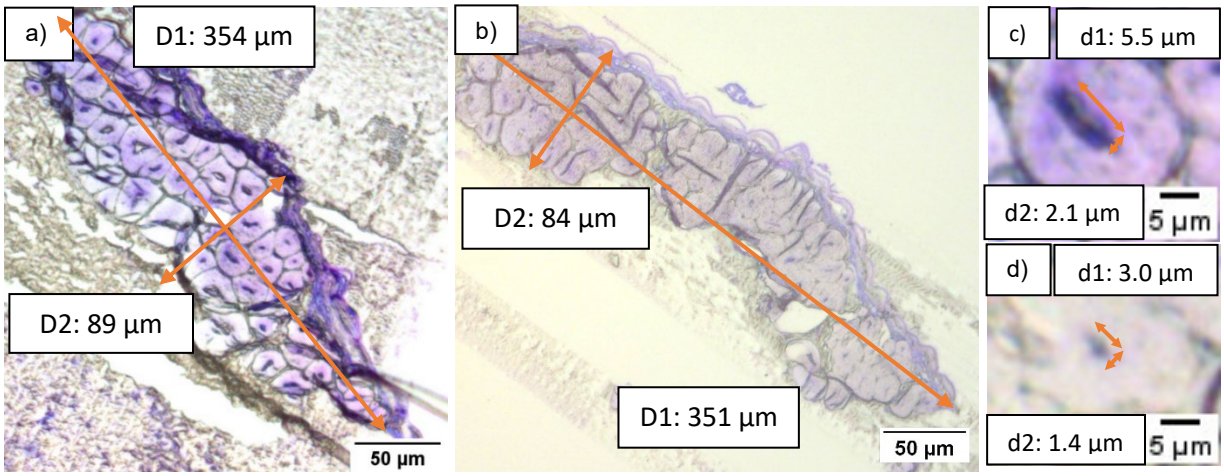

Figure 3.7: Flax fiber cellular morphology shown via fiber fixation and microtoming. a) Untreated fiber labeled with fiber diameters D1 and D2, b) 28MPa treated fiber, c) Untreated fiber lumen, labeled with lumen diameters d1 and d2, d) 28MPa treated fiber lumen. 28MPa treatment (without nanoparticles) appears to result in collapse of lumen, reducing fiber porosity.[78]

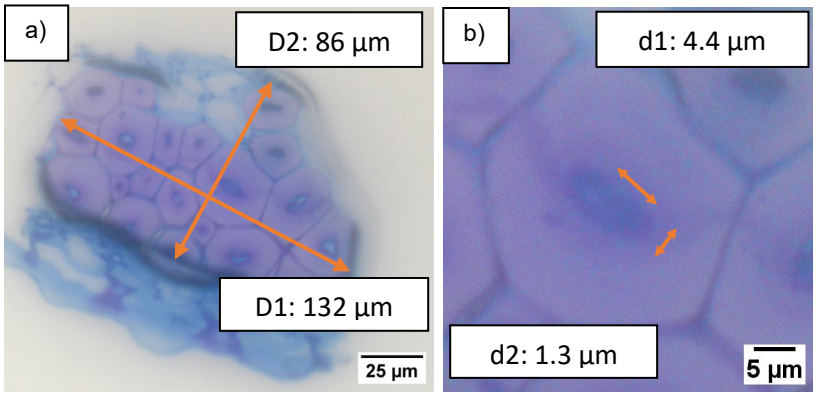

Figure 3.8: TiO_2 28MPa treated flax fiber cross-section, showing morphology of a) technical fiber, labeled with diameters D1 and D2, b) lumen, labeled with lumen diameters d1 and d2.

Table 3.2: Summary of changes to fiber morphology upon 28MPa treatment as well as TiO_2 28MPa treatment.

	Untreated	28MPa	TiO_2 28MPa	Δ due to 28MPa treatment	Δ due to TiO_2 28MPa treatment
Technical Fiber Area [µm^2]	25250 ± 2085	23258 ± 1865	8639 ± 720	-7.9%	-66%
Elementary Fiber (cellular) Area [µm^2]	314.9 ± 106	292.2 ± 102	287.9 ± 180	-7.2%	-8.6%
Lumen Area [µm^2]	10.50 ± 10.8	3.91 ± 4.2	3.82 ± 3.5	-63%	-64%
Lumen diameter – d1 [µm]	5.90 ± 1.3	4.47 ± 1.4	4.25 ± 1.8	-24%	-28%
Lumen diameter – d2 [µm]	2.30 ± 0.6	1.32 ± 0.5	1.59 ± 0.6	-43%	-31%

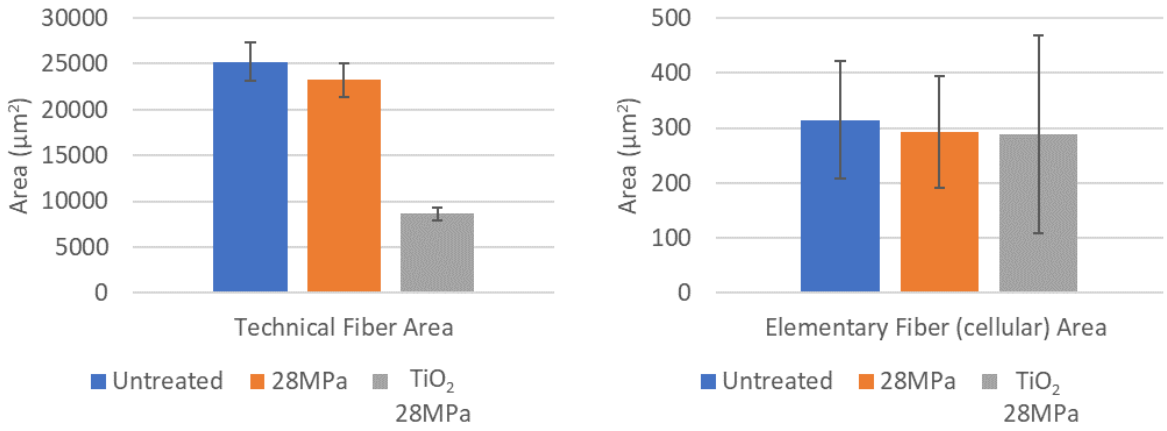

Figure 3.9: Area of technical fibers and elementary fibers before and after 28MPa treatment and TiO_2 28MPa treatment.

Prior work has shown that the inclusion of the lumen in cross-sectional area measurements for fiber tensile testing can contribute to overestimation of the load bearing component of the fiber.[79,80] When the lumen-included area is used in the calculation of fiber stress during single fiber tensile testing, the resulting moduli and ultimate strength values are lower than the inherent material property. The untreated fiber cross-sectional areas were

corrected to remove the 3.1% porosity, representing the lumen's contribution to cross-sectional area (Figure 3.10). Treatment of fibers at 28MPa without nanoparticles improved the fiber modulus and ultimate tensile strength by 33% and 36%, respectively, after lumen correction for cross-sectional area.

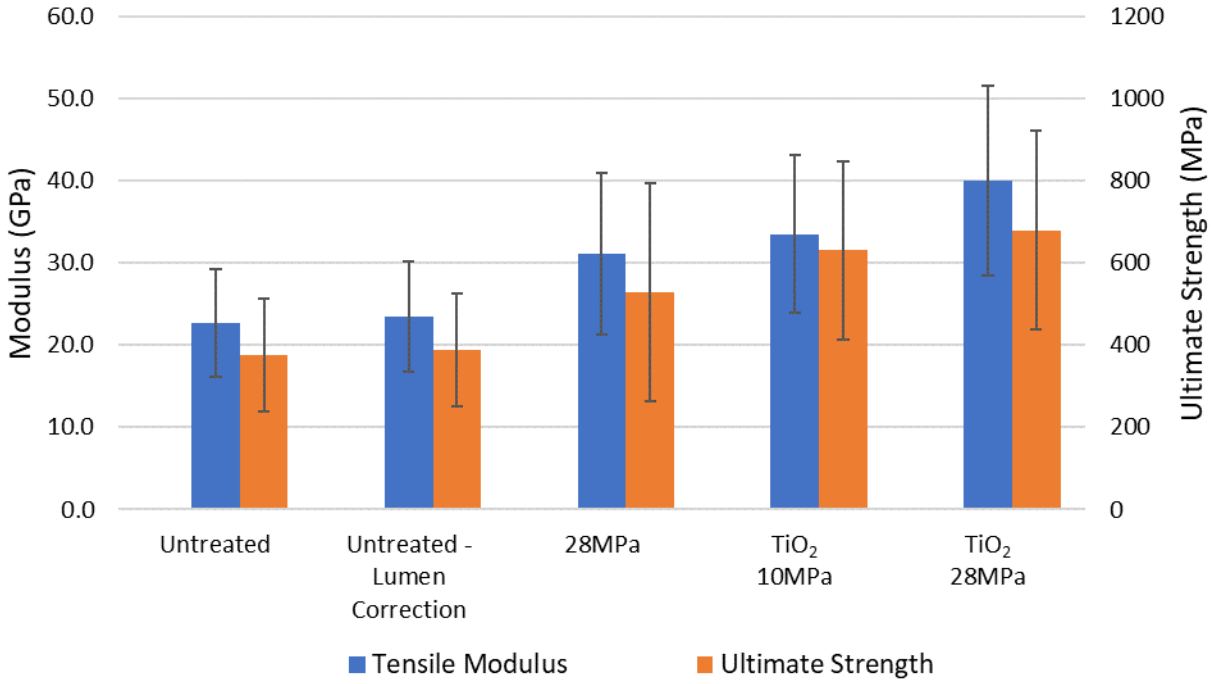

Figure 3.10: Single fiber tensile properties of untreated flax fibers before and after correction for lumen porosity.

3.3.4 Changes to Fiber Structure

After 28MPa and TiO_2 28MPa treatments, lumen cross-sectional area was reduced by ~7 μm^2 (63%) while the cellular cross-sectional area was reduced by ~23 μm^2 (7.2%). This suggests that the treatment is not only causing collapse of the lumens in each technical fiber, but also contributing to consolidation of micro/meso porosity and/or free volume within the fibers. To evaluate the effects of treatment on porosity, the micro/meso porosity and surface area of the

fibers were evaluated via nitrogen physisorption. Because this technique required evaluation of fibers cut to very small lengths (<1mm), lumen were exposed during physisorption, allowing for internal micropores and mesopores to be analyzed. However, the lumen itself is larger than the upper limit of the technique and was not measured via physisorption.

The pore volume and surface area results are shown in Table 3.3 and Figure 3.11 - Figure 3.13. 28MPa treatment results in a ~24% reduction in total micro/meso pore volume and a ~19% reduction in fiber surface area. Additionally, the pores most affected by 28MPa treatment have widths between 40-100 Å, which suggests that treatment has a more significant effect on very small pores, in comparison to pores which are sized near the upper limits of the technique (~4000 Å). This is consistent with the changes to surface area observed, which saw maximum reductions to pores with widths <100 Å (Figure 3.13).

TiO_2 28MPa treatment resulted in 93% and 98% reductions of total pore volume and surface area, relative to untreated fibers. Additionally, pores smaller than 93Å were no longer detected after treatment with TiO_2. This significant decrease in porosity and surface area suggests the possibility that the nanoparticles are highly mobile during treatment and repeatedly impacting the fiber surface resulting in compression of the fibers, pore closure, and surface smoothing.

Table 3.3: Micro/meso porosity and specific surface area of fibers before and after 28MPa treatment and TiO_2 28MPa treatment.

	Sample Mass (cm^3/g)	Total Volume in Pores (cm^3/g)	Total Surface Area in Pores (m^2/g)
Untreated	0.109	0.01901	4.888
28MPa	0.115	0.01445	3.607
TiO_2 28MPa	0.152	0.00131	0.090

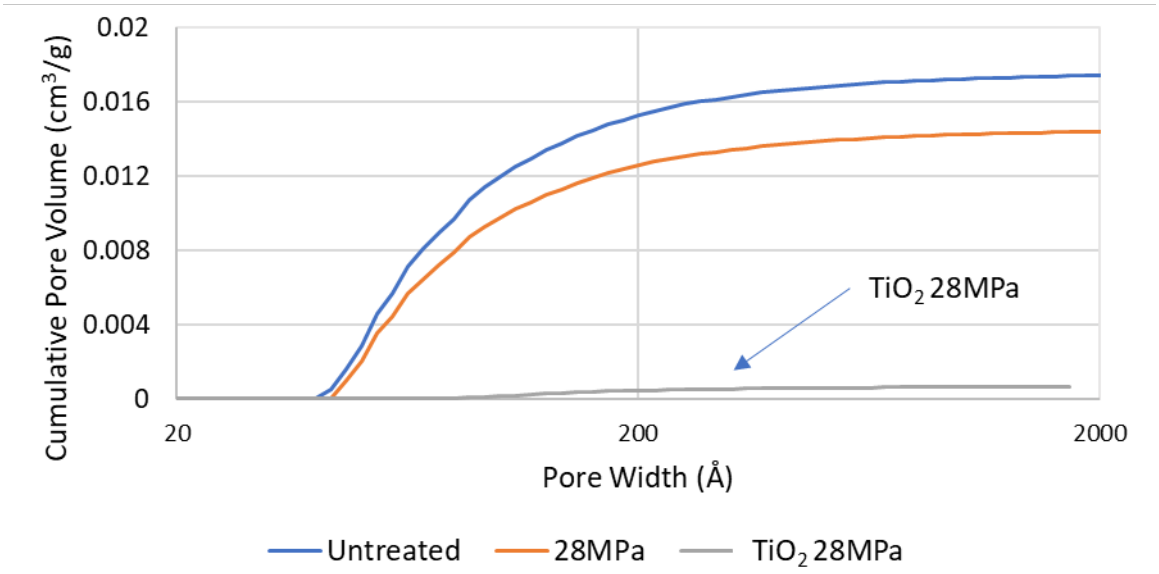

Figure 3.11: Cumulative pore volume of fibers before and after 28MPa treatment and TiO_2 28MPa treatment.

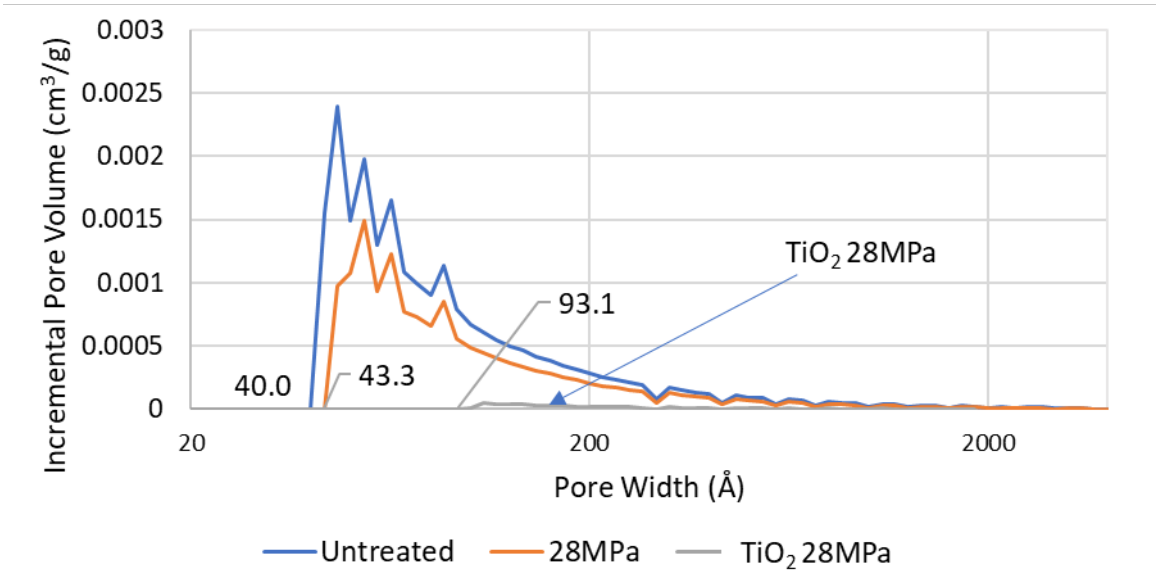

Figure 3.12: Incremental pore volume of fibers before and after 28MPa treatment and TiO_2 28MPa treatment.

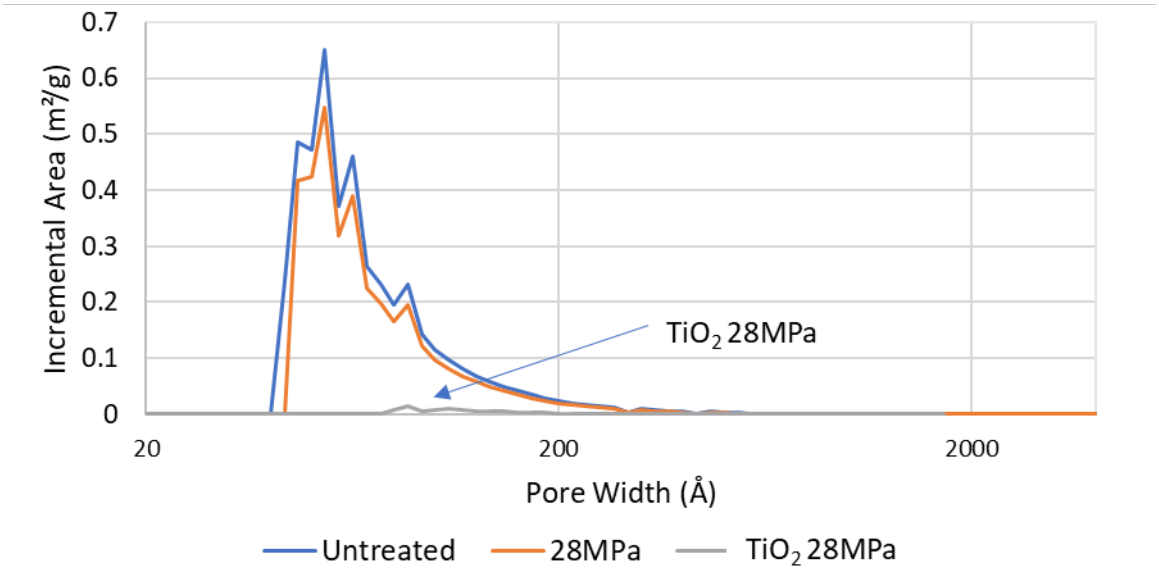

Figure 3.13: Incremental specific surface area of fibers before and after 28MPa treatment and TiO_2 28MPa treatment.

Using measurements of lumen size and pore volume from gas physisorption, total fiber porosity can be calculated and changes to porosity with treatment can be quantified. Macro porosity was determined as the percentage area of each elementary fiber consisting of lumen.

The bulk density of all fibers was measured to be ~0.79 g/cm^3. Using the bulk density and pore volume measurements from gas physisorption, the contribution to total fiber porosity from micro/meso pores can be calculated using Equation 5.

After 28MPa treatment, macro porosity (the lumen) is reduced by ~63% upon treatment and micro/meso porosity was reduced by ~27%. Overall, flax technical fiber porosity was reduced by ~50% due to 28MPa treatment (Table 3.4). TiO_2 28MPa treated fibers showed a similar change in macro porosity as 28MPa treatment. However, micro/meso porosity reduced by 43% in comparison to 28MPa treated fibers. TiO_2 28MPa treatment resulted in a 70% reduction in total technical fiber porosity (Table 3.4), suggesting that the presence of nanomaterials during treatment has a greater effect on modifications to micro/meso scale fiber structure than macro-scale structural changes.

Skeletal density was measured using gas (nitrogen) pycnometry (Table 3.4). After 28MPa and TiO_2 28MPa treatments, fiber skeletal density increased from 1.37 g/cm^3 to 1.44 g/cm^3, consistent with reductions in porosity observed.

$$\phi = \frac{V_p}{V_T} = \frac{V_{po}+V_{pc}}{V_f+V_{po}+V_{pc}} = \frac{\frac{V_{po}+V_{pc}}{m}}{\frac{V_f+V_{po}+V_{pc}}{m}} = \frac{V_{po}+V_{pc}}{m} * \rho_T \quad (5)$$

$\phi = porosity, V_p = pore\ volume, V_T = total\ (bulk)\ volume, V_{po} = open\ pore\ volume, V_{pc} = closed\ pore\ volume, V_f = fiber\ volume, m = sample\ mass, \rho_T = bulk\ density$

Table 3.4: Summary of fiber porosity and skeletal density before and after 28MPa treatment and TiO_2 28MPa treatment.

	Macro porosity[a] (%)	Micro/Meso porosity[b] (%)	Total Porosity (%)	Skeletal Density (g/cm^3)
Untreated	3.1	1.5	4.6	1.371 ± 0.027
28MPa	1.3	1.1	2.3	1.442 ± 0.014
$TiO_2$28MPa	1.3	0.1	1.4	1.441 ± 0.022

[a] Macro porosity determined via measurement of lumen size as % of cellular area
[b] Micro/meso porosity determined via measurement of pore volume from gas physisorption measurements and bulk density measurements

Because there were significant changes to porosity of the samples upon treatment, the crystallinity of the fibers was also investigated before and after treatments to better understand how treatment may be affecting polymeric free volume (Table 3.5). The d-spacing was consistent with prior results, and no significant changes to d-spacing were observed with treatment, suggesting that the observed changes to crystallinity relate to changes to size or quantity of crystals within the fiber as opposed to modification of the crystal structure during treatment. [73] Fiber crystallinity did not significantly change after 28MPa treatment (Table 3.5, Figure 3.14). However, TiO_2 10MPa treatment resulted in a 4% increase in crystallinity and TiO_2 28MPa treatment resulted in an 11% increase in average crystallinity.

Two possible mechanisms for higher crystallinity of the fibers with treatments that include TiO_2 nanoparticles include a) molecular rearrangement due to high pressure and/or fluid presence in cell walls of the fiber or b) removal of non-crystalline materials from the fiber. Due to movement of material within the pressure vessel during treatment, it is not possible to reliably measure changes to sample weight after treatment. However, prior work has investigated the effects of increasing packing density of cellulose via high pressure compression. Vaca-Medina, et. al. found that compression of α-cellulose at room temperature in a hydraulic press at 177 MPa for short durations (10 min), resulted in increases in crystallinity and reductions in surface area.

Other published works have shown that polymers can be induced to crystallize while exposed to high pressure CO_2. Tomasko, et al, found that cellulose crystallization which is dominated by growth of existing crystals (as opposed to nucleation) is accelerated and the temperature at which the maximum rate of crystallization occurs is depressed. [64] The authors attributed the increases in crystallinity to the reorganization of the amorphous cellulose into crystalline cellulose. [81] Additional characterization of α-cellulose via the creation of isobar (PVT) curves found that at pressures above 20 MPa and temperatures above 40°C for 30 min, the specific volume of α-cellulose decreases and density increases. [82] It is possible that the repeated impact of TiO_2 nanoparticles on the fiber surface is shot peening the fiber, causing consolidation and crystallization of amorphous cellulose during treatment.

Table 3.5: Crystallinity index and d-spacing for fibers before and after supercritical fluid treatments.

		d-spacing (Å)		
	Segal Crystallinity Index (%)	**(1 -1 0)**	**(1 1 0)**	**(2 0 0)**
Untreated	70 ± 7	5.98	5.32	3.92
28MPa	71 ± 3	5.92	5.34	3.92
TiO_2 10MPa	73 ± 5	5.94	5.37	3.92
TiO_2 28MPa	81 ± 2	5.98	5.36	3.92

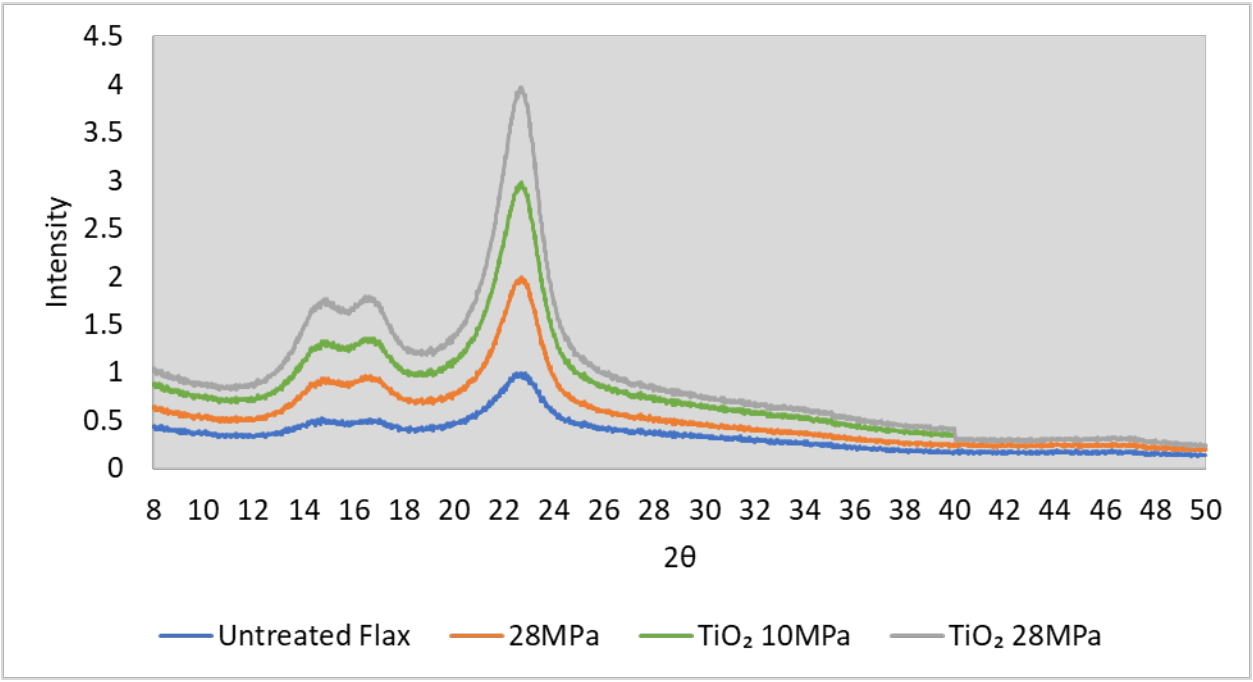

Figure 3.14: XRD spectra for untreated, 28MPa, TiO_2 10MPa, and TiO_2 28MPa treated flax fibers.

3.3.5 Changes to Fiber Chemistry

To evaluate if non-crystalline material was removed from the fibers, ATR-FTIR was used to evaluate whether bulk changes in fiber chemistry occurred during treatment with $scCO_2$ (Figure 3.14). Table 3.6 identifies key structures associated with the visible peaks and relates them to known lignocellulosic components, as previously identified in the literature. No significant changes in composition and no selective removal of major lignocellulosic components were observed after treatment in $scCO_2$.

Prior work exploring the use of $scCO_2$ as a treatment for natural fibers has shown varying results with respect to chemical extraction of lignocellulosic components. For example, Li, et al., found that treatment in $scCO_2$ alone did not result in any dissolution or change in physical form or color of α-cellulose, kraft lignin, arabinogalactan or xylan (hemicellulose), xylose,

glucose, or chemical components of a variety of wood species.[55] However, Seghini, et al. found that treatment of flax fibers in $scCO_2$ can result in the removal of lignin and hemicellulose.[42] In comparison to prior work which has observed significant chemical removal from lignocellulosic biomass, this study used much slower pressurization and depressurization rates. It is possible that the slower rates used in this work resulted in less or no chemical extraction.

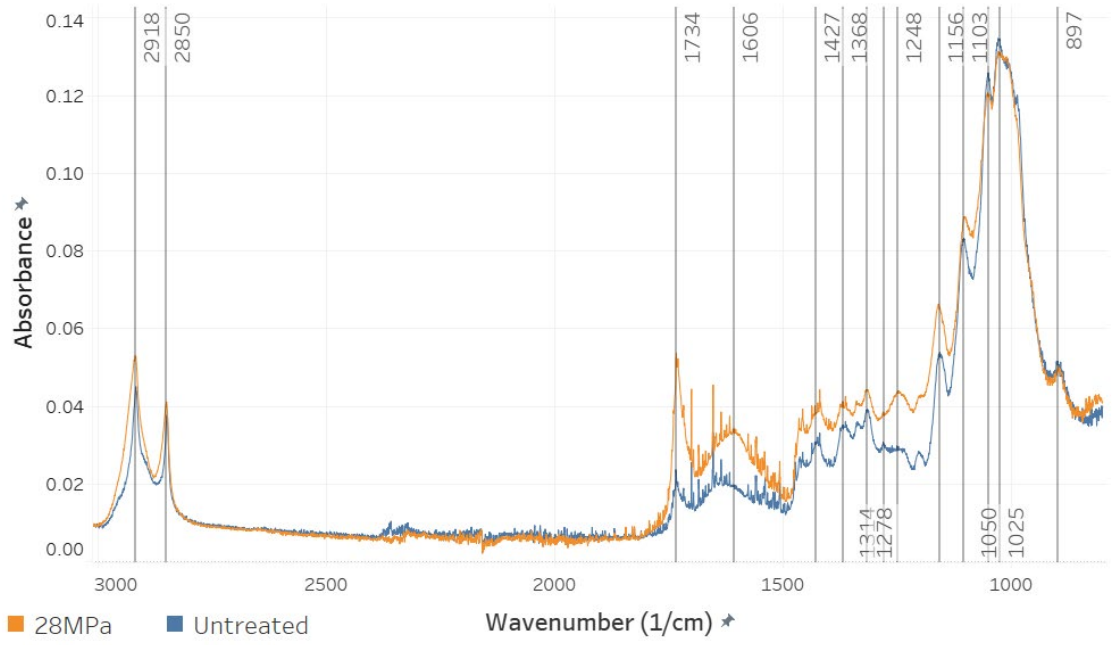

Figure 3.15: FTIR spectra for untreated and 28MPa treated fibers, showing no significant changes to fiber composition upon treatment.

Table 3.6: FTIR peak assignments related to the lignocellulosic components within the flax fiber, as previously published in the literature.[42,83]

Structure	Wavenumber	Assignment
C-H	2918	cellulose & hemicellulose
C-H	2850	cellulose & hemicellulose
C=O	1734	hemicellulose
HOH	1637	water in crystalline cellulose
C=O	1606	hemicellulose
CH_2	1427	cellulose
CH	1368	polysaccharides
CH_2 & CH	1314	cellulose & hemicellulose
CH_2	1278	cellulose
C-O-C & C-C	1248	hemicellulose
C-O-C	1156	polysaccharides
C-O-C & C-C	1103	polysaccharides
C-OH	1050	cellulose & hemicellulose
C-O & O-H	1025	cellulose
C-H	897	monosaccharides

3.3.6 Possible Mechanisms for Fiber Modification

In this chapter, treatment of flax fibers directly in $scCO_2$ with 5nm TiO_2 nanoparticles (TiO_2 28MPa) resulted in the reduction of technical fiber cross-sectional area, reduction in porosity, an increase in fiber crystallinity, an increase in fiber modulus and strength, and no measured changes to fiber chemistry. It was hypothesized that there may be one of two mechanisms occurring during fiber treatment (or a combination therein). Figure 3.15 shows one possible mechanism for the improvements observed: fiber fibrillation. It is possible that the nanoparticles are repeatedly impacting the fiber surface during treatment, causing highly porous, low modulus components of the technical fiber to break off, leaving behind a smaller technical fiber consisting of elementary fibers with low porosity, high crystallinity, and higher mechanical properties. Figure 3.16 illustrates another mechanism which may be occurring: shot peening. Shot peening of metals is a well understood cold-working technique which locally compresses a metal's surface, changing grain structure and improving fatigue resistance. It has also been applied to a variety of polymeric materials, in an attempt to control the crystallinity and polymer microstructure by manipulating chain alignment. [84–87] It is possible that a similar mechanism of polymer modification is occurring during these treatments. During treatment, highly mobile nanoparticles could be repeatedly impacting the fiber surface, inducing local compressive stress. The compression could be causing fiber surface smoothing and pore closure (observed in Table 3.3) while encouraging molecular re-arrangement and the formation of additional cellulose nanocrystals within elementary fibers. It is also possible that a combination of these mechanisms is occurring during treatment. Future work suggests exploring these mechanisms further to better understand how treatment could be optimized for both efficacy and cost.

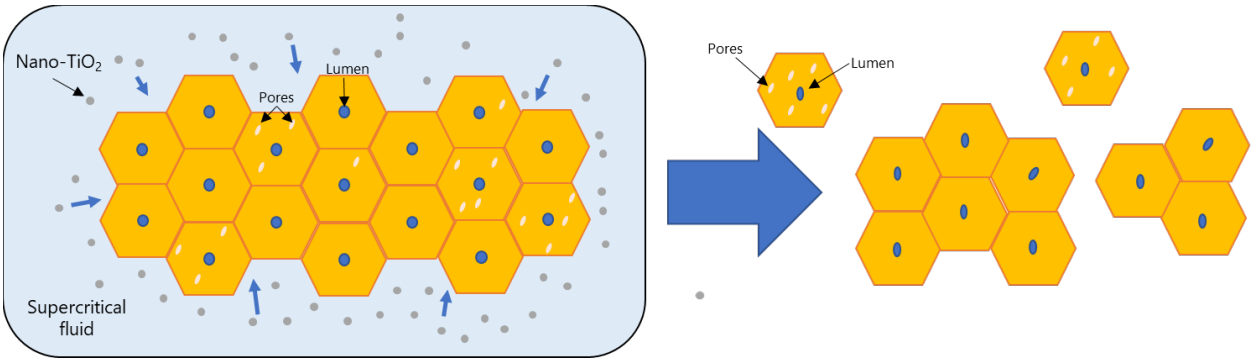

Figure 3.16: Schematic illustrating possible mechanism for flax fiber modification, involving fiber fibrillation. In this mechanism, nanoparticles could be impacting the fiber surface, resulting in fibrillation of the technical fiber, leaving behind smaller technical fibers with reduced porosity, higher crystallinity, and improved mechanical properties.

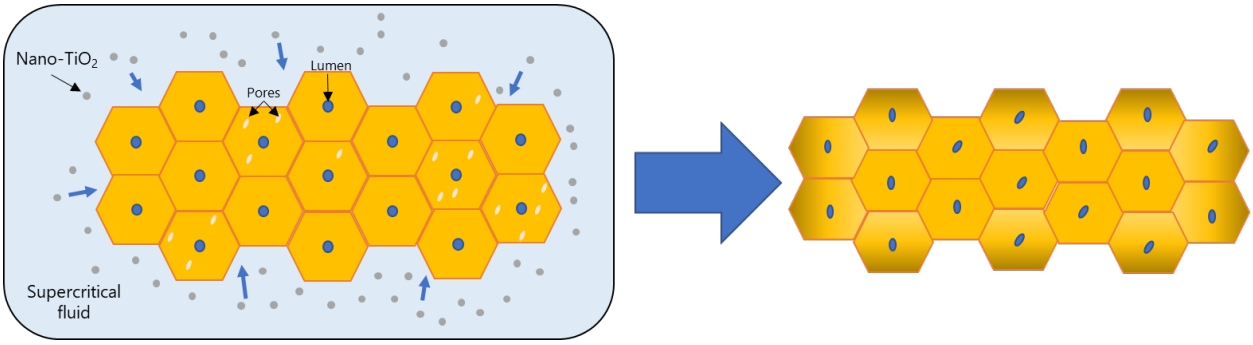

Figure 3.17: Schematic illustrating possible mechanism for flax fiber modification, involving shot peening of the fiber. In this mechanism, nanoparticles could be impacting the fiber surface, inducing local compressive stresses and plastically deforming the fiber surface. The result is a technical fiber with low surface roughness, reduced porosity, higher crystallinity, and improved tensile properties.

3.4 Conclusions

Treatment of flax fibers directly in $scCO_2$ with nanomaterials was explored. Fibers were treated in $scCO_2$ at 28MPa with and without 5nm TiO_2 nanoparticles (TiO_2 28MPa, 28MPa treated fibers, respectively) as well as at 10MPa with 5nm TiO_2 nanoparticles (TiO_2 10MPa treated fibers). A summary of changes to fiber structure, morphology, and mechanical properties is shown in Table 3.7.

Table 3.7: Summary of changes to fiber mechanical properties, morphology, and structure with direct treatment in $scCO_2$ with and without TiO_2 nanoparticles at 28MPa.

Change with treatment, compared to untreated flax		
	28MPa	**TiO_2 28MPa**
Modulus	↑ 33%	↑ 71%
Ultimate Strength	↑ 40%	↑ 80%
Skeletal Density	↑ 5%	↑ 5%
Macroporosity (Lumen Area)	↓ 63%	↓ 64%
Micro/meso porosity	↓ 27%	↓ 93%
Crystallinity	↑ 1%	↑ 11%

Treatment in $scCO_2$ at 28MPa (28MPa) resulted in 33% and 40% increases to fiber modulus and strength, respectively. Treatment caused the lumen in elementary fibers to collapse, resulted in a 50% reduction in total porosity, and increased fiber density by 5%. Fiber crystallinity was not significantly affected by 28MPa treatment; a 1% increase in average fiber crystallinity was observed. ATR-FTIR was used to evaluate the bulk chemistry of the fibers after 28MPa treatment. No significant changes to composition nor selective removal of lignocellulosic components were observed.

Treatment in $scCO_2$ at 28MPa with TiO_2 (TiO_2 28MPa) resulted in a 71% and 80% increase in fiber modulus and strength, respectively, but did not result in the incorporation of nanoparticles within the fiber structure, as determined via PFIB-SEM, TEM, and EDS. TiO_2 28MPa treatment resulted in a reduction to fiber cross-sectional area, suggesting that treatment results in fibrillation of the technical fibers. Treatment also resulted in lumen collapse, but reduced micro/meso porosity to a greater extent than treatment without nanoparticles. TiO_2 28MPa treatment resulted in a 70% reduction in total porosity and a 98% reduction in fiber surface area, suggesting that TiO_2 nanoparticles could be inducing pore closure and smoothing of the fiber surface. Additionally, TiO_2 28MPa treated fibers exhibited an 11% increase in fiber crystallinity, compared to untreated fibers. It is possible that fibers are being shot peened by

nano-TiO_2 particles, resulting in polymer chain consolidation and the formation of new cellulose crystals in the fiber structure.

Chapter 4 reports subsequent work where composite materials were fabricated with treated flax fibers and evaluated to determine if the improvements to fiber properties would translate into increased composite mechanical properties.

Chapter 4 Improved Flax Fiber Polymer Composite Performance

4.1 Introduction

Prior work has explored the use of flax as a reinforcement for polymer composites.[15,20,92,21,23,24,32,88–91] Like many polymer composites, natural fiber composite micromechanics are most commonly modeled via the Cox shear lag model, in which load is transferred from the matrix to a reinforcement via shear stress at the fiber-matrix interface.[11,93–95] Because of the importance of the interface in composite properties, many studies have explored chemical or physical treatments for flax fibers to improve interfacial adhesion with polymer matrices. Alkali treatment of flax has been shown to be effective at improving the tensile strength of flax/epoxy composites when treatments occur at low concentration for short durations. Specifically, 5 wt% NaOH treatment for 30 minutes has been shown to improve final composite tensile properties by 20-30% [15,32] Additionally, chemical modification via reaction of fiber surface hydroxyl groups with chemicals such as methacrylic anhydride or propionic anhydride has been shown to lead to co-polymerization between the unsaturated bonds in epoxy matrices and the vinylic groups on flax fibers during composite curing.[92]

Additionally, the Voigt model for elastic modulus, commonly referred to as the rule-of-mixtures, is generally used to predict the upper bound for composite elastic moduli, including the moduli of natural fiber composites (Equation 7). [93,96–99] However, many studies have previously reported that the rule-of-mixtures does not always accurately predict the performance of natural fiber composites. Several authors reported that single fiber tensile properties,

determined experimentally, did not match predicted fiber properties back-calculated from experimentally determined composite properties and the rule-of-mixtures.[22,93,94,97] Additionally, prior work has shown a very strong dependency between fiber size and tensile strength and modulus, with smaller fibers containing fewer middle lamellae throughout their cross-section.[10,28,100,101] While several potential sources for the discrepancy between back-calculated and experimentally calculated fiber modulus values have been previously explored, to the author's knowledge, no work has been performed to take into account the effect of fiber size in a model for composite modulus.

$$E_c = E_f V_f + E_m V_m \quad (7)$$

E_c= composite modulus. E_f = modulus of fiber. V_f= volume fraction of fiber. E_m= modulus of polymer matrix. V_m= volume fraction of polymer matrix

In Chapter 3, flax technical fibers were treated directly in $scCO_2$ in the presence of nanoparticles. 28MPa treatment (without nanoparticles) was shown to increase fiber modulus and strength by 33% and 40% respectively, while reducing fiber porosity and surface area by 50% and 20%, respectively. TiO_2 28MPa treatment resulted in a 71% and 80% increase in fiber modulus and strength, respectively. Additionally, TiO_2 28MPa treatment reduced fiber porosity by 70% and reduced surface area by 98%.

In this chapter, 30 vol% unidirectional flax-epoxy composites were fabricated via vacuum assisted molding. Composites were analyzed to understand how treatment of fibers affected composite tensile performance, tensile failure, and interfacial shear strength with the epoxy matrix. Additionally, a modification to the rule-of-mixtures was explored to consider fiber size as a non-negligible factor affecting the prediction of composite modulus.

4.2 Experimental

Flax fibers and TiO_2 nanoparticles used for this work were as described in Chapter 2, Section 2.2.1. Epon 862 resin and Epikure 3230 curing agent were used as the epoxy matrix for composite fabrication at a weight ratio of 100:35 and cured at 80°C for 8 hours. Buehler Release Agent (20-8186-004) was used as mold release.

4.2.1 Composite Fabrication

30 vol% unidirectional flax composites were fabricated using a silicone mold with 8 rectangular cavities (cavity dimensions: 3.8mm x 2.4mm x 65mm) (Figure 4.1). Epon 862 and Epikure 3230 were degassed in a vacuum oven for at least 30 min. Fiber tows were cut to 65 mm in length. Skeletal density was used to calculate the weight of fiber required to create 30 vol% composites; 8 fiber tows were created per sample (Table 4.1). Fiber tows were vacuum infiltrated with degassed resin in a vacuum oven for at least 1 hour. After infiltration, the silicone mold was coated with mold release and tows were transferred to each cavity in the silicone mold. Each cavity was filled with additional epoxy and degassed for at least 2 hours to ensure full infiltration of resin and removal of porosity. After degassing, the silicone mold was transferred to a vacuum setup as shown in Figure 4.2 and cured under vacuum at 80°C for 8 hours.

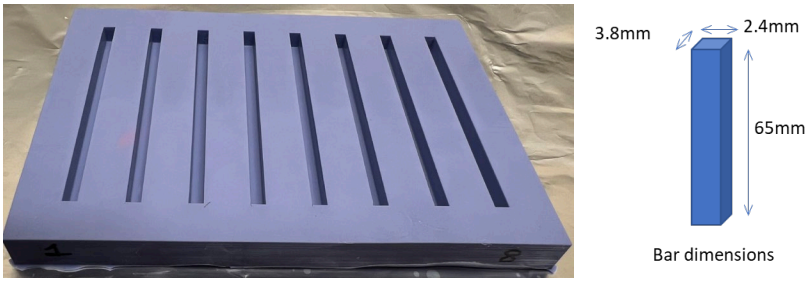

Figure 4.1: Silicone mold containing 8 rectangular cavities for composite creation. Dimensions for final composite specimens shown.

Table 4.1: Details of fiber bundles used for composite fabrication including average weight of bundles used to fill each mold cavity and final fiber volume percent. Treatment details for the types of fibers can be found in Table 3.1.

Fiber Type	Average Fiber Weight (g)	Fiber Skeletal Density (g/cm^3)	Average Fiber Volume (cm^3)	Fiber Vol%	
Untreated	0.236	1.371	0.172	29%	± 0.3%
28MPa	0.252	1.442	0.175	30%	± 0.2%
TiO_2 28MPa	0.257	1.441	0.178	30%	± 0.2%

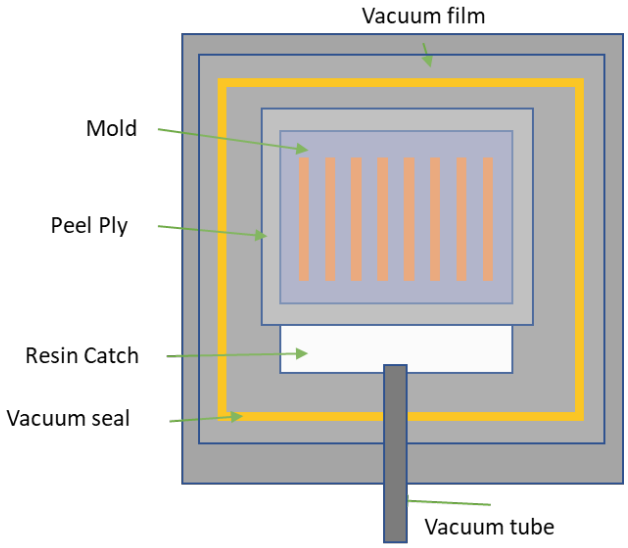

Figure 4.2: Vacuum setup used during composite curing. Samples were cured under vacuum for 8 hours at 80°C

After curing, specimens were removed from the silicone mold, placed into an aluminum fixture with 3.8mm cavities (for width control) and 2.4mm cavities (for thickness control) and polished using P600 silicone carbide sandpaper to achieve uniform width and thickness. After polishing, tabs were applied to specimens per ASTM D3039. Garolite G10 sheet was end milled to achieve a 15° bevel and cut into ~4mm tabs using a band saw. 3M DP420 adhesive was applied to the back of each tab and 250 µm glass beads were added to the adhesive to ensure uniform adhesive thickness. Four tabs were applied to each composite specimen and the

specimen was placed in a fixture for curing over 12 hours, as shown in Figure 4.3. A 1 kg weight was applied to all specimens during adhesive curing.

After adhesive curing, specimens were removed from the tab fixture and conditioned at 20% RH for 24 hours. Specimens underwent tensile testing per ASTM D3039 on an MTS Insight Tensile Machine with a 10 kN load cell. Specimens were tested with a gauge length of 35 mm at a rate of 1 mm/min using a 5mm clip-on extensometer to measure strain.

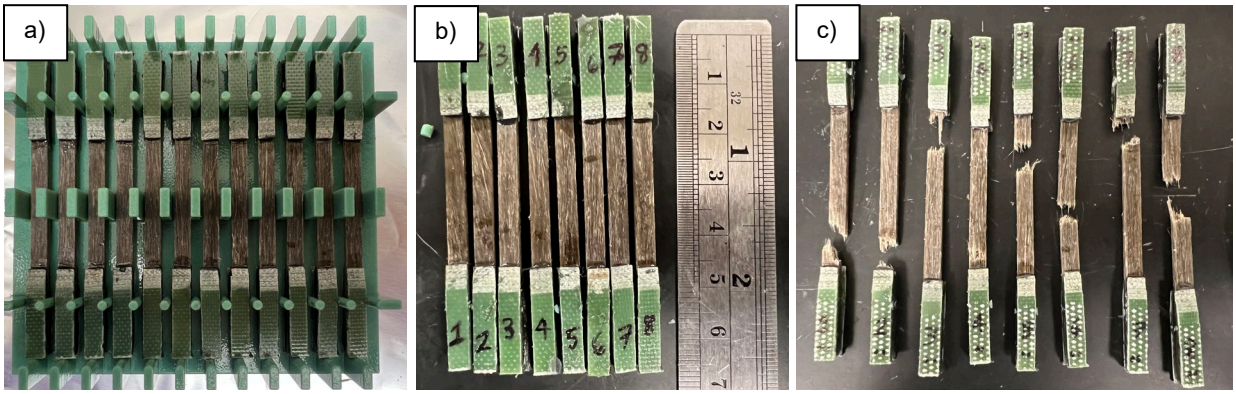

Figure 4.3: a) Fixture used to apply tabs to composite specimens, b) Composites ready for tensile testing. c) Composites after tensile testing showing failure within the specimen gauge length.

4.2.2 Interfacial Shear Strength

Interfacial shear strength measurements were collected via single-fiber pullout tests N = 11, min per sample).[102] Individual flax technical fibers were inserted into a small slit in a silicone mold, allowing for ~6 mm of fiber to enter the mold cavity. An optical microscope was used to verify the embedded length, as well as the two fiber diameters, D1 (major diameter) and D2 (minor diameter). The cavity was filled with a mixture of the same epoxy used to fabricate composites: Epon 862 + Epikure 3230 mixed at a ratio of 100:35 by weight. The sample was cured at 80°C for 8 hours. After curing, the specimen was removed from the mold and a tab of

tape was adhered via 3M General Use No Run Super Glue to the other end of the fiber for gripping, as shown in Figure 4.4. Each fiber pull-out test was performed using a 5 kN load cell on an Instron 5982 tensile machine at a displacement rate of 1mm/min. The interfacial shear strength (τ_{max}) was calculated using Equation 6 in which F_{max} is the max load recorded upon pullout of the fiber and L_e is the embedded length of the fiber. The denominator of Equation 6 uses Ramanujan's equation for the perimeter of an ellipse, multiplied by the embedded length to calculate surface area.

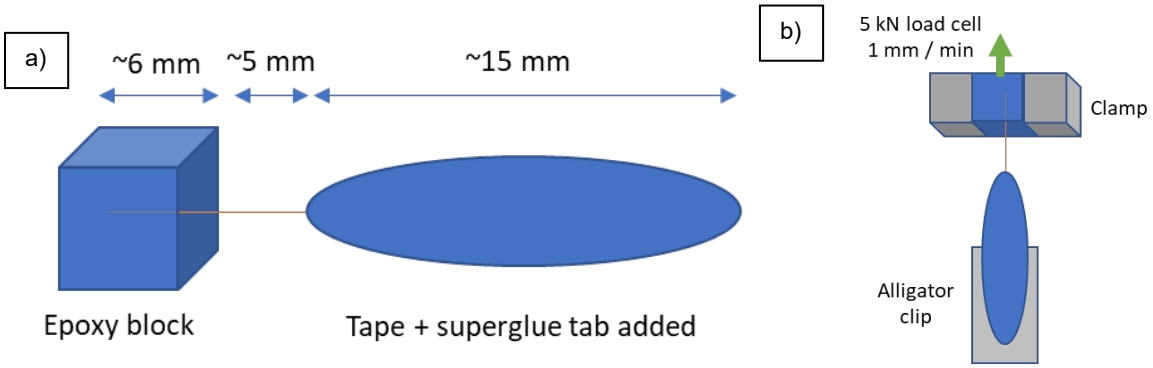

Figure 4.4: a) Schematic of prepared specimen for pull-out testing. b) Schematic for pull-out testing of specimens

$$\tau_{max} = \frac{F_{max}}{\pi L_e \left[3\left(\frac{D_1}{2}+\frac{D_2}{2}\right) - \sqrt{\left(\frac{3D_1}{2}+\frac{D_2}{2}\right)\left(\frac{D_1}{2}+\frac{3D_2}{2}\right)}\right]} \quad (6)$$

4.2.3 Fiber Size Distribution Analysis & Modeling

The fiber size distribution within untreated, 28MPa treated, and TiO_2 28MPa treated composites was analyzed. Fractured composite surfaces were polished using progressively finer silicon-carbide grinding paper followed by micron-sized diamond paste. Polished composite cross-sections were imaged using an Olympus inverted GX51 microscope at 10x magnification

followed by image analysis using the software ImageJ Fiji. Image processing was performed as shown in Figure 4.5: images were taken, fiber contrast was enhanced manually, and particle size analysis was performed using the built-in Analyze Particles function. Image analysis returned the cross-sectional area of each fiber within the composite. Three composite specimens were analyzed per sample; the specimens exhibiting the maximum, median, and lowest moduli per sample were analyzed.

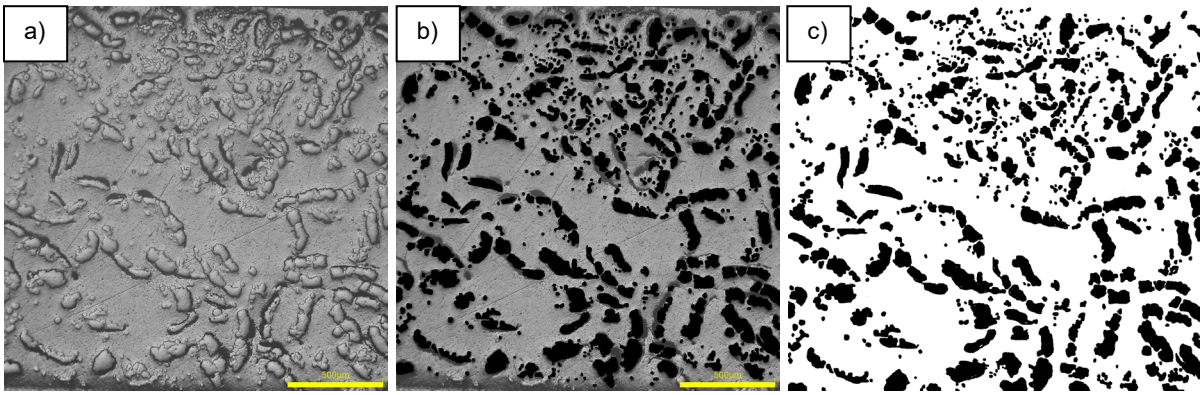

Figure 4.5: Image processing of composite cross-sections to enable fiber size distribution measurements. a) Original image of 30% TiO_2 28MPa epoxy composite after polishing. b) Enhanced contrast of fibers within epoxy matrix. c) Fibers detected using ImageJ Fiji software; sizes quantified.

A model was developed for the modulus of each fiber based on its cross-sectional area. Individual fiber moduli vs. cross-sectional areas of untreated fibers, 28MPa treated fibers, and TiO_2 28MPa treated fibers were gathered via single fiber tensile testing as described in Section 2.2.6 (moduli summarized in Figure 3.2.). Additional data for untreated technical flax fiber moduli vs fiber cross-sectional were gathered from Lamy, et al. [100] For treated samples (28MPa, TiO_2 28MPa), the data provided by Lamy, et al, was multiplied by the percentage increase in average fiber properties. For example, 28MPa treated fibers exhibited 33% higher modulus than untreated fibers, as determined via single fiber tensile testing (Figure 3.2); the

untreated flax moduli provided by Lamy, et al. were multiplied by 1.33 to approximate the improvement in fiber modulus due to treatment. Using the single fiber tensile data reported in this work combined with the tensile data from Lamy, et al, models for the relationship between fiber modulus and cross-sectional area were generated. An example of the model generated for untreated fibers is shown in Figure 4.6.

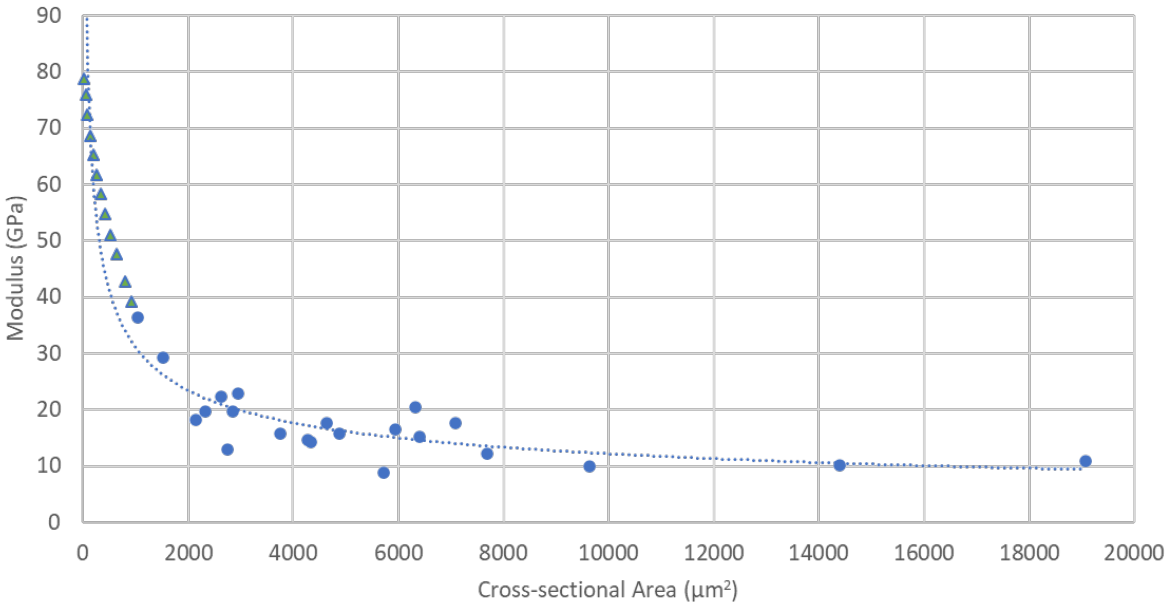

Figure 4.6: Model for the relationship between cross-sectional area of untreated fibers and fiber modulus. Points designated with a triangle were gathered from the literature. [100] All other data points were generated via single fiber tensile testing in this work, as summarized in Figure 3.2.

Each model consists of data points for cross-sectional area of fibers vs fiber modulus. Each cross-sectional area and modulus point within the models was treated as a bin, holding fibers smaller than its cross-sectional area value but larger than the next smallest cross-sectional area value in the model. Each fiber measured via image analysis of a polished composite cross-section was placed in a bin based on its size and assigned a modulus value. For example, an untreated fiber with a cross-sectional area of 9000 μm^2 was placed in the bin holding fibers

smaller than 9638 μm^2 but larger than 7683 μm^2 and assigned a modulus value of 9.9 GPa (Figure 4.6).

After assigning each fiber measured via image analysis a modulus value based on its cross-sectional area, the predicted average modulus of the fibers in each composite was calculated and designated as the "average weighted fiber modulus".

4.2.4 Scanning Electron Microscopy

Composite fracture surfaces were imaged using a JEOL JSM-IT500HR in secondary electron mode at 30kV and a working distance of 12mm. Fracture surfaces were carbon coated prior to imaging to provide a conductive path. The fracture type (fiber pull-out, fiber fracture) was evaluated visually.

4.3 Results

4.3.1 Interfacial Shear Strength (IFSS)

The IFSS of the flax-epoxy interface is shown for each fiber used to fabricate composites in Figure 4.7. Treatment at 28MPa resulted in an 8% reduction in interfacial shear strength. TiO_2 28MPa treatment resulted in a 17% reduction in interfacial shear strength, in comparison to the IFSS of untreated fibers. Previously, the surface area in pores was measured via gas physisorption and reported in Table 3.3. 28MPa and TiO_2 28MPa treatments resulted in a 25% and 98% reduction in surface area, respectively. Fiber surface roughness has been shown to affect mechanical interlocking between fibers and polymer matrices, with higher surface roughness resulting in higher IFSS. [103–105] It is likely that the surface smoothing that was observed via gas physisorption resulted in less mechanical entanglement between the fibers and

the epoxy matrix and reductions to IFSS. Future work could investigate if post-treatment surface modification of the fibers via chemical or physical treatments could improve IFSS and final composite properties.

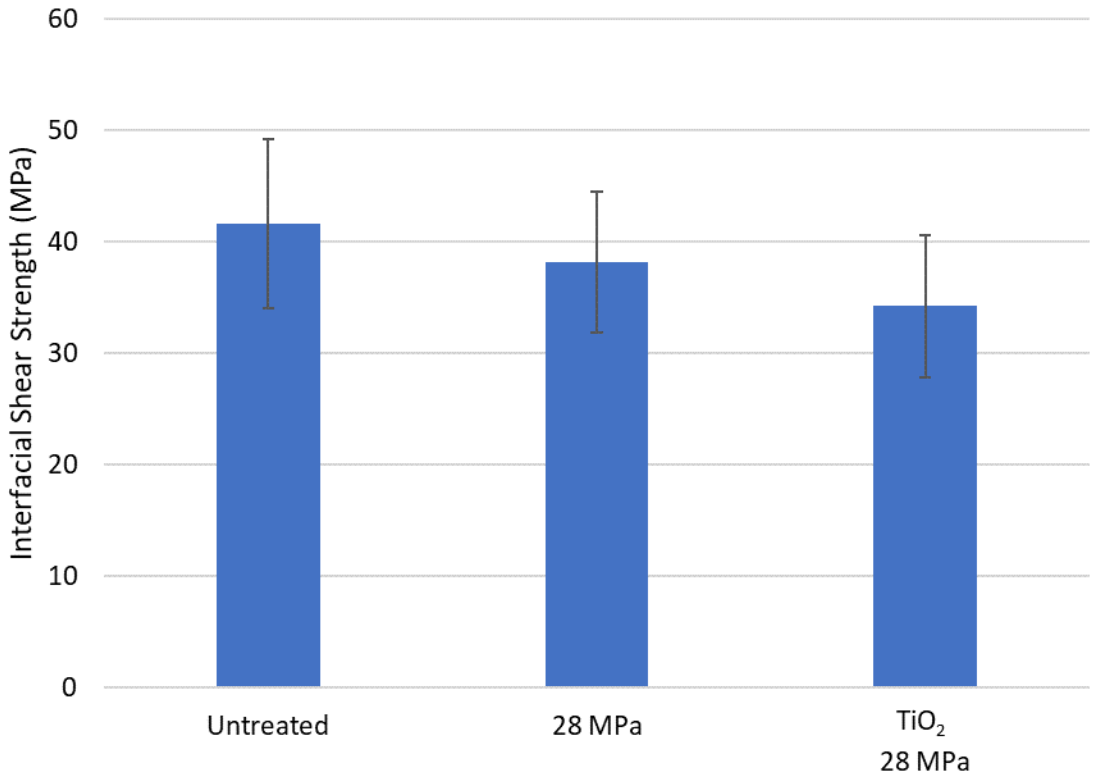

Figure 4.7: Interfacial shear strength of flax fibers used to fabricate composites.

4.3.2 Composite Tensile Properties

Composite tensile properties are summarized in Table 4.2. 28MPa treatment of fibers resulted in a 33% increase in composite modulus and a 25% increase in composite ultimate strength. Fibers which underwent TiO_2 28MPa treatment resulted in composites with 43% and 37% higher modulus and 37% higher strength than untreated fiber composites. Overall, as fiber tensile modulus and strength increased with treatment, composite tensile modulus and strength

also increased. A summary of the changes to fiber mechanical properties with treatment in comparison to changes in composite mechanical properties is shown in Table 4.3.

Table 4.2: Summary of composite tensile properties. Fiber treatments (28MPa, TiO_2 28MPa) resulted in increases to composite modulus and ultimate strength.

	Ultimate Strength		**Modulus**		**Strain at Break**	
	MPa		GPa		mm/mm	
30% Untreated	168.9	± 22.6	15.0	± 2.0	0.013	± 0.002
30% 28MPa	211.9	± 18.5	20.2	± 1.0	0.011	± 0.001
30% TiO_2 28MPa	231.5	± 9.5	21.4	± 1.6	0.013	± 0.001

Table 4.3: Summary of changes to tensile modulus and ultimate tensile strength of fibers and composites after 28MPa treatment and TiO_2 28MPa treatment.

Percent improvement compared to untreated				
	Modulus		**Strength**	
	Fiber	Composite	Fiber	Composite
28MPa	33%	33%	40%	25%
TiO_2 28MPa	71%	43%	80%	37%

Composite fracture surfaces were imaged using SEM and are shown in Figure 4.8-Figure 4.10. All fracture surfaces show that composite failure was a combination of fiber pull-out and fiber fracture. Additionally, the interface between the flax fiber and epoxy matrix in all specimens shows good wetting, as no visible debonding of the fibers from the matrix is apparent.

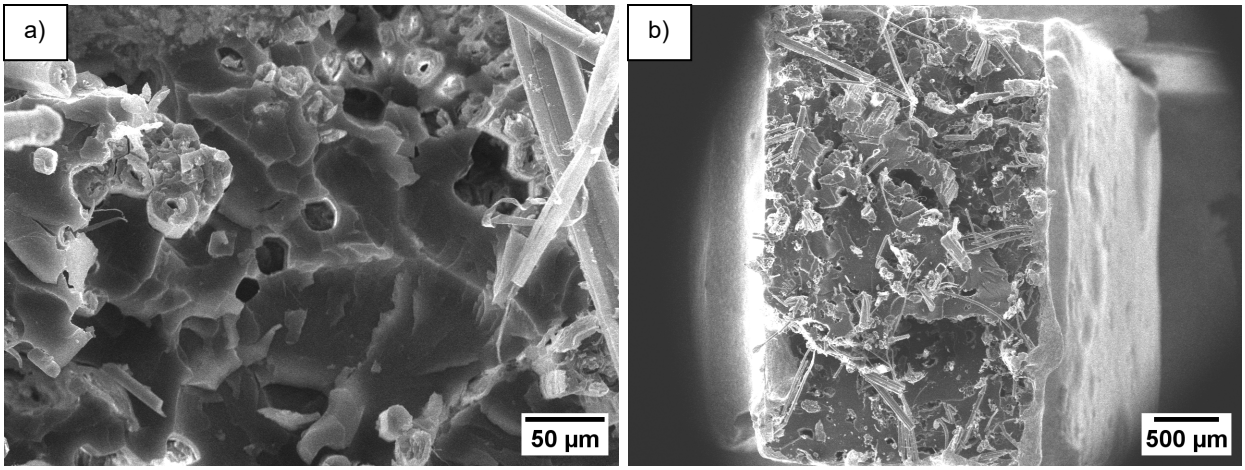

Figure 4.8: 30% untreated flax composite fracture surfaces showing a) failure mode is a combination of fiber fracture and fiber pull-out. Fiber-matrix interface shows good wetting of fibers. b) low-magnification view of specimen failure.

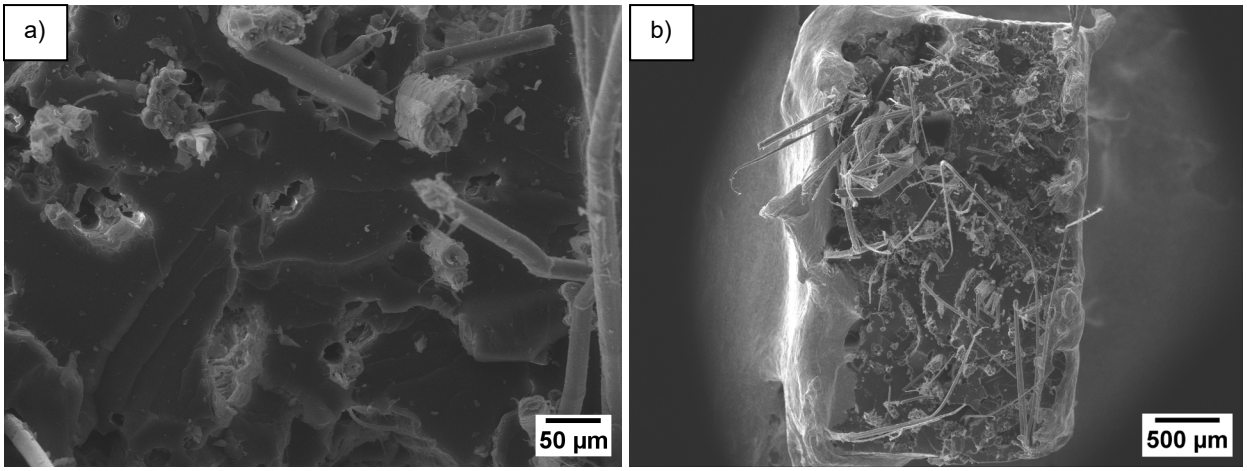

Figure 4.9: 30% 28MPa treated flax composite fracture surfaces showing a) failure mode is a combination of fiber fracture and fiber pull-out. Fiber-matrix interface shows good wetting of fibers. b) low-magnification view of specimen failure.

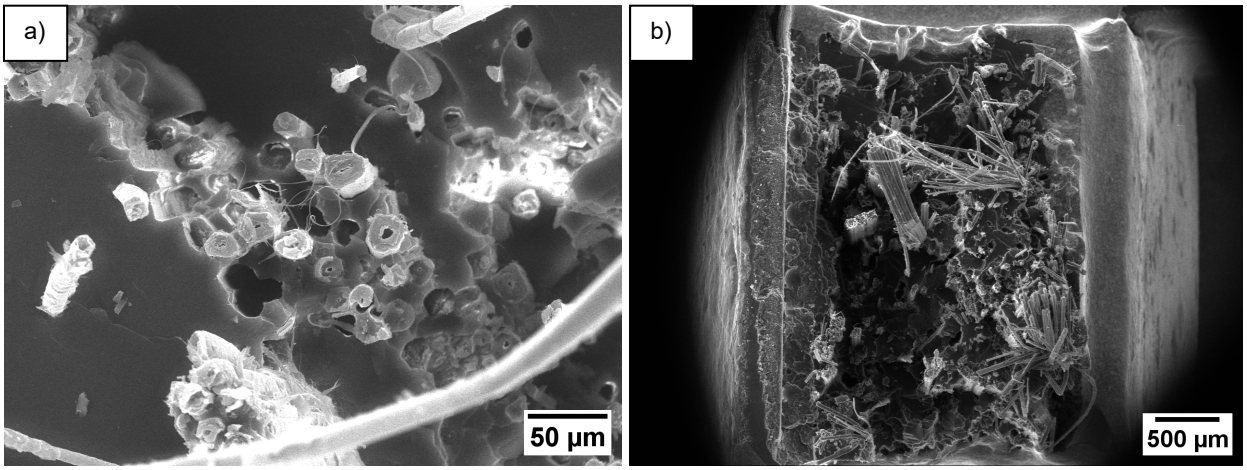

Figure 4.10: 30% 28MPa TiO_2 flax composite fracture surfaces showing a) failure mode is a combination of fiber fracture and fiber pull-out. Fiber-matrix interface shows good wetting of fibers. b) low-magnification view of specimen failure.

4.3.3 Fiber Size Distribution & Modeling

Composite specimens were polished and the fiber size distribution within each specimen was determined via image analysis. Composite cross-sections and their resulting fiber size distributions are shown in Figure 4.11 - Figure 4.13. Table 4.4 reports the median cross-sectional area of fibers within each composite. The composites containing TiO_2 28MPa fibers had a median fiber size 40% smaller than composites containing untreated fibers and 33% smaller than composites containing 28MPa treated fibers. This is consistent with prior analysis of technical fiber size via mounting and microtomy reported in Section 3.3.3, suggesting that treatment with 5nm TiO_2 results in fiber fibrillation. It is possible that some of the improvements to fiber and composite performance exhibited by the TiO_2 28MPa treated fibers is attributable to the reductions in fiber size.

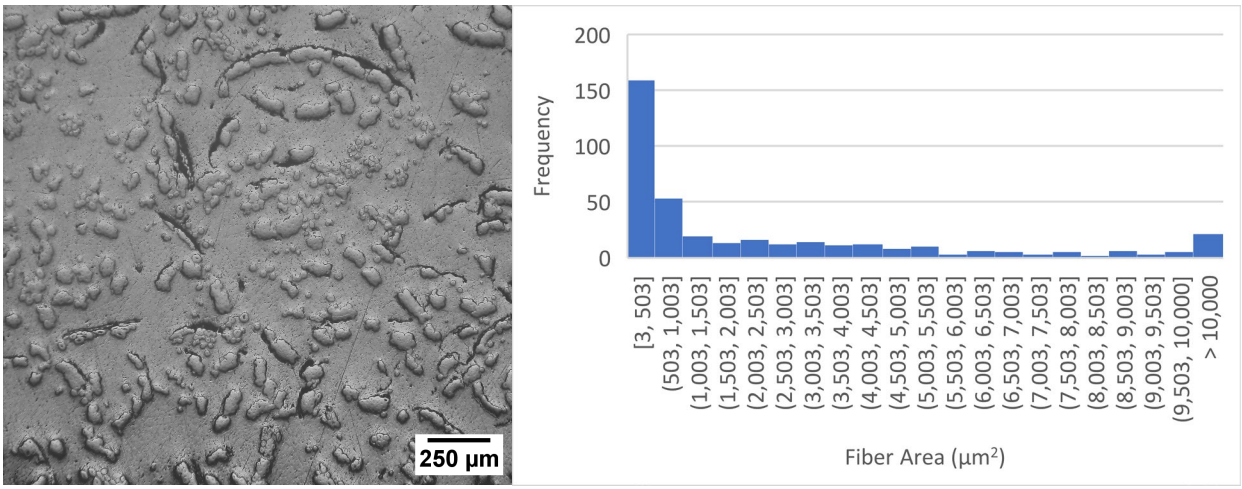

Figure 4.11: 30% untreated flax-epoxy composite cross-section and fiber size distribution. Specimen with median modulus in sample shown.

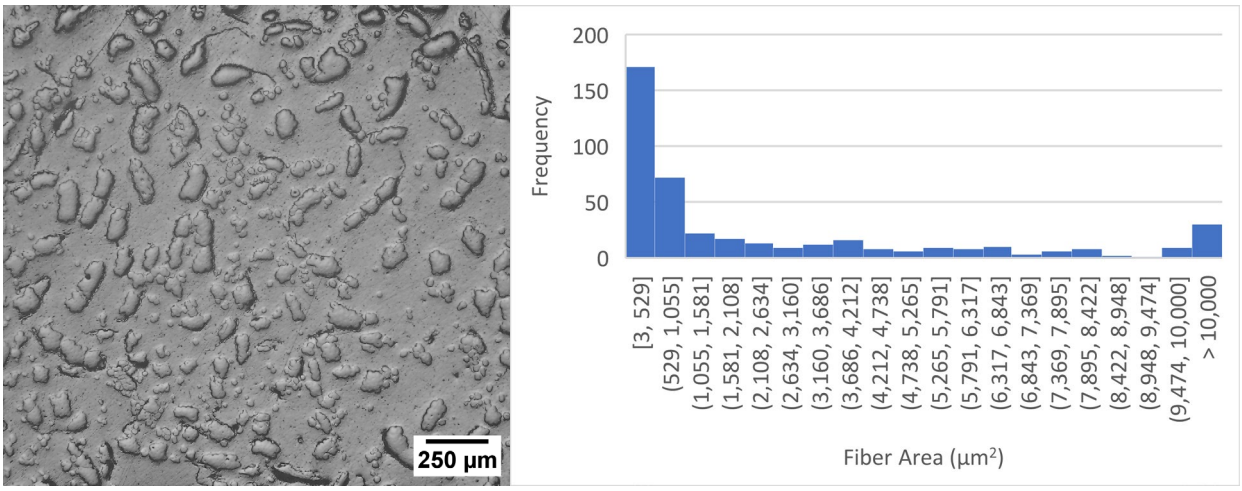

Figure 4.12: 30% 28 MPa treated flax-epoxy composite cross-section and fiber size distribution. Specimen with median modulus in sample shown.

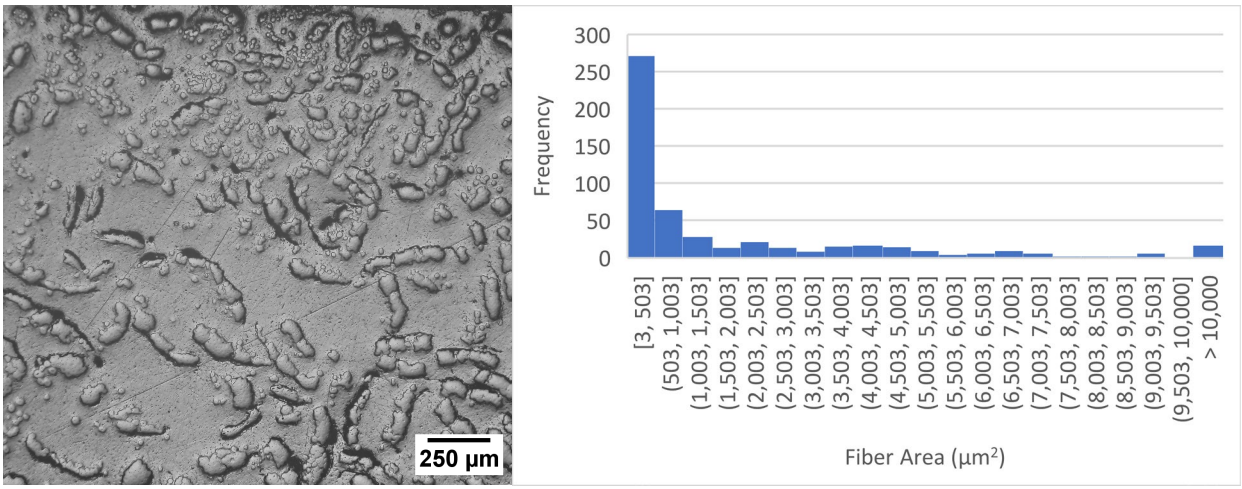

Figure 4.13: 30% TiO_2 28 MPa treated flax-epoxy composite cross-section and fiber size distribution. Specimen with median modulus in sample shown.

Table 4.4: Fiber cross-sectional area in composites containing untreated, 28MPa treated, and TiO_2 28MPa fibers. Average value calculated from fiber size distributions in composite specimens with lowest, median, and highest modulus in each sample.

	Median Fiber Size (μm^2)	
Untreated	880	± 113
28 MPa	781	± 219
TiO_2 28 MPa	524	± 69

Models for the relationship between fiber modulus and fiber cross-sectional area were generated for each fiber type, as shown in Figure 4.14. The average weighted fiber moduli for each sample are shown in Table 4.5. The average weighted fiber modulus determined from the models and the composite modulus determined experimentally were applied to Equation 7 (ROM) to back calculate fiber volume fraction in each sample (Table 4.5). For untreated fiber composites and 28MPa treated composites, the volume fraction of fiber predicted via ROM is ~30%, approximately equal to the volume fraction of fiber measured during composite fabrication. This suggests that this model, which takes into account fiber size as a non-negligible factor affecting composite modulus, is an appropriate representation of fiber performance within

untreated and 28MPa treated fiber composites. However, for TiO_2 28MPa treated composites, the volume fraction predicted via ROM is ~23%, lower than the experimentally measured value of 30 vol%. This model is predicting that the TiO_2 28MPa composites could exhibit higher modulus than observed experimentally. It is possible that the reduction in interfacial adhesion between TiO_2 28MPa treated fibers and the epoxy matrix, shown in Figure 4.7, is resulting in incomplete load transfer to the fibers, resulting in a reduction to experimentally measured composite modulus. It is suggested that future work explores the addition of coupling agents or compatibilizers within the composites to improve load transfer and determine if the models provided in this work are suitable for composites with improved load transfer.

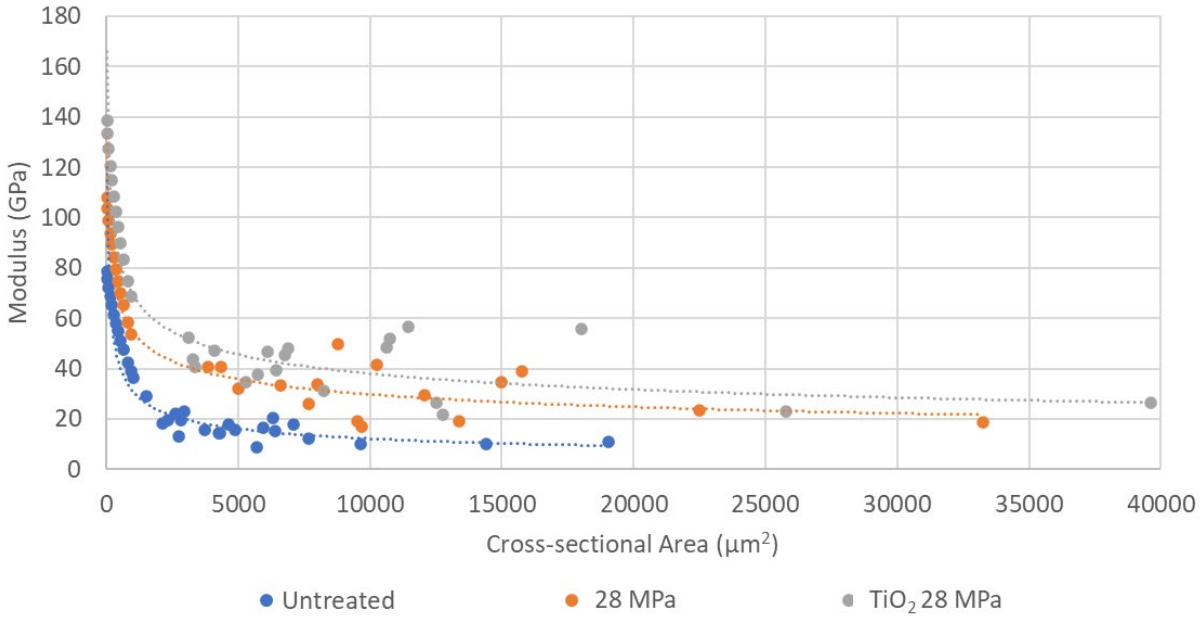

Figure 4.14: Models for relationship between fiber modulus and cross-sectional area for untreated, 28 MPa, and TiO_2 28 MPa treated fibers.

Table 4.5: Summary of weighted fiber moduli as calculated via the models shown in Figure 4.14.

Fiber Type	Volume Fraction (as measured during fabrication)		Average Weighted Fiber Modulus		Volume Fraction calculated from ROM
	%		GPa		%
Untreated	29.2%	± 0.3%	38.8	± 2.2	33%
28 MPa	29.8%	± 0.2%	60.6	± 2.3	29%
TiO_2 28 MPa	30.4%	± 0.2%	81.0	± 1.6	23%

4.4 Conclusions

Unidirectional epoxy composites were fabricated with 30 vol% flax technical fibers. Composites contained untreated, 28MPa, and TiO_2 28MPa $scCO_2$ treated flax fibers. Overall, improvements to flax fiber mechanical performance reported in Chapter 3 translated into improved composite mechanical properties. 28MPa treated flax composites exhibited 33% higher modulus and 25% higher strength than untreated flax composites. TiO_2 28MPa treated flax composites exhibited 43% higher modulus and 37% higher strength than untreated flax composites. The interfacial shear strength between the fibers and the epoxy matrix was measured via fiber pull-out testing. Treatment at 28MPa resulted in an 8% reduction in interfacial shear strength; TiO_2 28MPa treatment resulted in a 17% reduction in interfacial shear strength, compared to untreated fibers. The reductions in interfacial adhesion correlate with reductions to fiber surface area observed via nitrogen physisorption experiments in Chapter 3, Table 3.3.

Fiber size distributions were determined for each composite and the median fiber size was reported. 28MPa and TiO_2 28MPa fiber composites contained technical flax fibers that were, on average, 11% and 40% smaller than untreated fibers, respectively. Because of the dependence between technical fiber size and mechanical properties, models for fiber modulus based on fiber size were created and applied to the rule-of-mixtures. [10,28,100] The volume

fraction calculated for composites containing untreated and 28MPa treated fibers was predicted to be ~30%, suggesting that the new models were an appropriate representation of the fiber performance within each composite. However, for TiO_2 28MPa treated composites, the volume fraction predicted via ROM was ~23%, lower than the experimentally measured value of 30 vol%. It is possible that the reduction in interfacial adhesion between TiO_2 28MPa treated fibers and the epoxy matrix, reported via interfacial shear strength measurements, resulted in incomplete load transfer to the fibers and a reduction to experimentally measured composite modulus. Future work should explore methods to improve interfacial adhesion between treated fibers and the epoxy matrix.

Chapter 5 Conclusions

5.1 Key Findings

The development of lightweight structural composites has been increasing in recent years, in particularly as the transportation sector responds to consumer demand for the reduction of vehicle carbon footprints. Many structural composites contain glass-fiber as a reinforcing agent, with approximately 70% of glass fiber produced globally used in transportation or construction applications. However, glass fiber requires significant energy to produce and has a high density. As automakers look to reduce the weight and carbon footprints of their vehicles, the use of low-density, low carbon-footprint reinforcement of composite materials has been investigated, including the use of natural fibers.

Natural fibers have been extensively explored as a replacement for glass fiber in composites over the last 30 years. However, the high variability and low average mechanical properties of natural fibers has been a barrier to widescale replacement of glass in structural composites. [10,11] A variety of modification techniques have been explored previously, including chemical treatments, physical treatments, and extraction techniques, to attempt to improve natural fiber composite properties. [30–35]. Supercritical fluids, in particular supercritical CO_2 ($scCO_2$) have been explored as a means of improving the dyeability of natural fiber based textiles and extraction of lignocellulosic components. [39,41,53,54,45–52] However many of the techniques used previously to treat natural fibers in $scCO_2$ have also used high temperatures, high flow rates, and/or water as a co-solvent during treatment, and have reported extraction and/or degradation of fiber properties. This dissertation sought to improve upon prior

work to increase the modulus of flax fibers as a low cost, low carbon footprint alternative to glass reinforcement for structural composite applications.

Chapter 2 explored pre-treatment of flax fibers with aqueous solutions of nanoparticles via dip coating and sonication followed by treatment in $scCO_2$, with the goal of incorporating nanomaterials within the pectin-rich middle lamella to improve load transfer between elementary fibers. Treatment with aqueous solutions of Fe_3O_4 nanoparticles showed significant agglomeration of nanoparticles on the fiber surface. Additionally, pre-treatment via sonication resulted in the formation of micro-cracks on the fiber surface, suggesting that sonication results in fiber damage. All fibers treated with Fe_3O_4 nanoparticles via dip coating, sonication, and/or $scCO_2$ treatments resulted in reductions to fiber modulus and strength, as determined via single fiber tensile testing. Treatment of fibers in aqueous nanoparticle solutions was further explored via dip coating of TiO_2 nanoparticles followed by $scCO_2$ treatment. No improvements to fiber performance were observed via single fiber tensile testing. Proof of concept experiments were conducted using pectin films treated in $scCO_2$ with TiO_2 nanoparticles. Nanoparticles were observed to be dispersed throughout the pectin cross-sections via TOF-SIMS. Image analysis of TOF-SIMS images found that longer durations and higher pressures resulted in an increase in Ti signal from within the pectin films. Treatment of samples directly in $scCO_2$ at 28MPa, 60°C, for 24hr resulted in the strongest Ti signal via TOF-SIMS analysis of pectin films and was explored further in subsequent chapters.

Chapter 3 studied the treatment of flax fibers with TiO_2 nanoparticles in $scCO_2$. Treatment in $scCO_2$ at 28MPa, 60°C, for 24hr resulted in increases to fiber modulus and strength by 33% and 40%, respectively. Treatment resulted in densification of the fibers by 5% and a 50% reduction in total porosity, including the collapse of lumen in elementary fibers. A 1%

increase in average fiber crystallinity was observed. ATR-FTIR was used to evaluate the bulk chemistry of the fibers after 28MPa treatment. No significant changes to composition or selective removal of lignocellulosic components was observed.

Treatment of flax at 28 MPa, 60°C, for 24hr with 5nm TiO_2 nanoparticles (TiO_2 28MPa treatment) resulted in a 71% and 80% increase in fiber modulus and strength, respectively. No nanoparticles were detected within the fiber structure after treatment, as determined via PFIB-SEM, TEM, and EDS. Crystallinity of TiO_2 28MPa treated fibers increased by 11%, compared to untreated fibers. Treatment resulted in a 70% reduction in total porosity and a 98% reduction to fiber surface area, suggesting that TiO_2 nanoparticles could be inducing pore closure and smoothing of the fiber surface. In addition, TiO_2 28MPa treatment resulted in a reduction to fiber cross-sectional area, suggesting that treatment results in fibrillation of the technical fibers. Two mechanisms for changes to fiber morphology and structure were proposed: 1) fiber fibrillation and 2) shot peening of the fiber.

In Chapter 4, 30 vol% flax-epoxy composites were created via vacuum assisted molding. Improvements to fiber properties via treatment (as reported in Chapter 3) resulted in improvements to their resulting composite properties. Treatment of fibers in $scCO_2$ at 28MPa, 60°C, for 24hr (28MPa treatment) resulted in composites with 33% higher modulus and 25% higher strength than untreated flax composites, despite an 8% reduction in interfacial shear strength, measured via fiber pull-out testing. The addition of 5nm TiO_2 nanoparticles during treatment (TiO_2 28MPa treatment) resulted in composites with 43% higher modulus and 37% higher strength than untreated flax composites.

28MPa and TiO_2 28MPa fiber composites contained technical flax fibers that were, on average, 11% and 40% smaller than untreated fibers, respectively. Models for predicting fiber

modulus were created accounting for the dependence between fiber size and fiber modulus. The predicted fiber moduli were applied to the rule-of-mixtures. The volume fraction calculated for composites containing untreated and 28MPa treated fibers was predicted to be ~30%, suggesting that the new models were an appropriate representation of the fiber performance within these composites. However, the rule-of-mixtures back-calculated volume fraction of fibers for TiO_2 28MPa treated composites was ~23%, lower than the experimentally measured value of 30 vol%. TiO_2 28MPa treatment resulted in a 17% reduction in interfacial shear strength, compared to untreated fibers, consistent with reductions to fiber surface area observed in Chapter 3. It is possible that the reduction in interfacial adhesion between TiO_2 28MPa treated fibers and the epoxy matrix, resulted in incomplete load transfer to the fibers.

This work contributes a set of treatment parameters capable of improving the mechanical properties of flax fibers to the literature. Observations to changes in fiber structure (crystallinity, porosity, surface area), and morphology (lumen collapse, technical fiber cross-sectional area) as well as hypotheses for the mechanisms occurring during treatment will enable future optimization of this process. Experiments focused on understanding the mechanisms occurring are suggested as primary next steps. Additionally, new models for predicting composite modulus based on the dependency between fiber size and fiber modulus were created as a part of this work. Future studies may apply this modification to rule of mixtures to better predict composite properties. Overall, this work has laid the groundwork for development of a cost-effective, optimized treatment capable of improving the mechanical properties of flax fibers and their resulting composites.

5.2 Recommendations for Future Work

In Chapters 2-4, treatment of flax fibers with supercritical CO_2 was explored and possible mechanisms for improved properties, changes to morphology, and changes to structure were proposed. To better understand the mechanisms at play, it is suggested that future work explore different parameters during treatment (e.g. different pressures, different nanoparticle chemistries, different fluids, different sizes of nanomaterials, etc..).

Some initial work has been completed to begin exploring the effects of different fluids and different particle sizes on the structure and performance of the resulting fibers. Direct treatment of 6 cm long fibers with TiO_2 nanoparticles in supercritical fluid was performed according to the experimental conditions outlined in Table 5.1. Treatments were performed using supercritical nitrogen (scN_2), supercritical argon (scAr), larger nanoparticles (100nm TiO_2), as well as treatment in $scCO_2$ at 19MPa, an intermediate pressure to those explored in Chapters 2-4 (10MPa & 28MPa).

The materials (flax fibers, TiO_2 nanoparticles) used for this work were as described in Chapter 2, Section 2.2.1. Equipment used and treatment process flow were performed as described in Chapter 3, Section 3.2. Evaluation of fiber mechanical properties was determined via single fiber tensile testing, as previously described in Chapter 2, Section 2.2.6. Fiber crystallinity was determined via XRD, as described in Chapter 3, Section 3.2.3.

Table 5.1: Experimental design outlining additional treatments performed on flax fibers in supercritical N_2, Ar, and CO_2, with and without 5nm and 100nm TiO_2 nanoparticles.

Sample Name	Sample Type	Fluid Type	Pressure [MPa]	Time Duration [hours]	Temperature [°C]	Depressurization rate [MPa / min]	Nanoparticle Type
Untreated	Flax	-	-	-	-	-	-
scAr 28 MPa	Flax	scAr	28	24	60	2	-
scN_2 28 MPa	Flax	scN_2	28	24	60	2	-
TiO_2 scN_2 28 MPa	Flax	scN_2	28	24	60	2	5nm TiO_2
100nm TiO_2 28 MPa	Flax	$scCO_2$	28	24	60	2	100nm TiO_2
TiO_2 19 MPa	Flax	$scCO_2$	19	24	60	2	5nm TiO_2

The crystallinity indices for fibers treated per Table 5.1 are reported in Table 5.2. Figure 5.1 summarizes the crystallinity indices for fibers treated in $scCO_2$, with and without TiO_2 nanoparticles. TiO_2 19MPa treatment resulted in an average fiber crystallinity of 78%. TiO_2 10MPa and TiO_2 28MPa treatments resulted in crystallinity values of 73% and 81%, respectively. This suggests that the pressure of treatment in $scCO_2$ with 5nm TiO_2 has a direct effect on the final crystallinity of the fibers, with higher pressures resulting in higher fiber crystallinity. Treatment with a larger nanoparticle via 100nm TiO_2 28MPa treatment resulted in fibers with 80% crystallinity. Treatment with 5nm TiO_2 via TiO_2 28MPa treatment resulted in similar fiber crystallinity – 80%. This suggests that the nanoparticle size does not significantly affect final fiber crystallinity upon treatment. However, future work should explore a wider range of particle sizes, including micron-sized powders to better understand the mechanism occurring to induce crystallinity.

Figure 5.2 summarizes the crystallinity indices for fibers treated in scAr and scN_2, with and without TiO_2 nanoparticles. scAr 28MPa treatment resulted in 71% average crystallinity,

similar to the crystallinity of fibers which underwent $scCO_2$ 28MPa treatment (treatment name: 28MPa). However, scN_2 28MPa treatment resulted in fibers with an average crystallinity of 77%, suggesting that the difference in chemical composition of the supercritical fluid could influence the final crystallinity of the fibers. Additionally, TiO_2 scN_2 28MPa treatment resulted in fibers with 82% crystallinity, suggesting that the addition of 5nm TiO_2 nanoparticles to treatments in fluids other than $scCO_2$ or scN_2 could result in additional increases to crystallinity.

Table 5.2: Crystallinity index of fibers treated per the experimental design outlined in Table 5.1.

	Segal Crystallinity Index (%)
scAr 28 MPa	71 ± 4
scN_2 28 MPa	77 ± 7
TiO_2 scN_2 28 MPa	82 ± 1
100nm TiO_2 28 MPa	80 ± 4
TiO_2 19 MPa	78 ± 6

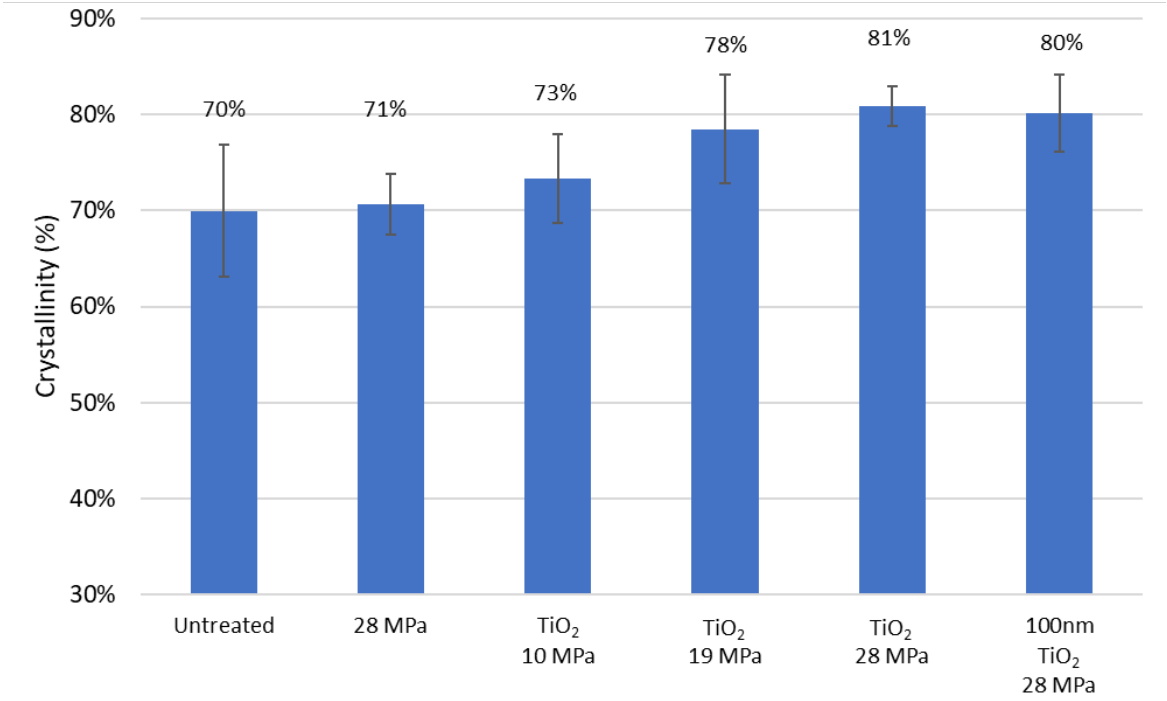

Figure 5.1: Summary of crystallinity index for fibers which underwent treatment in $scCO_2$ with and without nanomaterials. Treatment conditions for fibers can be found in Table 3.1 and Table 5.1.

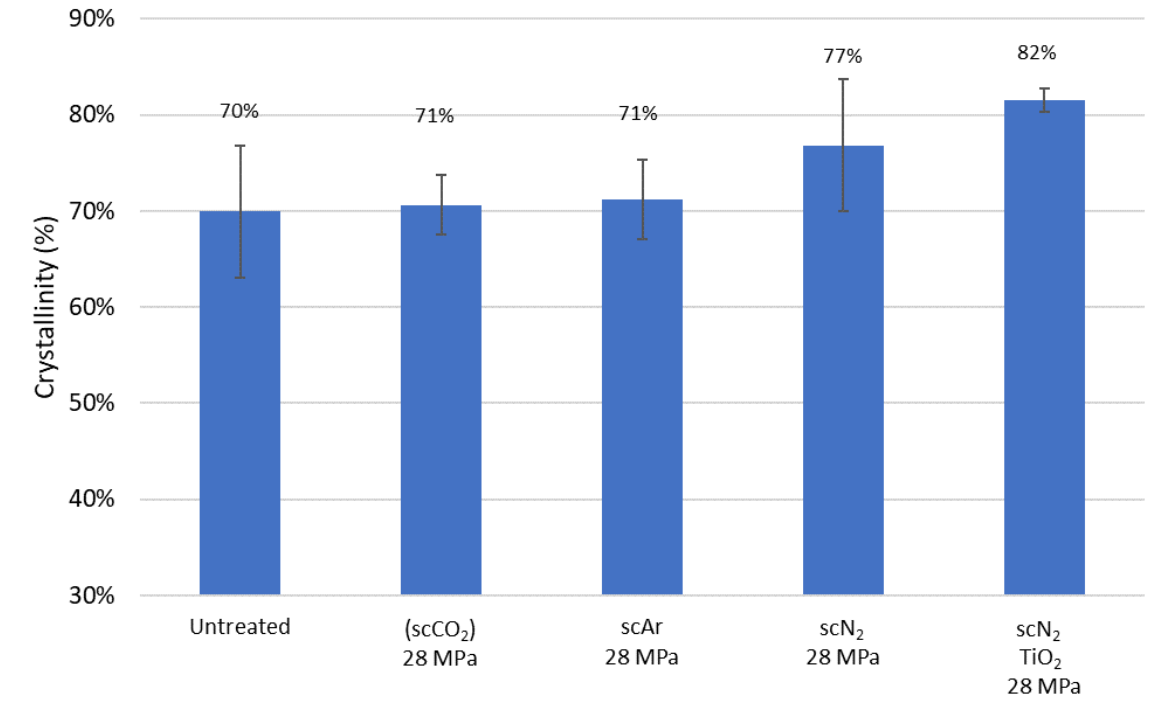

Figure 5.2: Summary of crystallinity index for fibers which underwent treatment in $scCO_2$, scN_2 and scAr with and without nanomaterials. Treatment conditions for fibers can be found in Table 5.1.

The mechanical properties of fibers which underwent treatments in $scCO_2$ with and without TiO_2 nanoparticles are summarized in Figure 5.3. Interestingly, while increasing pressure of treatment with TiO_2 nanoparticles resulted in steadily increasing crystallinity indices, the average modulus and strength of fibers which underwent TiO_2 19MPa treatment were slightly lower than the average modulus and strength of fibers which underwent TiO_2 10MPa treatment. Future work should visualize the 100nm TiO_2 28MPa treated fibers via SEM and determine if fiber damage occurred during treatment. Future work should also evaluate several other treatment pressures to better understand the relationship between pressure and fiber mechanical properties.

100nm TiO_2 28MPa treatment of fibers did not improve fiber modulus or strength, compared to untreated fibers. In fact, compared to TiO_2 28MPa treatment (with 5nm TiO_2), use of 100nm TiO_2 nanoparticles resulted in a 49% reduction in modulus and a 46% reduction in strength, despite the nearly equivalent fiber crystallinity reported in Figure 5.1. It is possible that the 100nm TiO_2 nanoparticles are inducing microcracks on the fiber surface or between elementary fibers, resulting in reduced load transfer under tension. Future work should examine the changes in 100nm TiO_2 28MPa fiber morphology and surface structure to enable comparisons to TiO_2 28MPa treated fibers. Future work should also evaluate how particle size affects final fiber properties and structure, including evaluation of particles between 5nm and 100nm in size. Additionally, TiO_2 is known for its catalytic properties. It is suggested that future work evaluate treatment with different chemistry particles, including fibers treated with alumina, silica, and/ or nanoclays.

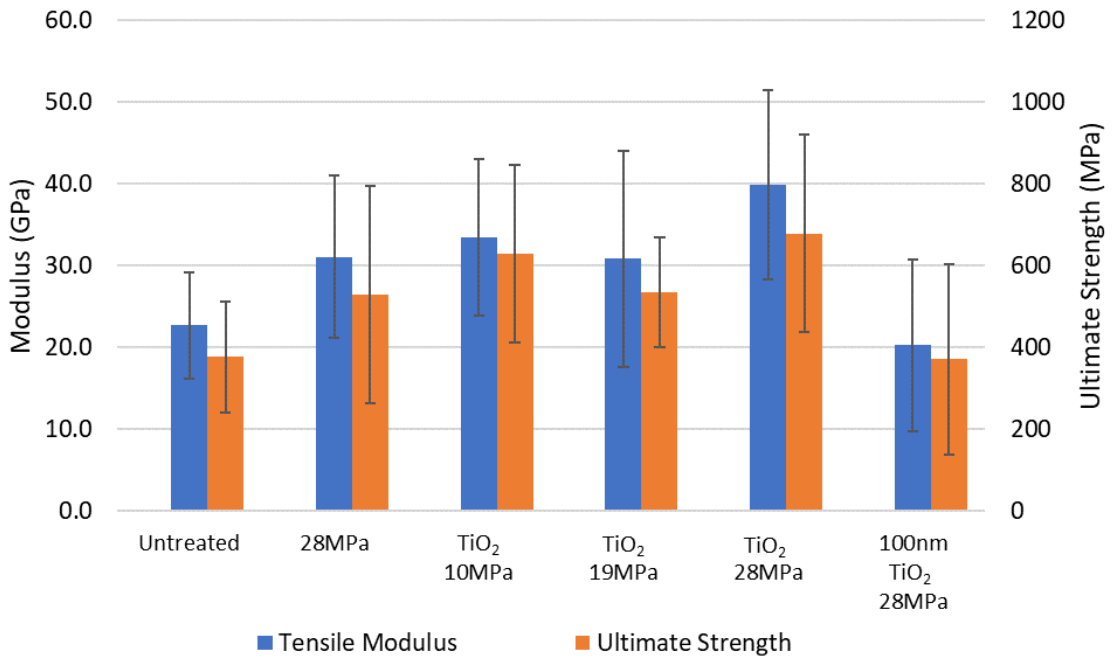

Figure 5.3: Summary of tensile properties flax fibers after treatment in $scCO_2$ with and without TiO_2 nanoparticles.

The mechanical properties of fibers treated in scAr and scN_2 are shown in Figure 5.4. scAr 28MPa and scN_2 28MPa treatment of fibers resulted in an average modulus of 29MPa, similar to the stiffness of ($scCO_2$) 28MPa treated fibers. However, the crystallinity of scN_2 28MPa treated fibers was 6% higher than that of ($scCO_2$) 28MPa treated fibers (Figure 5.1-Figure 5.2). Additionally, scN_2 TiO_2 28MPa treatment of fibers resulted in a significant reduction in modulus, compared to fibers treated without nanoparticles in nitrogen (scN_2 28MPa).

This suggests that a) fiber crystallinity does not always correlate with fiber mechanical properties and b) 5nm TiO_2 nanoparticles may interact differently with the fiber in the presence of different fluids. It is possible that differences in fluid density could be contributing to the different trends reported in Figure 5.1-Figure 5.4. The densities of scN_2 and $scCO_2$ at 28MPa and 60°C are 0.246 g/cm^3 and 0.810 g/cm^3; it is possible that the differences in density are affecting molecule and particle mobility within the pressure vessel during treatment. It is suggested that

future work analyze particle and fluid dynamics via modelling and tailored experiments to further the understanding of what mechanisms are occurring during treatments under different conditions. Additionally, it is possible that different fluid chemistries result in different levels of material extraction from the fiber. Future work should fully evaluate changes to fiber chemistry upon treatment in different fluids to determine if subtle changes to material chemistry are occurring.

Finally, this work focused on the treatment of one particular flax fiber cultivated and extracted in a very controlled manner. It is suggested that future work apply these treatments to flax fibers grown under different conditions and with different initial mechanical properties, crystallinities, and porosities, to see if changes to fiber properties translate to different species and fibers with different starting conditions.

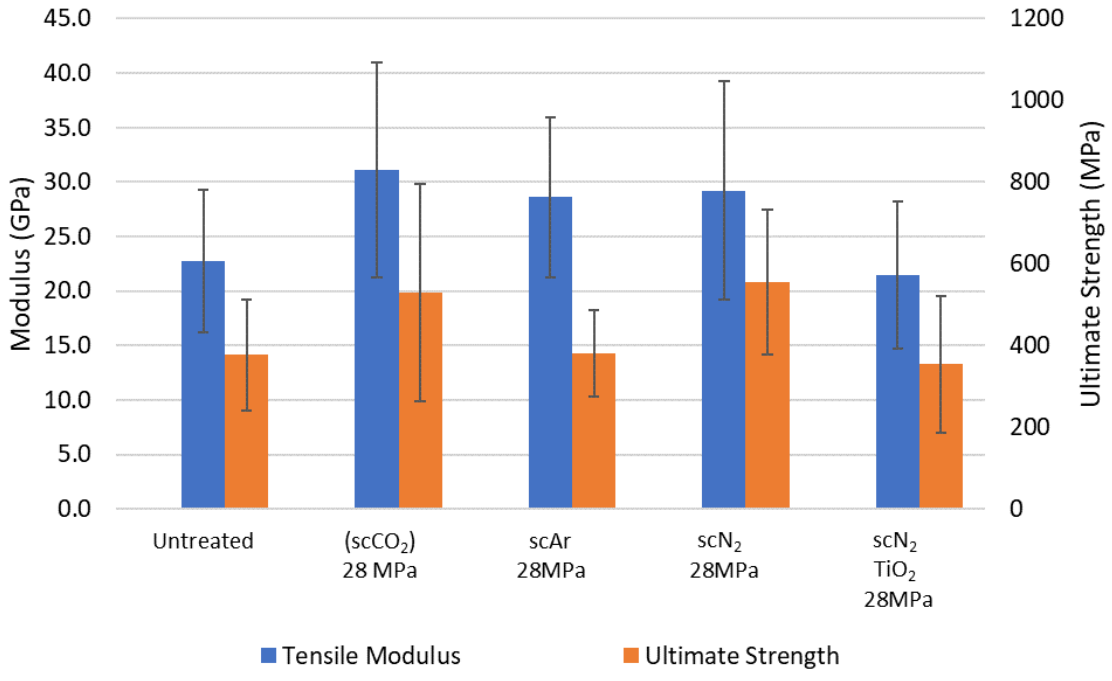

Figure 5.4: Summary of tensile properties flax fibers after treatment in $scCO_2$, scN_2 and scAr at 28MPa with and without 5nm TiO_2 nanoparticles.

Bibliography

[1] U.S.E.I. Administration, Transportation sector energy consumption, Int. Energy Outlook 2016. 2016 (2016) 127–137. https://www.eia.gov/outlooks/ieo/pdf/transportation.pdf.

[2] L. Miller, K. Soulliere, S. Sawyer-Beaulieu, S. Tseng, E. Tam, Challenges and alternatives to plastics recycling in the automotive sector, Materials (Basel). (2014). https://doi.org/10.3390/ma7085883.

[3] S. Jenkins, Electric Vehicles Drive Performance Polymers, 2021. https://www.chemengonline.com/electric-vehicles-drive-performance-polymers/?printmode=1 (accessed May 6, 2022).

[4] W. Joost, Energy, Materials, and Vehicle Weight Reduction, (n.d.). www.eia.gov (accessed December 29, 2022).

[5] A.A. Luo, Recent advances in light metals and manufacturing for automotive applications, CIM J. 12 (2021) 79–87. https://doi.org/10.1080/19236026.2021.1947088.

[6] Department of Energy, Lightweight Materials for Cars and Trucks, n.d. https://www.energy.gov/eere/vehicles/lightweight-materials-cars-and-trucks (accessed March 1, 2023).

[7] A. Langhorst, E. Harrison, A. Singhal, M. Banu, A. Taub, Reinforcement of Natural Fibers via Supercritical Fluid Infiltration of Nanoparticles, in: Am. Soc. Compos. Thirty-Seventh Tech. Conf., 2022.

[8] P. Wambua, J. Ivens, I. Verpoest, Natural fibres: Can they replace glass in fibre reinforced plastics?, Compos. Sci. Technol. 63 (2003) 1259–1264. https://doi.org/10.1016/S0266-3538(03)00096-4.

[9] W.P. Schmidt, H.M. Beyer, Life cycle study on a natural fibre reinforced component, in: SAE Tech. Pap., 1998: pp. 2095–2102. https://doi.org/10.4271/982195.

[10] A. Bourmaud, C. Morvan, C. Baley, Importance of fiber preparation to optimize the surface and mechanical properties of unitary flax fiber, Ind. Crops Prod. 32 (2010) 662–667. https://doi.org/10.1016/j.indcrop.2010.08.002.

[11] M. Hughes, Defects in natural fibres: their origin, characteristics and implications for natural fibre-reinforced composites, J. Mater. Sci. 47 (2012) 599–609. https://doi.org/10.1007/s10853-011-6025-3.

[12] E. Trujillo, M. Moesen, L. Osorio, A.W. Van Vuure, J. Ivens, I. Verpoest, Bamboo fibres for reinforcement in composite materials: Strength Weibull analysis, Compos. Part A Appl. Sci. Manuf. 61 (2014) 115–125. https://doi.org/10.1016/j.compositesa.2014.02.003.

[13] K.L. Pickering, M.G.A. Efendy, T.M. Le, A review of recent developments in natural fibre composites and their mechanical performance, Compos. Part A Appl. Sci. Manuf. (2016). https://doi.org/10.1016/j.compositesa.2015.08.038.

[14] J. Müssig, Industrial Applications of Natural Fibres: Structure, Properties and Technical Applications, 2010. https://doi.org/10.1002/9780470660324.

[15] I. Van de Weyenberg, J. Ivens, A. De Coster, B. Kino, E. Baetens, I. Verpoest, Influence of processing and chemical treatment of flax fibres on their composites, Compos. Sci. Technol. (2003). https://doi.org/10.1016/S0266-3538(03)00093-9.

[16] R.F. Evert, Esau's Plant Anatomy, John Wiley & Sons, Inc., Hoboken, NJ, USA, 2006. https://doi.org/10.1002/0470047380.

[17] E. Richely, S. Durand, A. Melelli, A. Kao, A. Magueresse, H. Dhakal, T. Gorshkova, F. Callebert, A. Bourmaud, J. Beaugrand, S. Guessasma, Novel insight into the intricate shape of flax fibre lumen, Fibers. 9 (2021). https://doi.org/10.3390/fib9040024.

[18] A. Bourmaud, C. Morvan, A. Bouali, V. Placet, P. Perre, C. Baley, P. Perré, C. Baley, Relationships between micro-fibrillar angle, mechanical properties and biochemical composition of flax fibers, Ind. Crops Prod. 44 (2013) 343–351. https://doi.org/10.1016/j.indcrop.2012.11.031.

[19] J. Beaugrand, S. Guessasma, J.E. Maigret, Damage mechanisms in defected natural fibers, Sci. Reports 2017 71. 7 (2017) 1–7. https://doi.org/10.1038/s41598-017-14514-6.

[20] A.K. Bledzki, J. Gassan, Composites reinforced with cellulose based fibres, 1999. https://doi.org/10.1016/S0079-6700(98)00018-5.

[21] C. Goudenhooft, A. Bourmaud, C. Baley, Flax (Linum usitatissimum L.) Fibers for Composite Reinforcement: Exploring the Link Between Plant Growth, Cell Walls Development, and Fiber Properties, Front. Plant Sci. 10 (2019) 1–23. https://doi.org/10.3389/fpls.2019.00411.

[22] K. Charlet, C. Baley, C. Morvan, J.P. Jernot, M. Gomina, J. Bréard, Characteristics of Hermès flax fibres as a function of their location in the stem and properties of the derived unidirectional composites, Compos. Part A Appl. Sci. Manuf. 38 (2007) 1912–1921. https://doi.org/10.1016/j.compositesa.2007.03.006.

[23] O. Faruk, A.K. Bledzki, H.-P. Fink, M. Sain, Biocomposites reinforced with natural fibers: 2000-2010, Prog. Polym. Sci. 37 (2012) 1552–1596. https://doi.org/10.1016/j.progpolymsci.2012.04.003.

[24] H.L. Bos, The potential of flax fibres as reinforcement for composite materials,

Eindhoven: Technische Universiteit Eindhoven, 2004. http://www.tue.nl/bib (accessed February 21, 2019).

[25] M. Le Gall, P. Davies, N. Martin, C. Baley, Recommended flax fibre density values for composite property predictions, Ind. Crops Prod. 114 (2018) 52–58. https://doi.org/10.1016/J.INDCROP.2018.01.065.

[26] G. Romhány, J. Karger-Kocsis, T. Czigány, Tensile Fracture and Failure Behavior of Technical Flax Fibers, J. Appl. Polym. Sci. 90 (2003) 3638–3645. https://doi.org/10.1002/app.13110.

[27] K. Charlet, A. Béakou, Mechanical properties of interfaces within a flax bundle Part I: Experimental analysis, Int. J. Adhes. Adhes. 31 (2011) 875–881. https://doi.org/10.1016/j.ijadhadh.2011.08.008.

[28] A.B. Bevitori, I.L.A. da Silva, F.P.D. Lopes, S.N. Monteiro, Diameter dependence of tensile strength by weibull analysis: Part ii jute fiber, Rev. Mater. (2010). https://doi.org/10.1590/s1517-70762010000200005.

[29] W.G. Hopkins, N.P.A. Huner, Introduction to plant physiology., 2004.

[30] X. Li, L.G. Tabil, S. Panigrahi, Chemical treatments of natural fiber for use in natural fiber-reinforced composites: A review, J. Polym. Environ. (2007). https://doi.org/10.1007/s10924-006-0042-3.

[31] M.Z. Rong, M.Q. Zhang, Y. Liu, G.C. Yang, H.M. Zeng, The effect of fiber treatment on the mechanical properties of unidirectional sisal-reinforced epoxy composites, Compos. Sci. Technol. 61 (2001) 1437–1447. https://doi.org/10.1016/S0266-3538(01)00046-X.

[32] A. Arbelaiz, B. Fernández, G. Cantero, R. Llano-Ponte, A. Valea, I. Mondragon, Mechanical properties of flax fibre/polypropylene composites. Influence of fibre/matrix modification and glass fibre hybridization, Compos. Part A Appl. Sci. Manuf. 36 (2005) 1637–1644. https://doi.org/10.1016/j.compositesa.2005.03.021.

[33] L. Sobczak, O. Brüggemann, R.F. Putz, Polyolefin composites with natural fibers and wood-modification of the fiber/filler-matrix interaction, J. Appl. Polym. Sci. 127 (2013) 1–17. https://doi.org/10.1002/app.36935.

[34] S. M.R., S. Siengchin, J. Parameswaranpillai, M. Jawaid, C.I. Pruncu, A. Khan, M.R. Sanjay, S. Siengchin, J. Parameswaranpillai, M. Jawaid, C.I. Pruncu, A. Khan, A comprehensive review of techniques for natural fibers as reinforcement in composites: Preparation, processing and characterization, 2019. https://doi.org/10.1016/j.carbpol.2018.11.083.

[35] M.M. Kabir, H. Wang, K.T. Lau, F. Cardona, Chemical treatments on plant-based natural fibre reinforced polymer composites: An overview, Compos. Part B Eng. 43 (2012) 2883–2892. https://doi.org/10.1016/J.COMPOSITESB.2012.04.053.

[36] T. Nishino, K. Takano, K. Nakamae, Elastic modulus of the crystalline regions of cellulose polymorphs, J. Polym. Sci. Part B Polym. Phys. (1995). https://doi.org/10.1002/polb.1995.090331110.

[37] M.J. John, R.D. Anandjiwala, Recent developments in chemical modification and characterization of natural fiber-reinforced composites, Polym. Compos. 29 (2008) 187–207. https://doi.org/10.1002/pc.20461.

[38] S. Pérez, D. Samain, Structure and Engineering of Celluloses, in: Adv. Carbohydr. Chem. Biochem., 2010. https://doi.org/10.1016/S0065-2318(10)64003-6.

[39] A. Schmidt, E. Bach, E. Schollmeyer, Damage to Natural and Synthetic Fibers Treated in Supercritical Carbon Dioxide at 300 bar and Temperatures up to 160°C, Text. Res. J. 72 (2002) 1023–1032. https://doi.org/10.1177/004051750207201115.

[40] L. V. Daza Serna, C.E. Orrego Alzate, C.A. Cardona Alzate, Supercritical fluids as a green technology for the pretreatment of lignocellulosic biomass, Bioresour. Technol. 199 (2016) 113–120. https://doi.org/10.1016/J.BIORTECH.2015.09.078.

[41] C. François, V. Placet, J. Beaugrand, S. Pourchet, G. Boni, D. Champion, S. Fontaine, L. Plasseraud, Can supercritical carbon dioxide be suitable for the green pretreatment of plant fibres dedicated to composite applications?, J. Mater. Sci. 55 (2020) 4671–4684. https://doi.org/10.1007/s10853-019-04293-y.

[42] M.C. Seghini, F. Touchard, L. Chocinski-Arnault, V. Placet, C. François, L. Plasseraud, M.P. Bracciale, J. Tirillò, F. Sarasini, Environmentally friendly surface modification treatment of flax fibers by supercritical carbon dioxide, Molecules. 25 (2020) 1–16. https://doi.org/10.3390/molecules25030438.

[43] J. Zhang, H. Zheng, L. Zheng, Effect of treatment temperature on structures and properties of flax rove in supercritical carbon dioxide, Text. Res. J. 88 (2018) 155–166. https://doi.org/10.1177/0040517516676068.

[44] L.J. Gerhardt, C.W. Manke, E. Gulari, Rheology of polydimethylsiloxane swollen with supercritical carbon dioxide, J. Polym. Sci. Part B Polym. Phys. 35 (1997) 523–534. https://doi.org/10.1002/(SICI)1099-0488(199702)35:3<523::AID-POLB11>3.0.CO;2-J.

[45] B. Gebert, W. Saus, D. Knittel, H. Buschmann, E. Schollmeyer, Dyeing Natural Fibers with Disperse Dyes in Supercritical Carbon Dioxide, Text. Res. J. 64 (1994) 371–374. https://doi.org/10.1177/004051759406400701.

[46] J. Jaxel, F.W. Liebner, C. Hansmann, Solvent-Free Dyeing of Solid Wood in Water-Saturated Supercritical Carbon Dioxide, ACS Sustain. Chem. Eng. 8 (2020) 5446–5451. https://doi.org/10.1021/acssuschemeng.0c01273.

[47] P.L. Beltrame, A. Castelli, E. Selli, A. Mossa, G. Testa, A.M. Bonfatti, A. Seves, Castelli, E. Selli, A. Mossa, G. Testa, A.M. Bonfatti, A. Seves, Dyeing of Cotton in Supercritical Carbon Dioxide, Dye. Pigment. 39 (1998) 335–340. https://doi.org/10.1016/S0143-

7208(98)00016-3.

[48] A. Schmidt, E. Bach, E. Schoomeyer, The dyeing of natural fibres with reactive disperse dyes in supercritical carbon dioxide, Dye. Pigment. 56 (2003) 27–35. https://doi.org/10.1016/S0143-7208(02)00108-0.

[49] M. Banchero, Supercritical fluid dyeing of synthetic and natural textiles - a review, Color. Technol. 129 (2013) 2–17. https://doi.org/10.1111/cote.12005.

[50] D. fa Yang, X. jun Kong, D. Gao, H. sheng Cui, T. ting Huang, J. xin Lin, Dyeing of cotton fabric with reactive disperse dye contain acyl fluoride group in supercritical carbon dioxide, Dye. Pigment. 139 (2017) 566–574. https://doi.org/10.1016/J.DYEPIG.2016.12.050.

[51] S. Maeda, S. Hongyou, K. Kunitou, K. Mishima, Dyeing Cellulose Fibers with Reactive Disperse Dyes in Supercritical Carbon Dioxide, Text. Res. J. 72 (2002) 240–244. https://doi.org/10.1177/004051750207200310.

[52] J.J. Long, G.D. Xiao, H.M. Xu, L. Wang, C.L. Cui, J. Liu, M.Y. Yang, K. Wang, C. Chen, Y.M. Ren, T. Luan, Z.F. Ding, Dyeing of cotton fabric with a reactive disperse dye in supercritical carbon dioxide, J. Supercrit. Fluids. 69 (2012) 13–20. https://doi.org/10.1016/j.supflu.2012.05.002.

[53] M.V.F. Cid, G.F. Woerlee, G.J. Witkamp, Textile dyeing in supercritical carbon dioxide, … Supercrit. Fluids. (2003). http://www.isasf.net/fileadmin/files/Docs/Versailles/Papers/PMt2.pdf.

[54] M. van der Kraan, M. V. Fernandez Cid, G.F. Woerlee, W.J.T. Veugelers, G.J. Witkamp, Dyeing of natural and synthetic textiles in supercritical carbon dioxide with disperse reactive dyes, J. Supercrit. Fluids. 40 (2007) 470–476. https://doi.org/10.1016/j.supflu.2006.07.019.

[55] L. Li, E. Kir, Interaction of Supercritical Fluids with Lignocellulosic Materials, 1988. https://pubs.acs.org/sharingguidelines (accessed November 4, 2019).

[56] D.L. Tomasko, X. Han, D. Liu, W. Gao, Supercritical fluid applications in polymer nanocomposites, Curr. Opin. Solid State Mater. Sci. 7 (2003) 407–412. https://doi.org/10.1016/j.cossms.2003.10.005.

[57] Y. Haldorai, J.J. Shim, K.T. Lim, Synthesis of polymer-inorganic filler nanocomposites in supercritical CO 2, J. Supercrit. Fluids. 71 (2012) 45–63. https://doi.org/10.1016/j.supflu.2012.07.007.

[58] C.D. Pascual, P. Subra-Paternault, Supercritical Fluid Nanotechnology, 2015. https://doi.org/10.1201/b19242.

[59] A. Langhorst, S. Peczonczyk, H. Sun, Biocarbon : A lightweight , functional filler for under-the- hood automotive composites, (2022) 1–13. https://doi.org/10.1002/pc.26517.

[60] A. Langhorst, S. Peczonczyk, H. Sun, A. Kiziltas, D. Mielewski, Biocarbon Hybrid Composites For High-Temperature Automotive Applications, in: ANTEC, Society of Plastics Engineers, 2021.

[61] A. Codou, M. Misra, A.K. Mohanty, Sustainable biocarbon reinforced nylon 6/polypropylene compatibilized blends: Effect of particle size and morphology on performance of the biocomposites, Compos. Part A Appl. Sci. Manuf. 112 (2018) 1–10. https://doi.org/10.1016/j.compositesa.2018.05.018.

[62] A. Pantano, Mechanical Properties of CNT/Polymer, Elsevier, 2017. https://doi.org/10.1016/B978-0-323-48221-9.00009-1.

[63] E.C. Lee, D.F. Mielewski, Exfoliation and Dispersion Enhancement in Polypropylene Nanocomposites by In Situ Ultrasonication, 2001. http://www.rlis.ford.com/techreports (accessed October 23, 2019).

[64] D.L. Tomasko, H. Li, D. Liu, X. Han, M.J. Wingert, L.J. Lee, K.W. Koelling, A Review of CO2 Applications in the Processing of Polymers, Ind. Eng. Chem. Res. 42 (2003) 6431–6456. https://doi.org/10.1021/ie030199z.

[65] Z.-T. Liu, L. Zhang, Z. Liu, Z. Gao, W. Dong, H. Xiong, Y. Peng, S. Tang, Supercritical CO 2 Dyeing of Ramie Fiber with Disperse Dye, (2006). https://doi.org/10.1021/ie061093h.

[66] Q. Yu, P. Wu, P. Xu, L. Li, T. Liu, L. Zhao, Synthesis of cellulose/titanium dioxide hybrids in supercritical carbon dioxide, Green Chem. 10 (2008) 1061–1067. https://doi.org/10.1039/b806094k.

[67] J.L. Gerlock, T.J. Prater, S.L. Kaberline, J.L. Dupuie, E.J. Blais, D.E. Rardon, 18O- time-of-flight secondary ion mass spectrometry technique to map the relative photooxidation resistance of automotive paint systems, Polym. Degrad. Stab. 65 (1999) 37–45. https://doi.org/10.1016/S0141-3910(98)00214-6.

[68] American Society for Testing and Materials, Standard Test Method for Tensile Strength and Young's Modulus of Fibers, Astm C1557-14. (2014) 1–10. https://doi.org/10.1520/C1557-14.2.

[69] A. Singhal, M. Banu, A. Taub, Improving the process of stem breaking for damage reduction in extracted natural fibers, J. Manuf. Process. 86 (2023) 143–151. https://doi.org/10.1016/J.JMAPRO.2022.12.037.

[70] A. Langhorst, M. Ravandi, D. Mielewski, M. Banu, Technical agave fiber tensile performance: The effects of fiber heat-treatment, Ind. Crops Prod. 171 (2021) 113832. https://doi.org/10.1016/j.indcrop.2021.113832.

[71] K. Anurakparadorn, A. Taub, E. Michielssen, Dispersion of Cobalt Ferrite Functionalized Graphene Nanoplatelets in PLA for EMI Shielding Applications, Proc. Am. Soc. Compos. Tech. Conf. Compos. Mater. 0 (2021) 2163–2192. https://doi.org/10.12783/ASC36/35905.

[72] C.M. Lara-Mondragón, C.A. MacAlister, Arabinogalactan glycoprotein dynamics during the progamic phase in the tomato pistil, Plant Reprod. 34 (2021) 131–148. https://doi.org/10.1007/s00497-021-00408-1.

[73] T. Okano, A. Koyanagi, Structural Variation of Native Cellulose Related to Its Source, 25 (1986) 851–861.

[74] L. Segal, J.J. Creely, A.E. Martin, C.M. Conrad, An Empirical Method for Estimating the Degree of Crystallinity of Native Cellulose Using the X-Ray Diffractometer, Text. Res. J. 29 (1959) 786–794. https://doi.org/10.1177/004051755902901003.

[75] S. Nam, A.D. French, B.D. Condon, M. Concha, Segal crystallinity index revisited by the simulation of X-ray diffraction patterns of cotton cellulose Iβ and cellulose II, Carbohydr. Polym. 135 (2016) 1–9. https://doi.org/10.1016/j.carbpol.2015.08.035.

[76] P. Zugenmaier, Order in cellulosics : Historical review of crystal structure research on cellulose, Carbohydr. Polym. 254 (2021) 117417. https://doi.org/10.1016/j.carbpol.2020.117417.

[77] J.E.G. van Dam, T.A. Gorshkova, Fiber Formation., Encycl. Appl. Plant Sci. (2003) 87–96. https://doi.org/10.1016/B0-12-227050-9/00046-6.

[78] A. Langhorst, E. Harrison, A. Singhal, M. Banu, A. Taub, Reinforcement of Natural Fibers via Supercritical Fluid Infiltration of Nanoparticles, in: Am. Soc. Compos. Tech. Conf. Compos. Mater., 2022.

[79] M. Aslan, G. Chinga-Carrasco, B.F. Sørensen, B. Madsen, Strength variability of single flax fibres, J. Mater. Sci. 46 (2011) 6344–6354. https://doi.org/10.1007/S10853-011-5581-X/TABLES/5.

[80] K. Charlet, S. Eve, J.P. Jernot, M. Gomina, J. Breard, Tensile deformation of a flax fiber, Procedia Eng. 1 (2009) 233–236. https://doi.org/10.1016/j.proeng.2009.06.055.

[81] G. Vaca-Medina, B. Jallabert, D. Viet, J. Peydecastaing, A. Rouilly, Effect of temperature on high pressure cellulose compression, Cellulose. 20 (2013) 2311–2319. https://doi.org/10.1007/S10570-013-9999-Y/FIGURES/4.

[82] B. Jallabert, G. Vaca-Medina, S. Cazalbou, A. Rouilly, The pressure-volume-temperature relationship of cellulose, Cellulose. 20 (2013) 2279–2289. https://doi.org/10.1007/S10570-013-9986-3/FIGURES/10.

[83] A. Belaadi, A. Bezazi, M. Bourchak, F. Scarpa, C. Zhu, Thermochemical and statistical mechanical properties of natural sisal fibres, Compos. Part B Eng. 67 (2014) 481–489. https://doi.org/10.1016/j.compositesb.2014.07.029.

[84] E. Maleki, S. Bagherifard, O. Unal, M. Bandini, G.H. Farrahi, M. Guagliano, Introducing gradient severe shot peening as a novel mechanical surface treatment, Sci. Reports 2021 111. 11 (2021) 1–13. https://doi.org/10.1038/s41598-021-01152-2.

[85] K. Zhan, Y. Wu, J. Li, B. Zhao, Y. Yan, L. Xie, L. Wang, V. Ji, Investigation on surface layer characteristics of shot peened graphene reinforced Al composite by X-ray diffraction method, Appl. Surf. Sci. 435 (2018) 1257–1264. https://doi.org/10.1016/J.APSUSC.2017.11.242.

[86] A.N. Al-Khazraji, M.N.M. Shareef, Effect of Shot Peening on the Endurance Limit of Fiber Glass Composite Material, Int. J. Sci. Eng. Res. 5 (2014). http://www.ijser.org (accessed December 7, 2022).

[87] H. Hadidi, B. Mailand, T. Sundermann, E. Johnson, R. Karunakaran, M. Negahban, L. Delbreilh, M. Sealy, Dynamic mechanical analysis of abs from hybrid additive manufacturing by fused filament fabrication and shot peening, in: ASME 2020 15th Int. Manuf. Sci. Eng. Conf. MSEC 2020, 2020: pp. 1–9. https://doi.org/10.1115/MSEC2020-8253.

[88] A. Arbelaiz, B. Fernández, J.A. Ramos, I. Mondragon, Thermal and crystallization studies of short flax fibre reinforced polypropylene matrix composites: Effect of treatments, Thermochim. Acta. 440 (2006) 111–121. https://doi.org/10.1016/j.tca.2005.10.016.

[89] C. Baley, F. Busnel, Y. Grohens, O. Sire, Influence of chemical treatments on surface properties and adhesion of flax fibre–polyester resin, Compos. Part A Appl. Sci. Manuf. 37 (2006) 1626–1637. https://doi.org/10.1016/j.compositesa.2005.10.014.

[90] A. Le Duigou, P. Davies, C. Baley, Interfacial bonding of Flax fibre/Poly(l-lactide) bio-composites, Compos. Sci. Technol. 70 (2010) 231–239. https://doi.org/10.1016/j.compscitech.2009.10.009.

[91] A. Bourmaud, J. Beaugrand, D.U. Shah, V. Placet, C. Baley, Towards the design of high-performance plant fibre composites, Prog. Mater. Sci. 97 (2018) 347–408. https://doi.org/10.1016/j.pmatsci.2018.05.005.

[92] M. Hughes, J. Carpenter, C. Hill, Deformation and fracture behaviour of flax fibre reinforced thermosetting polymer matrix composites, J. Mater. Sci. 42 (2007) 2499–2511. https://doi.org/10.1007/S10853-006-1027-2/FIGURES/12.

[93] J. Summerscales, A.S. Virk, W. Hall, Enhanced rules-of-mixture for natural fibre reinforced polymer matrix (NFRP) composites (comment on Lau et al. in volume 136), Compos. Part B Eng. 160 (2019) 167–169. https://doi.org/10.1016/J.COMPOSITESB.2018.10.021.

[94] A.S. Virk, W. Hall, J. Summerscales, Modulus and strength prediction for natural fibre composites, Mater. Sci. Technol. (United Kingdom). 28 (2012) 864–871. https://doi.org/10.1179/1743284712Y.0000000022.

[95] H.L. Cox, The elasticity and strength of paper and other fibrous materials, Br. J. Appl. Phys. 3 (1952) 72–79. https://doi.org/10.1088/0508-3443/3/3/302.

[96] S.R. Bakshi, A. Agarwal, An analysis of the factors affecting strengthening in carbon

nanotube reinforced aluminum composites, Carbon N. Y. 49 (2011) 533–544. https://doi.org/10.1016/j.carbon.2010.09.054.

[97] D.U. Shah, R.K. Nag, M.J. Clifford, Why do we observe significant differences between measured and 'back-calculated' properties of natural fibres?, Cellul. 2016 233. 23 (2016) 1481–1490. https://doi.org/10.1007/S10570-016-0926-X.

[98] M.W. Tham, M.N. Fazita, H.P.S. Abdul Khalil, N.Z. Mahmud Zuhudi, M. Jaafar, S. Rizal, M.M. Haafiz, Tensile properties prediction of natural fibre composites using rule of mixtures: A review, J. Reinf. Plast. Compos. 38 (2019) 211–248. https://doi.org/10.1177/0731684418813650.

[99] B. Madsen, A. Thygesen, H. Lilholt, Plant fibre composites – porosity and stiffness, Compos. Sci. Technol. 69 (2009) 1057–1069. https://doi.org/10.1016/J.COMPSCITECH.2009.01.016.

[100] B. Lamy, C. Baley, Stiffness prediction of flax fibers-epoxy composite materials, J. Mater. Sci. Lett. 19 (2000) 979–980. https://doi.org/10.1023/A:1006776423764.

[101] A. Lefeuvre, A. Bourmaud, C. Morvan, C. Baley, Elementary flax fibre tensile properties: Correlation between stress–strain behaviour and fibre composition, Ind. Crops Prod. 52 (2014) 762–769. https://doi.org/10.1016/j.indcrop.2013.11.043.

[102] Kelsey Steinke, Nanomaterial-Based Surface Modifications for Improved Ballistic and Structural Performance of Ballistic Materials, 2015.

[103] J. Nasser, J. Lin, K. Steinke, H.A. Sodano, Enhanced interfacial strength of aramid fiber reinforced composites through adsorbed aramid nanofiber coatings, Compos. Sci. Technol. 174 (2019) 125–133. https://doi.org/10.1016/J.COMPSCITECH.2019.02.025.

[104] G. Li, C. Zhang, Y. Wang, P. Li, Y. Yu, X. Jia, H. Liu, X. Yang, Z. Xue, S. Ryu, Interface correlation and toughness matching of phosphoric acid functionalized Kevlar fiber and epoxy matrix for filament winding composites, Compos. Sci. Technol. 68 (2008) 3208–3214. https://doi.org/10.1016/j.compscitech.2008.08.006.

[105] H. Dong, J. Wu, G. Wang, Z. Chen, G. Zhang, The ultrasound-based interfacial treatment of aramid fiber/epoxy composites, J. Appl. Polym. Sci. 113 (2009) 1816–1821. https://doi.org/10.1002/APP.30055.